CHAPTER ONE

INTRODUCTION

1.1 Introduction to Oleochemicals

“Oleochemicals” refer to chemicals derived from natural oils and fats of both plant and animal origins. Basically, oleochemicals refer to the fatty acids and glycerol derived from the splitting of the triglyceride structures of oils and fats. However, they also include those derivatives derived from the subsequent modification of the carboxylic acid group of the fatty acids by chemical or biological means, and other compounds obtained from further reactions of these derivatives. Oleochemicals are often categorised into basic oleochemicals such as fatty acids, fatty methyl esters, fatty alcohols, fatty amines and glycerol, and their further downstream derivatives obtained from further chemical modifications of these basic oleochemicals.

The uses of oleochemicals are mostly for food purposes. In fact, until the1980s, almost 95% of natural oils are used in foods and only a small percentage is used in non-food applications such as soap manufacturing and drying oils. It was only after the 1980s that oleochemicals found wide uses in technical applications which previously are the domains of “synthetic chemicals” derived from petroleum or better known as petrochemicals. At this moment, oleochemicals are used in the manufacture of products such as soaps and detergents, cosmetics and personal care products, lubricants and greases, drying oil, surface coatings and polymers, and biofuels (Table 1.1). In theory, oleochemicals can replace petrochemicals in all their applications. These are because oleochemicals are derived from renewable resources, as compared to petrochemicals which are obtained from exhaustible or non-renewable petroleum, and products derived from oleochemicals are more readily biodegradable and hence do not pose a threat to the environment while products derived from petroleum sources use more energy and cause higher emission of pollutants such as NO_x, SO_2, CO and hydrocarbons.

Basic oleochemicals are materials produced principally from the hydrolysis or methylation of oils and fats. Thus fatty acids, fatty methyl esters, fatty alcohols, fatty amines and glycerine are generally refer to as basic oleochemicals. These materials are produced from oil and fat feedstocks.

Table 1.1: Applications of Oleochemicals [Malaysian Palm Oil Board(2006)].

Industry/Product	Uses
Leather	Softening, dressing, polishing and treating agents
Metal Work & Foundry	Cutting oils, coolants, buffing and polishing compounds
Mining	Surface-active agents for froth flotation of ore and oil-well drilling
Rubber	Vulcanising agents, softeners and mould-release agents
Electronics	Insulation and special-purpose plastic components
Lubricants and Hydraulic Fluids	General and specialty industrial lubricants and biodegradable base oils, hydraulic fluids
Paints and Coatings	Alkyd and other resins, drying oils, varnishes and other protective coatings
Printing and Paper Re-cycling	Printing inks, paper coatings, photographic printing, de-inking surfactants
Plastics	Stabilizers, plasticisers, mould-release agents, lubricants, anti-static agents, antifogging aids, polymerisation emulsifiers

Biofuels	Methyl esters and alcohols
Waxes	Ingredients in waxes and polishes
Soaps & Detergents	Industrial and domestic products, specialty surfactants
Health & Personal Care	Culture media, tabletting aids, soaps, shampoos, creams, lotions

1.2 An Overview of the Malaysian Palm Oil Industry

1.2.1 Palm Oil Industry

Technological development has transformed the Malaysian palm oil industry into a strategic and well planned industry that responds to global challenges. In particular, genetic knowledge since as early as 1912 first led the phenomenal growth of the industry through the planting of tenera instead of dura palms. This was complemented by the government allocating land to the poor and landless to plant more oil palm, in great part causing the area to increase from 641 791 hectares in 1975 to 1.02 million hectares in 1980 and 2.03 million hectares in 1990. By 2006, there were 4.16 million hectares of oil palm, constituting nearly two-thirds of the national agricultural area (Table 1.2). Malaysia continues to be the world’s largest palm oil producer with a production of 15.90 million tonnes in 2006.

The success of the crop is largely market driven with good longterm price prospects for palm oil thus making oil palm more attractive than most other crops. Palm oil contributes more than one-third of the national agricultural GDP, generating RM 31.81 billion in export earnings in 2006, making it one of the pillars of Malaysia’s economy. At present, the industry employs more than 1.5 million people in the core and related sectors.

Table 1. 2: Oil Palm Planted Area: 1975-2006 (hectares)

Year	P.Malaysia	Sabah	Sarawak	Total
1975	568,561	59,139	14,091	641,791
1980	906,590	93,967	22,749	1,023,306
1985	1,292,399	161,500	28,500	1,482,399
1990	1,698,498	276,171	54,795	2,029,464
1995	1,903,171	518,133	118,783	2,540,087
2000	2,045,500	1,000,777	330,387	3,376,664
2001	2,096,856	1,027,328	374,828	3,499,012
2002	2,187,010	1,068,973	414,260	3,670,243
2003	2,202,166	1,135,100	464,774	3,802,040
2004	2,201,606	1,165,412	508,309	3,875,327
2005	2,298,608	1,209,368	543,398	4,051,374
2006	2,334,247	1,239,497	591,471	4,165,215

1.2.2 Oleochemical Industry

Malaysia is one of the world's leading oleochemical producers and exporters, capitalising on its competitiveness, innovation and productivity in palm oil-based products. Arising from the phenomenal growth of the palm oil industry in Malaysia, the Malaysian oleochemical industry started to take place in 1980 when a local company produced 10,000 tonnes of fatty acids and glycerol. There were a number of factors that contributed to this rapid expansion of the oleochemical industry in Malaysia. First is the involvement of the Multi-National Companies “or MNCs, which take advantage of the low production cost and abundant supply of raw materials, in joint ventures with local companies". On top of this are the incentives provided by the Malaysian government which identified the oleochemical industry as the potential growth sector of the palm oil industry. In the first Industrial Master Plan (IMP), targets were set to increase production of basic oleochemicals from 126,000 tonnes in 1984 to 886,000 tonnes in 1994 and 1,360,000 tonnes in 1999.

Ever since then, the Malaysian oleochemical industry has grown rapidly upon incentives given by the government, and the targets have been exceeded many times. At the present moment, there are 21 companies in operation, 12 are joint ventures, 4 are 100% foreign owned and 5 Malaysian owned. 14 of these companies are producing basic oleochemicals and glycerin, and 7 companies are producing derivatives such as metallic soaps, cosmetic esters, and soap noodles (Table 1.3). Total investment is estimated at USD 1 billion.

Table 1.3: Oleochemicals Companies and Their Products in Malaysia [Malaysian Oleochemical Manufacturers' Group (MOMG)]

Company	Products
Acidchem International, Stabilchem, Derichem	Fatty Acids, Glycerine, Metal Stearates, Soap Noodles
Fatty Chemicals	Fatty Alcohols, Methyl Esters, Glycerine, Ethylene Bis-Stearamide (EBS), Soap Noodles
Danisco Cultor	Cosmetic and Food Esters
Cognis Oleochemicals	Fatty Alcohols, Glycerine, Methyl Esters, Fatty Acids
Unichema Malaysia	Fatty Acids, Glycerine, Soap Noodles, Cosmetic Esters
FPG Oleochemicals	Methyl Esters and Fatty Alcohols
Southern Acids	Fatty Acids, Glycerine, Soap Noodles

Palm Oleo, KSP, Palmamide	Fatty Acids, Glycerine, Soap Noodles, Ethylene Bis-Stearamide (EBS), Alkanolamides
Esterol	Mono-Glycerides
Natural Oleochemical, Dubois Natural	Fatty Acids, Glycerine, Cosmetic Esters
Pan Century Oleochemicals	Fatty Acids, Glycerine, Soap Noodles
Akzo Nobel, Lam Soon Edible Oil	Fatty Acids, Glycerine, Soap Noodles
Rikken Vitamin	Mono-Glycerides
Twenty First Century	Ceased operation in 1993; planning to restart soon.

1.3 Fatty Amines

Vegetable oils can be used as starting materials for a great number of intermediates, such as fatty alcohols, alpha olefins and fatty amines. Fatty amines are the most important nitrogen derivatives of fatty acids. They are produced by the reaction of fatty acids with ammonia and hydrogen (eq. 1-3). Further descriptions are described in page 12.

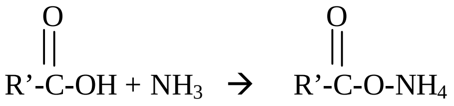

$$R'\text{-}\overset{\overset{O}{\|}}{C}\text{-}OH + NH_3 \rightarrow R'\text{-}\overset{\overset{O}{\|}}{C}\text{-}O\text{-}NH_4 \qquad (1)$$

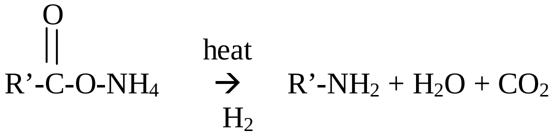

$$R'\text{-}\overset{\overset{O}{\|}}{C}\text{-}O\text{-}NH_4 \xrightarrow[H_2]{heat} R'\text{-}NH_2 + H_2O + CO_2 \qquad (2)$$

The most important source of fatty amines, is fatty nitriles which are formed from the fatty alcohols and ammonia over dehydrating catalysts such as Al_2O_3, ZnO or salts of Mn or Co in liquid phase or vapor phase at 280-360^{o}C. Subsequently, the reaction of fatty nitriles in presence of a Cu-chromite catalyst at 80-140°C and 10-40 bar produces fatty amines (eq. 3).

$$R'\text{-}CN + 2H_2 \xrightarrow{cat} R'CH_2\text{-}NH_2 \qquad (3)$$

The most direct route to fatty amines, however, is by conversion of fatty alcohols in the presence of ammonia (reductive alkylation of ammonia) or in the presence of substituted amines (eq. 4).

$$R\text{-}OH + NH_3 \xrightarrow{cat} R\text{-}NH_2 + H_2O \qquad (4)$$

This process is usually carried out in the range of 90-190°C at 1-7 bar using a Nickel catalyst [Li Qiuxio et. al, 2002]. The main product from this reaction is mostly primary amines. Secondary and tertiary amines can be produced using fatty alcohol by means of H_2O removal. Although nitrile hydrogenation is considered to be a much cheaper process for the high carbon numbers fatty amine than from the alcohol, direct alcohol hydrogenation is better suited for production of low carbon numbers fatty amines.

1.4 Market Analysis of Fatty Amines

The total market for fatty amines in 2000 was estimated at 2 billion dollars (Chemical Week, January 2001). Market leader in the production of fatty amines is Akzo Nobel Surface Chemicals, which had revenues of $585 million in 2000 of which an estimated 20% is generated by the sales of amines (both short chain and fatty amines). Another major player in the fatty amines market is BASF. Assuming that BASF's market share is 10%, the global market for fatty amines is roughly estimated at $1 billion. Precise figures are impossible to obtain due to the use of large amounts of amine used as chemical intermediates for subsequent production in other secondary compounds.

The world average growth rate for fatty amine is projected to be about 2% per annum. World fatty amine production in 1995 and 2005 totaled 525,000t and 620,000t respectively. Europe fatty amine production in 2005 totaled 200,000t, worth US$605m and representing 32.2 % of the total oleochemical market. While in Asia fatty amine production in 2005 totaled 200,000t. Fatty amine forecast in Asia to achieve compound growth 0.7% to 2010 (Figure 1.1).

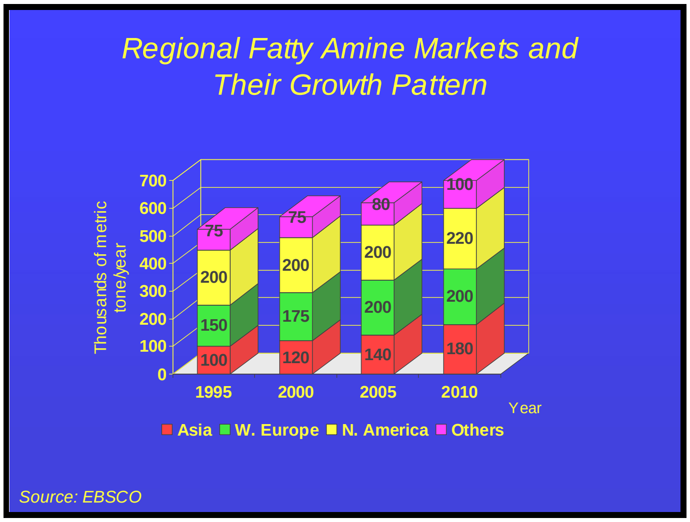
Regional Fatty Amine Markets and Their Growth Pattern

Source: EBSCO

Figure 1.1: Regional fatty amine markets and their growth pattern

1.5 Applications of Fatty Amines

Fatty amines are mainly used as fabric softeners, of which the quaternary ammonium compounds are most prominent, e.g. N,N-dimethyldialkyl ammonium chloride. For example, distearyldimethyl ammonium chloride can be produced by the reaction of distearylamine and methylchloride with continuous addition of alkali. Other applications of quaternary fatty ammonium compounds are as corrosion inhibition agents, asphalt emulsifiers, dispersants, bactericides, sanitizers and disinfectants.

Primary fatty amines are used as anti-caking agents and flotation agents. Tertiary amines are used in the manufacture of amine oxides by the oxidation with hydrogen peroxide. The amine oxides are used in cosmetic preparations for their good foaming properties and mildness to the skin. Another raw material used in the cosmetic industry is the betaines produced by the reaction of a tertiary fatty amine with sodium chloroacetate. The betaines exhibit good foam stability over a wide range of pH, are insensitive to water hardness, and are mild to the skin. The asymmetrical tertiary amines are used exclusively as starting materials for the manufacture of quaternary ammonium compounds, cationic and amphoteric surfactant, and amine oxides. Quatenary ammonium compounds used as bactericides and algasides are produced by the reaction of tertiary amines with benzyl chloride, methyl chloride, or dimethyl sulfate. Of these, the benzyl ammonium chloride salt is the most widely used.

The cationic compounds of fatty amines and fatty amine derivatives differ from anionic and nonionic surfactants in that they have a marked degree of substantivity for nearly all solid surfaces. Their substantivity is a characteristic property which allows them to be absorbed onto solids and form a firm cationic film on them so that properties can be varied to fit in with any desired applications. Thus materials such as wool, hair, leather, cotton, synthethic fibres, plastics, dye pigments, rocks, metals etc. can be treated with fatty-amine-based cationic formulations to acquire useful properties for quite specific applications. Substantivity imparts versatility in product application and this reflects in fields as described before which include:

- Anticorrosion agents for oil, aqueous media and lubricants,
- Fabric softners, antistatic agents,
- Bonding and wetting agents for varnishes, paints, adhesives, dispersions and bitumen/asphalt,
- Textile, leather, rubber, dyeing and washing auxiliaries,
- Hair conditioners and disinfectants,
- Flotation agents and anticaking products etc.

1.6 Issues in Fatty Amines Production

Process for producing amines from aldehyde, ketones or alcohols, comprising of reacting them with an aminating agent in the presence of a catalyst, are well known. However, many of the known process are expensive, inefficient and inoperative for the production of high molecular weight and/or branched amines and /or require harsh reaction conditions.

A large number of catalysts suitable for liquid phase amination of fatty alcohols with ammonia have been disclosed. By liquid phase amination process wherein the alcohol is in the liquid phase, while the ammonia or the primary or secondary amines are in the liquid or gaseous phase. However, it is difficult to selectively produce the primary amine. Normally secondary and tertiary amines are produced in large quantities. A wide variety of metal catalysts are used for the amination of alcohol, e.g. nickel, copper, chromium and iron, or the oxides thereof, optionally in combination with alkali and alkaline earth metals as co-catalysts. A large number of the said catalysts are highly reactive which, however, will mean poor selectivities for primary amines. Another issue associated is with the separation of the alcohol and the primary amine, because the boiling points of the said products are close together. Another potential problem relates to the instability of the intermediate imine, which is a Schiff base and therefore undergoes aldol-dimerization and is susceptible to conversion to polymeric products even under relatively mild reaction conditions in the presence of certain catalysts.

1.7 Objectives and Scope of work

The scope of the research work involves the following objectives:

1. To synthesis supported bimetallic catalysts CuZn and CuNi via slurry method.
2. To characterize the catalysts by X-ray Diffraction (XRD), Scanning Electron Microscope (SEM) and Energy Dispersive X-ray (EDX), Ultraviolet Visible (UV-Vis) Spectroscopy, Fourier Transform Infrared (FTIR) and X-ray Fluorescence (XRF), Thermal Gravimetric Analysis-Mass Spectrometer (TGA-MS), Differential Scanning Calorimetric (DSC) and Temperature Programme Reduction (TPR).
3. To screen the catalyts for hydrogenation reaction of fatty alcohols to fatty amines.

CHAPTER TWO

LITERATURE REVIEW

2.1 Introduction

Fatty amines can be produced by converting fatty acids to fatty amides and subsequently to fatty nitriles. GB patent 981,123 (1965) claims a process in which the conversion is carried out by liquid phase reaction with ammonia in three steps: at 170-180°C and 3.5-7 bar to form the amide, at 280-300°C and 2-3 bar and subsequently at 300-320°C and 1 bar to convert the amide to the nitrile. The conversion takes place over a dehydration catalyst. Hoechst patent US 4,801,730 (1989) describes the formation of fatty nitriles from the glyceride by reaction with ammonia gas over Zn, Pb, Cd, Co, Fe(II) and Sn(IV) alkylsulfonates. This batch process is operated in two steps at an ammonia rate of 15-100 l//kg fat/h, starting at 230-260°C until all glyceride has been converted and then raising the temperature to 260-300°C.

The most important source of fatty amines, is fatty nitriles which are formed from the fatty alcohols and ammonia over dehydrating catalysts such as Al_2O_3, ZnO or salts of Mn or Co in liquid phase or vapor phase at 280-360°C. Subsequently, the reaction of fatty nitriles in presence of a Cu-chromite catalyst at 80-140°C and 10-40 bar produces fatty amines. The most direct route to fatty amines, however, is by conversion of fatty alcohols in the presence of ammonia (reductive alkylation of ammonia) or in the presence of substituted amines. This process is usually carried out in the range of 90-190°C at 1-7 bar using a Nickel catalyst (Figure 2.1). The main product from this reaction is mostly primary amines. Secondary and tertiary amines can be produced using fatty alcohol- by means of H_2O removal. Although nitrile hydrogenation is considered to be a much cheaper process for the high carbon numbers fatty amine than from the alcohol, direct alcohol hydrogenation is better suited for production of low carbon numbers fatty amines. A summary of the catalysts and process conditions listed in Patents and Journals are given in Table 2.1 & Table 2.2.

Table 2.1: Summary of catalyst and process listed in patents

Catalyst	Feed	Process details	Reference
Ni/ Cobalt/support	C_{12}-C_{18} alcohol	Batch, NH_3, 100-350^{0}C, 40 bar	US 5808158 (1998)
Ni-Mg/Support	C_6-C_{24} (linear)	Batch, NH_3, 80-200^{o}C, 60 bar	Eur. Pat. 547505 (1993), Hoechst.
Ni or Co	C_8-C_{22} (linear, unsat)	Batch, 2 steps, NH_3,80-160^{o}C, 50 bar	Eur. Pat. 547505 (1992), Hoechst.
Raney Co promoted with Ni and Cr	Polynitrile	Continuous, NH_3, 60-125^{o}C, 300 bar	US 5105015 (1992)
Ni/SiO_2	C_6-C_{24} (linear)	Batch, NH_3 and NaOH, 150^{o}C, 50 bar	DE 156177 (1981)
Raney Ni	>C_6	Batch, NH_3, 125-140^{o}C, 10 bar	GD 1321981 (1973)
Ni-Cu-Cr-Mo	C_8-C_{22} (linear)	Continuous, 2 steps, NH_3, 130-180^{o}C, 300 bar	US 5130491 (1992)
Co-Zr/support	C_8-C_{22} (linear)	Continuous, 2 steps, 150^{o}C, 35bar	Eur. Pat. 451979 (1991)
Ni/support	C_8-C_{22} (linear, unsat)	Batch, presence of $AcNH_2$ to inhibit the reaction of C=C, 160-200^{o}C, 200 bar	Eur. Pat. 232097 (1986)
Cu-Cr-K/SiO_2	C_8-C_{22} (linear)	Continuous, 80-250^{o}C, 200 bar	GB 1180972 (1970)

Table 2.2: Summary of catalyst and process listed in Journals

Catalyst	Feed	Process details	Reference
Metal phosphate catalysts (Zr, Ce or B phosphates)	1-Octanol	Batch, NH_3, 250-400°C	Applied Catalysis A:General, 183 (1999), 167-176
Copper, nickel or a Group VIII metal (Ni, Pd, Ru, Rh, Pt)	Cyclohexanol/ cyclohexanone	continuous fixed bed reactor, H_2, 250^{o}C, 1 atm	Applied Catalysis A: General, 197 (2000), 229–238
Cu–Ni catalysts supported on $CaCO_3$	Lauryl Alcohol	Batch, H_2, 170^{o}C	Journal of Surfactants and Detergents, Vol. 5, No.3 (July 2002), 229-233
Activated Ni catalysts	Tallow nitrile	Batch, H_2, 160^{o}C, 50 bar	Catalysis Today, 121 (2007) 106–114

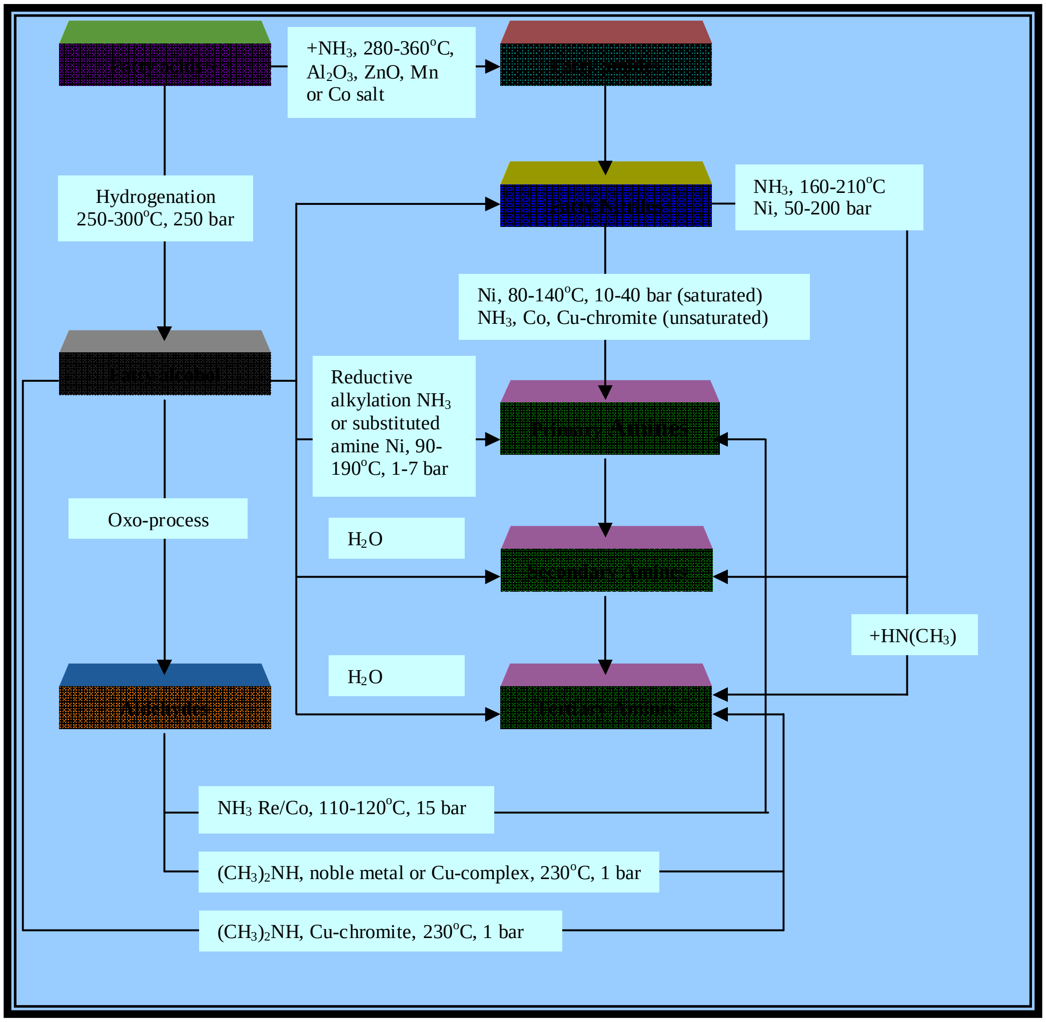

Figure 2.1: Different routes to produce fatty amines

2.2 Hydrogenation Catalysts

2.2.1 Catalyst

Catalysis is a multidisciplinary science that serves a broad range of industries covering specialty, fine, intermediate, commodity and life science chemicals. Catalysts are commonly used for the hydrogenation of alkenes, alkynes, aromatics, aldehydes, ketones, esters, carboxylic acids, nitro groups, nitriles and imines. These materials may be in the form of homogeneous and heterogeneous catalysts where each type has its own special properties that can be adjusted for their optimal use.

Heterogeneous catalysts are commonly used in the form of powders for slurry and fluidized bed reactions or as formed bodies for fixed bed hydrogenations. The addition of promoters and adjustments in particle size and porosity allow these catalysts to be fine tuned for specific reactions. Homogeneous catalysts are also very flexible where the choice of active metal, ligands and reaction conditions can lead to highly selective hydrogenations. The separation problems associated with homogeneous catalysts have led to the development of heterogenised homogeneous catalysts via the fixation of the active complexes on organic or inorganic supports or via application in biphasic systems. While there have been some successes in this area, there still remains a considerable amount of work to be done.

In industrial point of view, catalysis is very important since the production of most industrially important chemicals involves catalysis. Among the earliest commercial processes using the catalyst are the Haber process for synthesis of ammonia and the Fischer-Tropsch synthesis. Catalyst, according to its definition is *"a substance used to boosts up the rate of a chemical reaction but is unchanged at the end of the reaction"* [Bond *et al.*, 1974]. Because catalyst affects only the rate of the reaction, it changes neither the thermodynamics of the reaction nor the equilibrium composition. Catalyst accelerates chemical reaction that is itself not consumed by the overall reaction. The catalyst's fundamental characteristic has to be active, selective to the product and stable to meet the demands of an industrial user. In addition to this, industrial applications require that a catalyst to be regenerable, reproducible, mechanically and thermally stable, original, economical and possesses suitable morphological characteristics.

The art of preparing catalyst is a daunting task. The understanding of catalysis chemistry is as illusive, as in many ways it involves other disciplines: surface science, inorganic, organic, organometallic, materials sciences and even catalytic engineering. A catalyst itself can come in many different forms; from heterogeneous catalysts in the form of porous solids over homogeneous catalysts dissolved in the liquid reaction mixture to biological catalysts in the form of enzymes. The reaction mixture and the catalyst can be either in the same phase or in different phases (homogenous and heterogenous catalysis, respectively) [Bond *et al.*, 1974].

The idea of a good catalyst encompasses high surface area that will allow adsorption of reactant molecules and subsequent reaction between the molecules to form products, again on the surface. The bond between reactants and catalyst or catalyst to products should be flexible enough to allow the product molecules to stick temporarily or otherwise leave the surface of the catalyst. Many practical heterogeneous catalysts consist of one or several catalytically active component(s) deposited on a high-surface-area support. It is known that supported metal and/or oxide catalysts comprise the most important class of heterogeneous catalysts in industrial practice [Dillan V, 2003]. Supports such as alumina and silica have been identified to be able to provide the seat to disperse the active components of the catalyst to hopefully bring about;

(a) larger surface area for contact or complex with reactants

(b) stronger mechanical strength

(c) higher dispersion of reaction heat around the active components

Catalyst development is a process of evolution. Although cases differ, successful process implementation follows a series of logical steps. Each has well defined objective that requires talents of established branches of science and engineering. Since the emergence of industrial catalysis, the development of catalyst has become the most important technologies in our modern world. Indeed, the art of preparation accounts for the strict secrecy surrounding the highly competitive manufacture of solid catalysts, as well as the costly litigation alleging patent infringement. Commercialisation may involve many passes through steps, but every proven catalyst development has, in some fashion, progressed in this manner.

2.2.2 Hydrogenation

Hydrogenation is the chemical reaction between molecular hydrogen and an element or compound, commonly in the presence of a catalyst. The reaction may be one in which hydrogen simply adds to a double or triple bond connecting two atoms in the structure of the molecule or one in which the addition of hydrogen results in dissociation (breaking up) of the molecule (called hydrogenolysis, or destructive hydrogenation). There are several types of hydrogenation reactions. They include: (1) the addition of hydrogen to reactive molecules; (2) the incorporation of hydrogen accompanied by cleavage of the starting molecules (hydrogenolysis); and (3) reactions in which isomerization, cyclization, and so on, result. The industrial importance of the hydrogenation process dates back from 1897, when the French chemist Paul Sebatier discovered that the introduction of a trace of nickel as a catalyst facilitated the addition of hydrogen to molecules of carbon compounds [Hugh S. 1944].

The hydrogenation of fatty alcohol to fatty amine is a heterogenous catalyzed process; with liquid feed and product over a solid catalyst. The catalysts of choice, which allow highly selective conversion of alcohol to amine, are usually based on copper, meaning that the active component is copper. In particular, much of the study of alcohol hydrogenation has been based on the use of “copper-chromite” Catalyst systems. These catalysts were initially developed in 1930 by [Adkins et. al.] for acetaldehyde condensation. While the conventional copper chromite catalyst has been used almost exclusively for the mass production of fatty amine, the activity of this catalyst has been shown to be significantly increased by the addition of other metals such as zinc, nickel, barium, iron, aluminium, manganese and tin [Kurc, L. et al.]. The active components are normally fixed on support material ie. alumina, silica, zirconia, carbon, etc. The catalyst support has a function to enlarge the surface area of active components and also to provide a catalyst stable in a reaction condition against sintering of metal particles. As such, supported metal and metal oxide copper catalysts comprise the most important class of heterogeneous catalysts.

2.3 Copper-based Catalysts

2.3.1 Copper-Chromite Catalysts

Copper-chromite has long been the standard catalyst for the producing fatty amines. However, the search for a non-chromium catalyst has lead to the development of alternative catalysts. Strauss [Strauss, et al, 1979] disclosed a process for carrying out the hydrogenation of fatty alcohol to fatty amine in the liquid phase over a copper-chromium oxide catalyst wherein the liquid alcohol was reacted with a circulating gaseous mixture containing hydrogen and 1-20 percent by volume dimethylamine to obtain up to 93.5 percent yield of dodecyldimethylamine. A catalyst containing 41% by weight of copper, 31% by weight of chromium and 0.3% by weight of barium (corresponding to 69% by weight of copper chromite, 28% by weight of copper oxide and 0.5% by weight of barium oxide) was extremely suitable. Even though the metal oxides may be used in a concentrated form according to known methods, while being applied onto inert carriers, such as aluminum oxide or silica gel, carrier-free fully active catalysts were particularly suitable.

J. Barrault [Barrault et. al, 1992] reported the properties of copper-chromite catalysts can be much modified by the presence of additives such as barium. The selectivity however depended a great deal on the content and the localization of this promoter. The increase in the acidity of the support and the presence of Cr(IV) species favoured the production of the dialkylamine (i.e., didodecylamine) resulting from the condensation of a primary amine with the corresponding imine.

The role of chromium in copper chromite as structural promoter has been studied intensively, in order to develop a catalyst with higher selectivity and activity. However, the discovery that the cupric chromite phase is not essential for hydrogenation catalysts has led to many examples of non-chrome catalyst development. Evans *et al.* [Evans 1983] showed that copper on silica, or even pure Raney copper, can be as effective as copper chromite for the hydrogenation of esters. Thus finely divided metallic copper seems to be the catalytically active component in such systems. According to Kurc and Cerveny [Kurc *et al.* 1988], ZnO as a carrier can replace the traditionally used cupric chromite. Moreover, the needs of alternative non-chrome catalysts are also partially attributed by the environment issues involving the disposal of chrome-containing catalyst.

Copper--chromite catalysts promoted with alkaline or alkaline-earth compounds like rhodium catalysts [Rylander et.al, 1970] could be used for the secondary amine synthesis; but the support could have a definite effect on the final catalytic properties [Dallons et. al 1992].

2.3.2 Copper-Nickel Catalysts

Li Qiuxiao [Li Qiuxiao et al, 2002] reported, there are different types of catalysts for the amination of fatty alcohols, and among them Cu–Ni catalysts show better performance. Lower reducibility of Ni^{2+} has led to higher catalyst selectivity and the higher the ratio of Cu-Ni catalyst, the lower the reducibility of Ni^{2+} in the samples. This is probably due to the greater electronegativity of Cu compared to Ni. When NiO and CuO coexist in a sample, the reduction of CuO occurs prior to that of NiO. The reduction of Ni can be affected by CuO, and the higher the ratio of Cu/Ni the larger the effect, so by varying the Cu/Ni ratio can affect the valence of Ni in the reduced catalyst samples. It has also been found that depression of the reduction of Ni^{2+} in Cu-Ni catalysts is beneficial to lowering the amount of dialkylmethylamines in the amination of fatty alcohols to promote the selectivity of the catalysts.

According to H. Kimura [Kimura et al, 2005] the Cu-Ni -based colloidal catalyst, stabilized by barium stearate (Cu:Ni:Ba mole ratio 5:1:1; particle size 1–5 nm), for the one-step amination of dodecyl alcohol and dimethylamine to *N*,*N*-

dimethyldodecylamine at Cu concentration range of 300–1000 ppm at 200–210 °C, could be recovered by distillation and could be reused several times without a decrease in the activity. The activity of the concentrated activated colloidal catalysts for the amination reaction was not decreased for a month. These observations demonstrated that the reusability and stability of the Cu-Ni based colloidal catalysts were enough for the commercial operation, which opposed to the claim that a colloidal catalyst cannot be recovered and reused. The Cu-Ni-Ba colloidal catalyst is the first example of a metallic colloid applied for the amination reaction.

2.3.3 Copper-Zinc Catalysts

Hoechst patented Cu-Zn-Al catalysts for the production of fatty amines from fatty nitriles or fatty acids and of fatty alcohols from esters [Deckers et.al, 1995]. The co-precipitated catalyst is made by simultaneous addition of a metal nitrate solution and Na_2CO_3 solution at 353 K, filtration, drying at 323-393 K and calcination in air at 523-673 K. The preferred catalyst in its unreduced state contained 52-67 wt% CuO, 29-42 wt% ZnO and 2.7-7.1 wt% Al_2O_3. Optionally, the catalyst contained 0.25-5 wt% of Mn-, Mo-, V-, Zr or alkaline earth oxides. The BET surface area was typically 80-175 m^2g^{-1}, and 75-95% of the pores had a radius smaller than 15 nm. The hydrogenation process conditions were preferably 503-593 K and 200-320 bar. The example shows hydrogenation of a fatty acid methyl ester mixed at 523 K and 250 bar. The Cu-Zn-Al catalyst performed quite well compared to various commercial Cu-Cr catalysts.

2.4 Non-Copper Catalysts

2.4.1 Cobalt Catalysts

Texaco patented cobalt catalyst for the production secondary amines such as ditallowamine from fatty nitriles [Zimmerman, 1991]. The cobalt proportion of the catalyst should range from about 30-70% while the amount of promoter may range from about 1-5%. The catalyst promoter was zirconium in a form such as zirconium oxide. The catalyst may be supported upon kieselguhr, alumina, titania or silica. The reaction was preferably conducted at elevated temperatures and pressures. The process was carried out at a temperature in the range of about 130-180^{0}C and a pressure in the range of about 200-1000 psig, to give a yield to secondary amine of about 80%.

2.4.2 Raney Nickel Catalysts

Quite often, highly loaded supported nickel catalysts have the disadvantage that at high temperatures during reduction, calcination or use, the nickel sinters to large crystallites, thereby losing surface area. An alternative for the supported nickel catalysts is Raney nickel. Raney nickel has a high nickel content, i.e. more than 90 wt. %, but the pore sizes of Raney nickel tend to be rather small, namely typically between 4.5 and 6.5 nm, and the
total pore volume is typically about 0.15 ml/g [Reesink et.al, 2003].

Gulf [Arthur et al, 1960] has disclosed catalysts composed of Raney nickel, in preparation of tertiary amines. In Example 4 of this patent, 345 grams of isotridecyl alcohol and 8.5 grams of Raney nickel catalyst were refluxed at a temperature of 240^0C. While 20 grams of ammonia were bubbled therethrough over a period of 5 hours. 30 grams of water were evolved and removed from reaction and 296 grams of product was recovered. 142 grams of the recovered products was tridecyalamines and 51 grams was unreacted alcohol remains. The conversion was therefore 82% and the yield of tertiary amine 58%.

CHAPTER 3

EXPERIMENTAL METHODS AND ANALYSIS

3.1 Introduction

This chapter explains details on the experimental procedure and chemicals used in CuZn/SiO_2 and CuNi/SiO_2 catalysts synthesis. In addition, the synthesized samples were further characterized using variety of analysis techniques. The catalysts then were used in hydrogenation of fatty amines. The catalysts composition studied in this research are listed in Table 3.1.

Table 3.1: Catalysts composition of 25 wt% metal loading supported on silica.

Catalysts code	M1	M2
Metal	Cu, Zn	Cu, Ni
Support	Silica AEROSIL 300	Silica AEROSIL 300
Metal weight loading	25 % metal on support	25 % metal on support
Metal Ratio	3 Cu: 1 Zn	3 Cu: 1 Ni
Metal precursor	Citrate	Citrate

3.2 Materials and Gases

3.2.1 Feed stocks

In the present research work, model compound of fatty alcohol was converted over different solid catalysts to fatty amines. The fatty alcohol was used in the present study:

1. Dodecanol, obtained from Aldrich (Purity 99 %)

3.2.2 Chemicals

A list of the chemicals used in the present research is listed in Table 3.2.

Table 3.2: List of Chemicals

Chemicals	**Brand**	**Formula molecule**	**Molecular weight, g/mol**	**Grade %**
Copper Citrate 2.5 hydrates	Pfaltz&Bauer	$Cu_2C_6H_4O_7.2.5H_2O$	360.00	98.9
Zinc Citrate 2 hydrates	Aldrich	$Zn_3(C_6H_5O_7)_2.2H_2O$	610.40	97.0
Nickel Citrate 2 hydrates	Aldrich	$Ni_3(C_6H_5O_7)_2.2H_2O$	588.00	98.0
Ammonium Hydroxide solution, 28% in water	Aldrich	NH_4OH	38.00	99.9
Ammonia 28% in water	Merk	NH_3	17.03	99.0
Dodecylamines	Aldrich	$C_{12}H_{27}N$	185.35	98.0
Dodecanol	Aldrich	$C_{12}H_{26}O$	186.34	99.0

3.2.3 Support

Table 3.3: Support material used

Type of support	**Trade name**	**Manufacturer**	**Specific surface area m^2g^{-1}**	**Particle Size (nm)**
Silica	Aerosil 300	Degussa	300	7

3.2.4 Gases

Table 3.4: The gases used in preparation, characterization and reaction process

No.	Gases	Brand	Purity (%)
1	Synthetic air (21% Oxygen in Nitrogen)	MOX	99.99
2	Nitrogen	MOX	99.99
3	5% Hydrogen in Nitrogen	MOX	99.99
4	Purified Hydrogen	MOX	99.99
5	Liquid Nitrogen	MOX	99.5

3.3 Equipment

3.3.1 High throughput Reactor used for Liquid Phase Reaction

3.3.1 (a) Catalyst Activation using Pre-treatment Unit

Ex-situ activation of the catalyst with hydrogen at 623 K was carried out in the pre-treatment unit (Figure 3.1). The pre-treatment unit consists of 12 parallel reactors with glass bulbs; controlled gas feed and temperature control (up to 923 K). Approximately 200 mg of catalyst was weighed into the glass pre-treatment reactor (exact weight noted). The reactor was closed by attaching the bulb on top of the pre-treatment reactor and inserted into the pre-treatment unit. The pre-treatment reactor was evacuated and then purged with nitrogen several times to remove the air inside the reactor and catalyst bulb. The gas supply to the reactors was switched from nitrogen to hydrogen and the reactors were heated at 5 K min^{-1} from ambient temperature to

623 K. The catalysts were kept under hydrogen flow at 623 K for 2 hours. After cooling, the reactors were flushed with nitrogen and removed from the reactor rig.

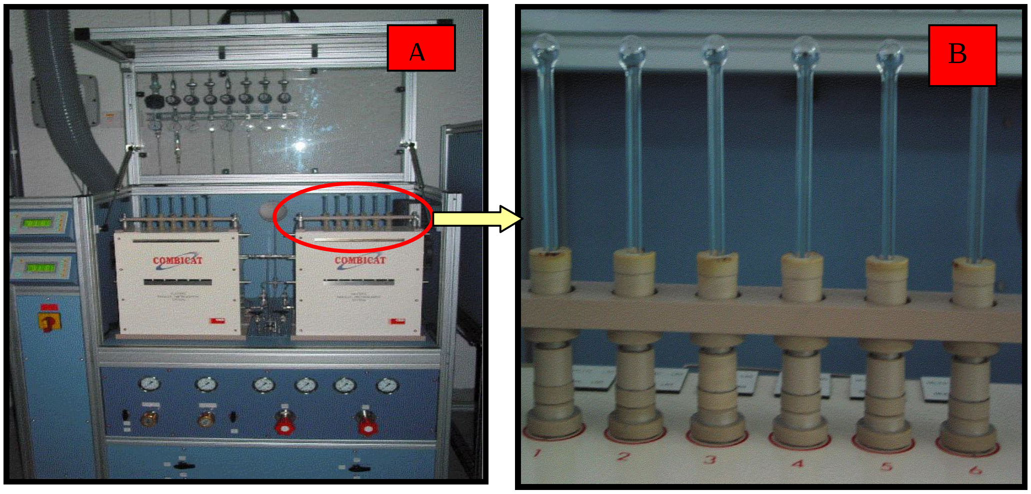

Figure 3.1: Pictures of (A) Pre-treatment unit used for the activation of the catalyst and (B) Individual reactors.

The catalysts were transferred to the bulbs by placing the reactors upside down and the bulbs were sealed with a torch (Figure 3.2 (B)). The catalyst ampoules (Figure 3.2 (C)) were then stored until it is used in the hydrogenation reaction. Instead of directly weighing the catalysts, the empty bulbs before addition of catalyst and the sealed bulbs with catalysts were weighed. The difference between the two bulb weights is the exact weight of the catalyst that was used for the hydrogenation reaction. In this way the actual amount of catalyst introduced in the reactor was weighed and this method excludes the catalyst quantity that sticks to the wall of the pre-treatment reactor due to static charges.

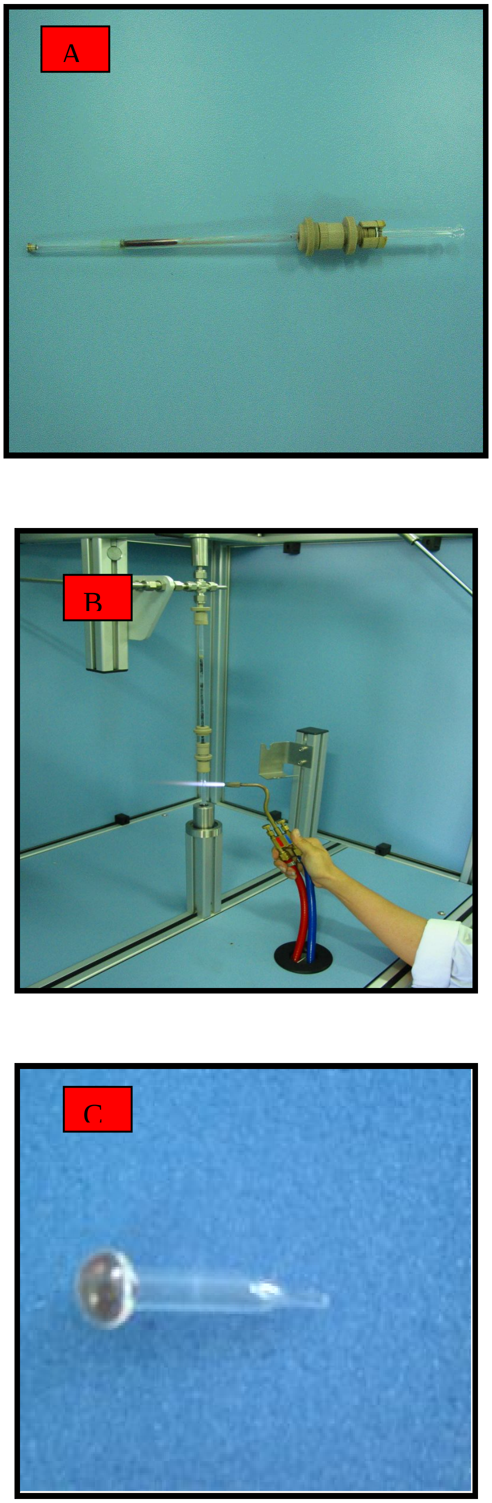

Figure 3.2: Pictures of (A) Pretreatment reactor with approximate 200mg catalyst, (B) Catalyst sealing and (C) Sealed catalyst bulb.

3.3.1 (b) High Throughput Reactor :Oleobed

Figure 3.3 shows a schematic diagram of the Oleobed reactor used for the activity test of the catalysts on the hydrogenation of fatty alcohol to fatty amines. The Oleobed reactor system (Figure 3.3(A)) consists of 12 parallel reactors, operating at high pressures (maximum: 300 bar) and high temperatures (maximum: 573 K) and equipped with an overhead stirrer.

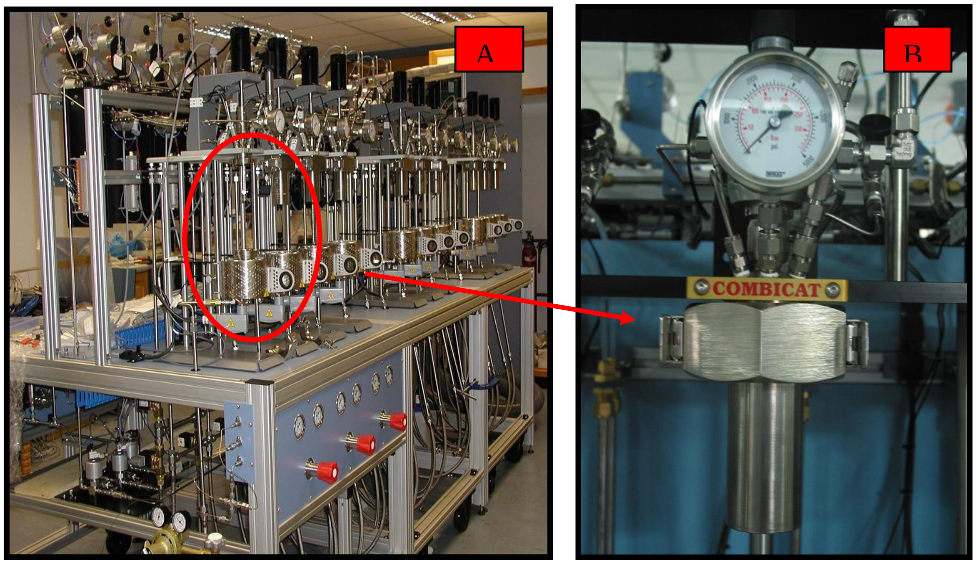

Figure 3.3: Pictures of (A) Twelve parallel oleobed reactors (B) Individual sealed reactor.

The inner diameter of the reactors is 42 mm. A minimum working volume of 50 ml is possible with a 42 mm liner. This represents a good compromise between compactness and having sufficient volume for accurate hydrogen uptake and temperature measurement. Reactors will be individually sealed using a standard split-seal design from Parr Autoclaves.

Each automated reactor is capable of individual heating (Figure 3.3(B)), allowing isothermal operation to a maximum temperature of 573 K. The overall process of experiment was easily traceable and stored in software up to 60 days (Figure 3.4). Material of construction is Hasteloy 276. Designated pressure is 250 bar and kalrez O-ring was found to be the best sealant.

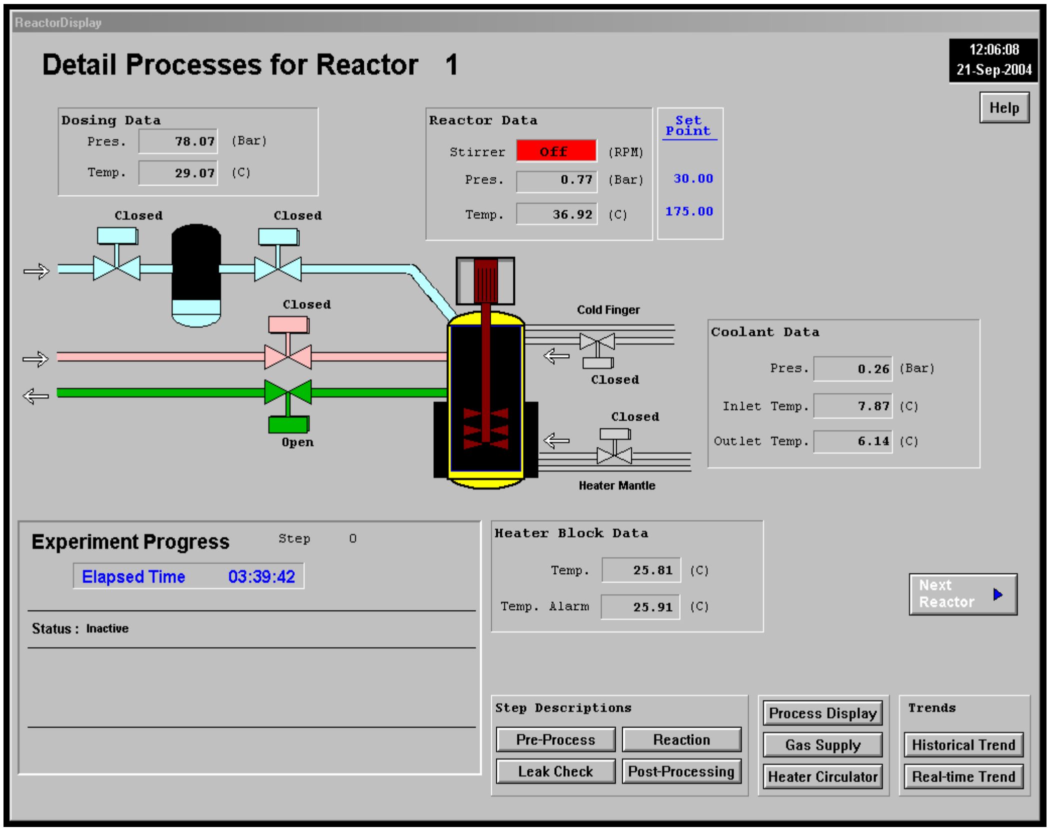

Detail Processes for Reactor 1

12:06:08
21-Sep-2004

Dosing Data
Pres. 78.07 (Bar)
Temp. 29.07 (C)

Reactor Data
Stirrer Off (RPM)
Pres. 0.77 (Bar)
Temp. 36.92 (C)

Set Point
30.00
175.00

Coolant Data
Pres. 0.26 (Bar)
Inlet Temp. 7.87 (C)
Outlet Temp. 6.14 (C)

Experiment Progress
Step 0
Elapsed Time 03:39:42
Status : Inactive

Heater Block Data
Temp. 25.81 (C)
Temp. Alarm 25.91 (C)

Figure 3.4: Automated autoclave control during experiment process.

During the reaction, the pressure was kept constant by the gas dosing system. Gas consumption by reaction caused the pressure in the reactor to drop below the set point pressure, at which a valve between the reactor and the gas dosing vessel opened for a short time to replenish hydrogen. Such a system is also known as “hydrogen-on-demand” system; in which reactors' pressure (amount of hydrogen) are kept consistent throughout the experiment.

Click on buttons below to select the correct scale

17:34:31
28/05/2004

HistR2DosingPressure 115.08 106.48
HistR2DosingTemp 23.15 22.50
HistR2ReactorPressure 0.79 0.79
HistR2ReactorTemp 23.52 22.36
HistR2SetPres 100.00 100.00
HistR2SetTemp 250.00 250.00
HistR2MantleTemp 23.15 22.31

Off Off HistR2DosingInlet
Off Off HistR2DosingOutlet
Off Off HistR2DirectFeed
On On HistR2Vent
Off Off HistR2ColdFinger
Off Off HistR2MantleCooling

08:01:21
17:01:25

Use the scooter buttons above and below to select data and zoom in/out

08:01:21
17:01:25

Use the button below to save data to a CSV file

Filename: C:\COMBICAT OLEO\PERFORMANCE TESTS\280504-R1

Historical Trend for Reactor 2

Figure 3.5: Experimental profile, computed by software.

At all the times the pressure in the gas dosing vessel was 10 bar higher than the reactor pressure to allow flow from the dosing vessel to the reactor. The amount of gas consumed by reaction can be calculated from the reactors' profiles (Figure: 3.5) and temperature in the gas dosing vessel. When the pressure in the gas dosing vessel dropped below the reactor pressure ± 2 bar, the gas dosing vessel was refilled automatically to the gas dosing set point pressure. At the end of the reaction, the gas dosing was stopped and fast mantle cooling was made possible by a water chiller (brand: Julabo). The samples were collected, filtered and analyzed by NMR and FTIR.

3.4 Preparation of Bimetallic Catalysts on Silica Support via Citric Acid Route

3.4.1 General Introduction

The preparative variables in catalyst preparation have greatly influenced the characteristic of the resulting catalysts, such as dispersion of active component, average particle size and particle size distribution.

Citrate chelated precursor was chosen because previous work in industry and academia has shown that catalyst preparation with some specific chelated metal complexes results in catalyst with a high dispersion of small supported metal (oxides) particles with a narrow particle size distribution. The chemical natures of these specific chelate precursors enable them to interact with hydroxyl group on the surface via hydrogen bonding. Besides citrate, other chelating ligands frequently used for these purposes are EDTA, NTA (Nitrilo Tri-acetic Acid) and their structural analogues [Lensveld *et al.*, 2002]. With weakly interacting the nitrate precursor forming a complex with citric acid, the mixture of metal nitrate salt solution was deposited on the surface of the support which is silica in this work. As during deposition and drying, the pH of the wet composite between silica and the various ionic species will greatly change. It is thus imperative to characterize the solid precursor for the existence of chelating metal compounds on its surface. The following subsequent thermal treatment steps will depend on their redox kinetics which is strongly dependent on the type of ligands of the organic acid. It can be easily de-ligand and form free acid at pH values where the non dissociated acid is stable with respect to its salts (weak organic acid vs. strong mineral acid from hydrolyzing metal nitrate species).

The activity of solid catalyst is usually proportional to the active surface area per unit volume of catalyst. It is consequently desirable to apply the active component(s) as uniformly or as disperse as possible over the surface of a support in order to achieve an optimal dispersion of the catalytically active component(s) while also reducing sintering phenomena. In a supported metal catalyst system, the better thermostable and well dispersed metal crystallites on the support attained have been small enough in nano-scale [Sharifah Bee, 2001]. The silica Aerosil 300 with the specific surface area of 300 m^2/g was used to allow more loading of the active component onto the surface of the support using slurry method or can be also called wet impregnation compared to incipient wetness impregnation which is more to pore filling concept and metal deposition is limited to pore size of the support. However, it is not necessary that higher loading of active component result in higher performance of the catalyst but depends more on the nature of the catalyst active sites and the reaction itself. The methodology is basically divided into two sections namely preparation of metal salt solution or metal precursor and the preparation of catalyst.

3.4.2 Preparation of metal salt solution (catalysts precursor)

Two solutions were prepared separately by dissolving the salt in NH_4OH solution. First solution contained X mol of copper citrate 2.5 hydrates dissolved in Y ml 28% NH_4OH, while second solution contained X mol of metal citrate that dissolved in Y ml 28% NH_4OH. The concentration of both solutions fixed as 0.2 g/ml. The mixture was magnetically stirred. The solution prepared was calculated as 25 weight percent metal on support at 3Cu: 1M atomic ratio. The details of solution preparation are shown in Table 3.5. Both copper and metal salt solutions prepared in previous step were mixed and stirred for 5 minutes. The same method of metal solution preparation applied to both samples in this research. The procedure is illustrated in Figure 3.6 and 3.7.

Table 3.5: Details on metal salt solutions preparation for respective samples.

Metal loading (Weight %)	Metal salts	Amount (g)	NH_4OH (ml)	Concentration (g/ml)	Colour of solution
25	Copper Citrate	11.2	55.8	0.2	Royal blue
	Zinc Citrate	4.4	22.1	0.2	Colourless
25	Copper Citrate	11.5	57.6	0.2	Royal blue
	Nickel Citrate	4.1	20.5	0.2	Colourless

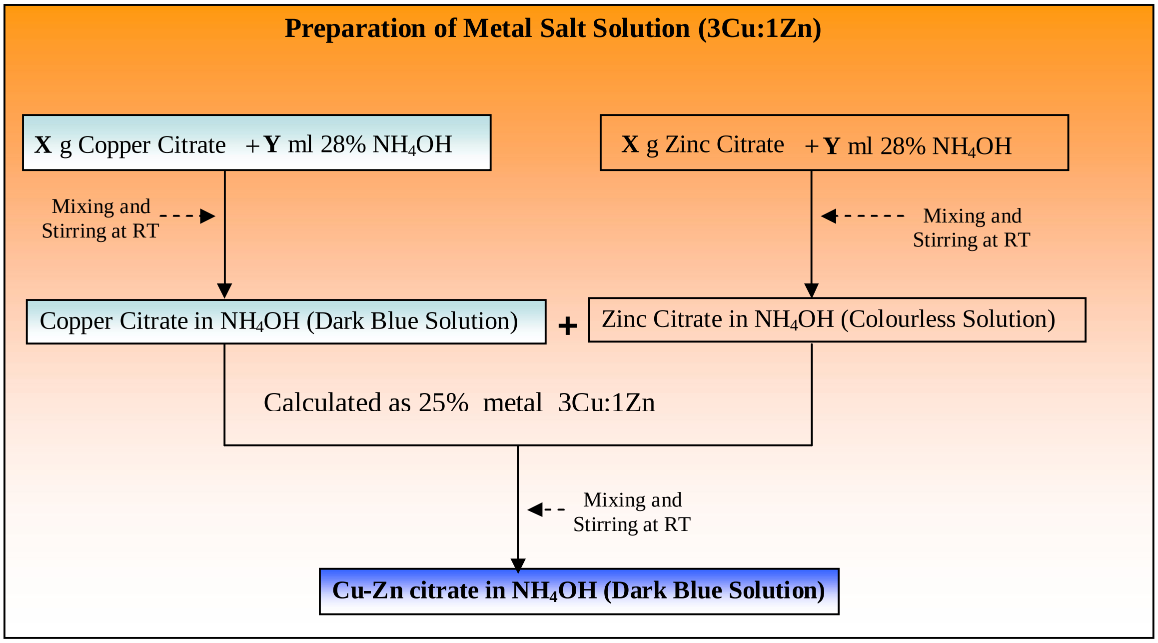

Figure 3.6: Schematic diagram preparation of 25% metal salt solution (precursor) 3Cu:1Zn

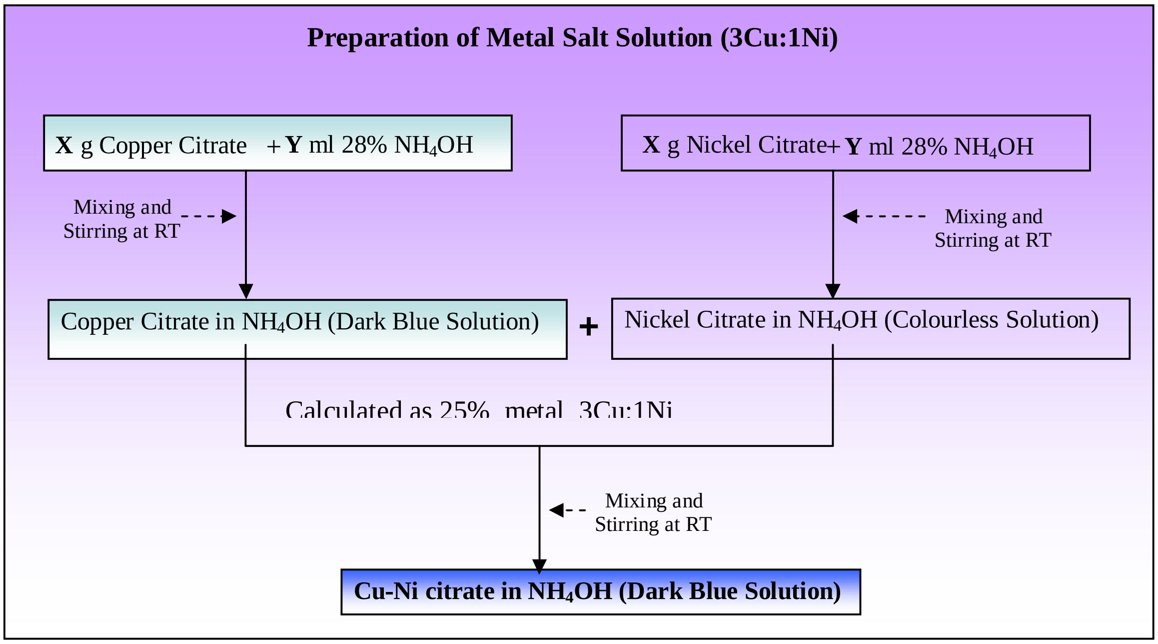

Figure 3.7: Schematic diagram preparation of 25% metal salt solution (precursor) 3Cu:1Ni

3.4.3 Catalyts preparation

The preparation procedure of samples is illustrated in Figure 3.6 and Figure 3.7. 20 g of silica (Aerosil 300) was weighed and subsequently pre-wetted using distilled water with stirring for 5-7 min. The Cu-Zn and Cu-Ni metal solution mixtures prepared in metal salt solution preparation step were poured into the pre-wetted support respectively and stirred using the magnetic stirrer for 5-10 min in order to form homogenous slurry.

Both the homogenous slurries were dried using spray dry (Figure 3.8). Drying the slurry prepared by standard method (air oven) met with some difficulties due to the inhomogeneous metal dispersion on the support and the different concentration gradients of the dried material formed after the drying step. Therefore a good and careful drying procedure required avoiding above phenomenon. Spray drying is essentially an improved rapid and aggressive evaporation method from furnace drying. It is an ideal process where the end product has smaller particle size distribution and well dispersed active component at early stage prior to calcination. Spray drying involves the disintegration of the Cu-Zn and Cu-Ni gels into an aerosol of droplets followed by contacting the droplets with hot air at 373 K in a drying chamber. The sprays are produced by heated nozzle atomizer using the instantaneous evaporation of some solvents of the gel as driving force for particle separation.

Prior to spray drying, approximately 200 ml of deionized water was added to dilute the slurry to prevent nozzle blockage. Evaporation of moisture from droplets and formation of dry particles proceed under controlled temperature and airflow conditions. A fine and physically homogeneous light blue powder was continuously discharged from the drying chamber and collected in drying pot. The dry light blue powder was subsequently calcined in static oven at 723 K for 2 h with heating rate of 2 K min^{-1}. Dark brown powder was formed after calcination.

Table 3.6: List of catalysts prepared

Catalyst	Support	Metal loading	Catalyst Code
3Cu1Zn	Silica	25 wt%	M1
3Cu1Ni	Silica	25 wt%	M2

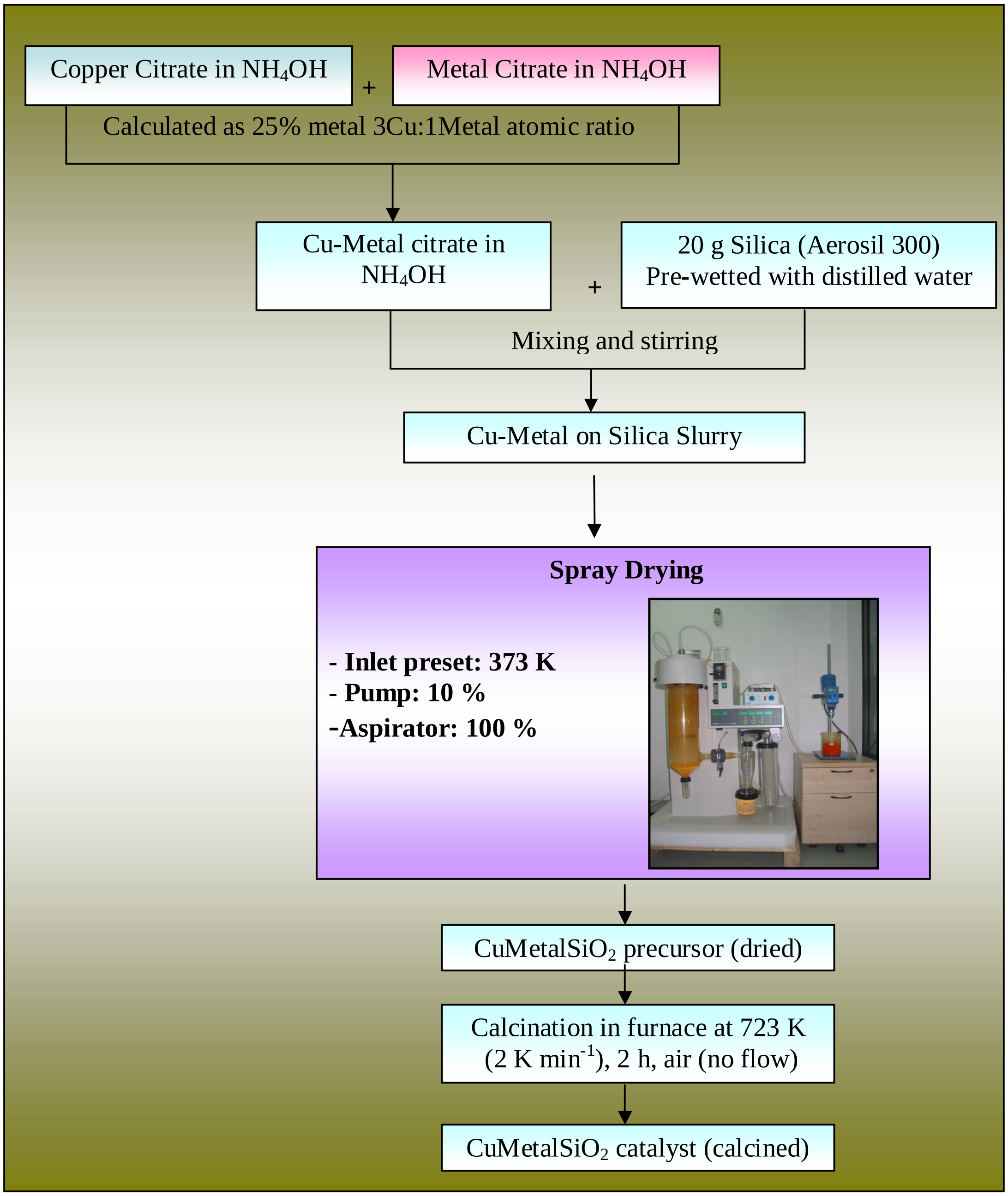

Figure 3.8: Flow diagram catalysts preparation

3.5 Characterization Techniques

This section discusses the type of characterization methods done in the quest to understand the properties of proprietary catalyst developed in this work. Therefore, the basic concepts of characterization techniques as well as the instruments used will be briefly described.

3.5.1 Structural Analysis

3.5.1 (a) Scanning Electron Microscope (SEM) and Energy Dispersive X-ray Analysis (EDX)

The BET analysis is important to measure the surface area of metallic phase; however it cannot reveal the breadth of the particle size accurately. This piece of information is useful because it provides useful clues as to the way the particles are formed. The best way of observing the particle size is by transmission electron microscopy (TEM); since this method can detect particles size as small as 1 nm. However, the instrumentation is very sophisticated and expensive. Therefore, the next best method available *i.e.* scanning electron microscope with EDX, which reveals details of particles not smaller than 10 nm, was used.

Scanning Electron Microscopy (SEM) is capable of producing images of the morphology of the particles and the surface topology of the crystalline materials. Scanning electron microscopy is used for inspecting topographies of specimens at very high magnifications. SEM magnifications can go to more than 300,000X but most semiconductor manufacturing applications require magnifications of less than

3,000X only. SEM inspection is often used in the analysis of die/package cracks and fracture surfaces, bond failures, and physical defects on the die or package surface. The information yields from the SEM are listed in Table 3.7.

Table 3.7: Information from SEM analysis

Information	Details
Topography	The surface features of an object or "how it looks", its texture; detectable features limited to a few manometers
Morphology	The shape, size and arrangement of the particles making up the object that are lying on the surface of the sample or have been exposed by grinding or chemical etching; detectable features limited to a few manometers
Composition	The elements and compounds the sample is composed of and their relative ratios, in areas ~ 1 micrometer in diameter
Crystallographic Information	The arrangement of atoms in the specimen and their degree of order; only useful on single-crystal particles >20 micrometers

In scanning electron microscopy, a fine beam of electron is used to scan back and forth across the specimen surface. The low-energy, secondary electrons generated are then collected by a scintillator crystal that converts each electron impact into a flesh of light. Each of these light flashes in the crystal is then amplified by a photo multiplier tube and used to build the final image on a fluorescent screen. The scan of the beam used to form this image is driven in synchrony with that of the electron-exciting beam that scans the specimen, so the resulting image (formed in much the same way as the picture on the television cathode ray tube) is a faithful representation of the specimen surface as imaged by altering size of the area scanned by the scanning beam [FEI Training Module, 1998].

SEM may be equipped with an EDX analysis system to enable it to perform compositional analysis on specimens. EDX analysis is useful in identifying materials and contaminants, as well as estimating their relative concentrations on the surface of the specimen.

EDX Analysis stands for Energy Dispersive X-ray analysis. It is sometimes referred to also as EDS or EDAX analysis. It is a technique used for identifying the elemental composition of the specimen, or an area of interest thereof. During EDX Analysis, the specimen is bombarded with an electron beam. An image of the spatial distribution of each element in the sample can be acquired [FEI Training Module, 1998].

The output of an EDX analysis is an EDX spectrum .The EDX spectrum is just a plot of how frequently an X-ray is received for each energy level. An EDX spectrum normally displays peaks corresponding to the energy levels for which the most X-rays had been received. Each of these peaks is unique to an atom, and therefore corresponds to a single element. The higher a peak in a spectrum, the more concentrated the element is in the specimen.

Experimental Procedure:

The calcined samples were adhered to the aluminium stub using carbon conductive tape. The stub was then mounted on the stub holder and loaded into the chamber. The chamber was evacuated for analysis. Images were recorded with a Quanta 200 FEI microscope instrument and INCA-Suite version 4.02 for EDX analysis. The flowing settings were used are listed in Table 3.8.

Table 3.8: Setting for EDX analysis.

Accelerating volatage	HV 5kV
Detector type	LFD
Working distance	8-10 mm
Spot Size	2.5 – 3
Cone	X-ray

3.5.1 (b) Nitrogen Physisorption Measurements (BET)

From the catalysis point of view, the rate of product formation over a catalyst is a function of the assessable surface area of the active phase for materials not limited by mass transport of reactants to the active phase [Thomas 1997]. Thus it is important to be able to quantify the surface area of this active phase and the adsorptions of the inert gas make this measurement possible. In spite the oversimplification of the model on which the theory is based, The Brunauer-Emmet-Teller (BET) method is the most widely used standard procedure for the determination of the surface area of finely divided and porous material. The BET method is based on the kinetic model of the adsorption process by Langmuir in which the surface of the solid was regarded as an array of adsorption sites. A dynamic equilibrium was assumed between the rate of molecules condensing from gas phase onto the bare sites and the rate at which molecules evaporate from occupied site. The two rates are equal at that stage. To determine the characteristics of the adsorbent, the adsorption and desorption isotherms must be established. The isotherm is the standard volume adsorbed as the function of relative pressure. Relative pressure is defined as the ratio of actual gas pressure over the saturated vapour pressure of adsorbate (P_0), under constant temperature (liquid nitrogen temperature at atmospheric pressure). The isotherm shapes reveal not only the pore structure of adsorbent, but also the adsorption and desorption process. Adsorption isotherms from physisorption, which are shown in Figure (3.9), follow one of the six forms.

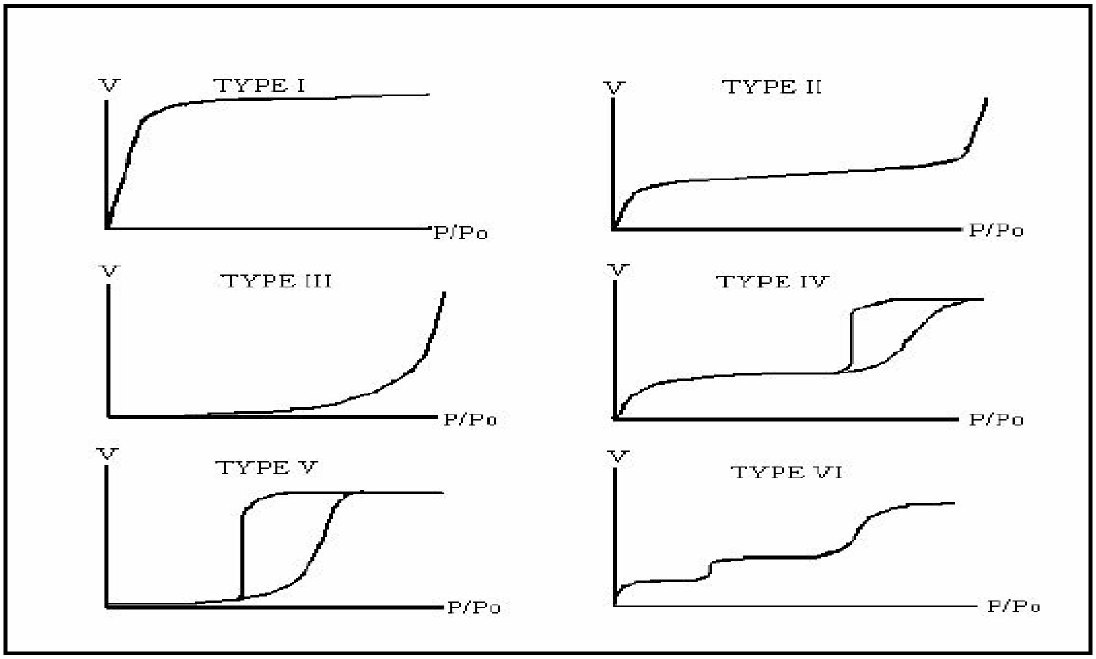

Figure 3.9: Adsorption isotherms types

The first five types were proposed by S. Brunauer, L.S. Deming, W.S. Deming and E. Teller (BDDT) and the sixth isotherm was observed recently. Type I is a Langmuir isotherm with very small pores or microporous adsorbent. The adsorbate uptake rate depends on the accessible microprobe volume instead of the internal surface area at which adsorption occurs by filling micropores in order of increasing size. Sometimes, the hysteresis loop is presented at the near saturation pressure region due to the presence of mesopores with an upper size restriction. Type II and IV isotherms are the forms observed for either nonporous or mesoporous adsorbents with unrestricted monolayer-multilayer adsorption. In the nonporous isotherm, the desorption curve traces the adsorption curve, and the adsorption volume rapidly increases at low relative pressure of less than 0.01 due to the first energetic region interaction followed by the interaction with less energetic regions. When the monolayer of adsorbed adsorbate is completed, multilayers are forming at the sharp knee of the isotherm. As the relative pressure approaches unity, an abrupt rise indicates the bulk condensation of adsorbate gas to liquid. Instead of retracting the adsorption curve, the mesopores or macropores behaviour shows a wide hysteresis loop indicating the filling and emptying of the pores by capillary condensation.

Type III and V isotherms do not have the sharp knee shape, implying stronger adsorbate-adsorbate interactions than adsorbent-adsorbate. Type VI is the isotherm of a nonporous solid associated with layer by layer adsoption on a highly uniform surface. The step’s sharpness is dependent on the system and the temperature. It is also noted that, in some cases, isotherms without hysteresis loops do not show that the adsorbent is nonporous, for instance, adsorbents with conical or close-end pores.

Hysteresis loops are associated with capillary condensation in the multilayer region, pore filling and emptying mechanism of physisorption isotherm. The micropore filling effects occur at the low relative pressure up to a unity relative pressure. Thus, the meniscus begins to form and increases steadily toward the pore entrance with increasing relative pressure. The evaporation process involves the same series of steps in the reverse direction of condensation.

The shape of the hysteresis loop implies the existence of certain states. The major hysteresis loops correspond to different pore shapes, represented in IUPAC, and shown in Figure (3.10).

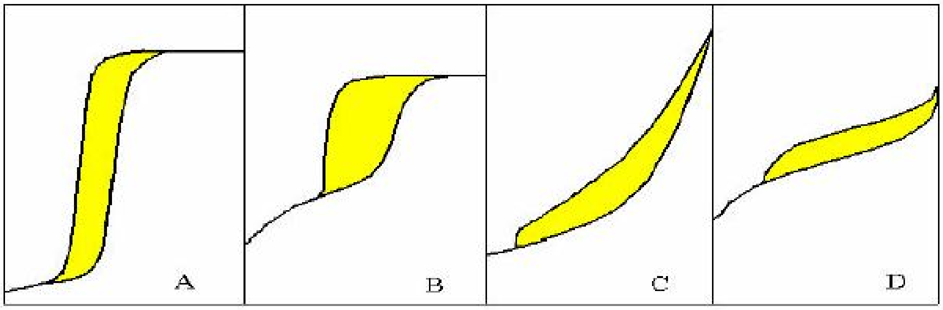

Figure 3.10: Hysteresis loops.

Type A hysteresis is attributed to cylindrical or tubular pore type of adsorbents with a narrow distribution of uniform pores, and is signified by steep and narrow parallel adsorption and desorption curves. Type B has a long flat plateau adsorption with a steep desorption curve. This is a complex structure of pores with interconnected net works or inkbottle shape. Type C presents the aggregates of adsorbents that contain parallel plates, slit shape pores, or wide capillaries (>5000A). Type D is also associated with slit shape pores but contains mainly the pores in micropore region. The lower limit of the hysteresis loop or the closing point is dependent on both of the adsorbate gas and the operating temperature. Increasing temperature will reduce the size of the hysteresis loop. In the case of nitrogen, the hysteresis loop is closed at relative pressure of 0.4. However, most hysteresis loops close before the relative pressure approaches 0.3 in the absence of micropores. Pores can be varied in size and shape from one adsorbent to another. Depending on the shape of either cylindrical pores or slit pores, pore size is expressed in terms of diameter or width. Pores with diameters or widths of less than 20 Å are micropores. Intermediate pores between 20 Å and 500 Å are mesopores, and macropores are the pores with openings exceeding 500 Å.

In spite of the oversimplification of the model on which the theory in based, the B.E.T. method is the most widely used standard procedure for the determination of surface area of finely divided and porous material. The BET equation applicable at low p/p_o range is customarily written in linear form as:

$$\frac{p}{n^{\mathrm{a}}(p_o-p)} = \frac{1}{n_{\mathrm{m}}^{\mathrm{a}}C} + \left(\frac{C-1}{n_{\mathrm{m}}^{\mathrm{a}}C}\right)\frac{p}{p_o} \qquad (3.1)$$

where n^{a} is the amount of the gas adsorbed at the relative pressure p/p_o, $n_{\mathrm{m}}^{\mathrm{a}}$ is the monolayer capacity and C is the so-called BET constant which, according to the BET theory, is related to the enthalpy of adsorption in the first adsorbed layer and gives information about the magnitude of adsorbent-adsorbate interaction energy. If the information is applicable, a plot of $p/[n^{\mathrm{a}}(p_o-p)]$ *vs.* p/p_o should yield a straight line with intercept $1/n_{\mathrm{m}}^{\mathrm{a}}C$ and slope $(C-1)/n_{\mathrm{m}}^{\mathrm{a}}C$. The value of $n_{\mathrm{m}}^{\mathrm{a}}$ and C may then be obtained from a plot of a single line, or regression line, through the points. The volume of the monolayer having been determined allows the surface area of the sample to be determined by a single adsorbate molecule, a value derived from the assumption of close packing at the surface by the formula:

$$\mathrm{a_s\,(BET)} = \frac{n_{\mathrm{m}}^{\mathrm{a}} \,.\, L \,.\, a_m}{m} \qquad (3.2)$$

where a_s is the specific surface area, L is Avogadro’s number (6.023×10 23 mol^{-1}), m is the mass of the adsorbent, and a_m is the cross sectional area of the adsorbate molecule, for which a value of 0.162 nm^2 $molecule^{-1}$ for N_2 is widely accepted. The assumptions in the BET equation break down if the BET plot is not linear, and the plot is usually restricted to the linear part of the isotherm over the p/p_o range of 0.05-0.3.

Experimental Procedure:

All the specific surface areas, pore sizes and pore size distribution for the materials used were analyzed by BET procedure using nitrogen adsorption and desorption. The N_2 adsorption / desorption was done by using Sorptometric 1990 Instrument. Approximately 20-50 mg of the material to be analyzed was placed in a tube of known volume and heated to 393 K (1 K min^{-1}) for degassing under vacuum for 5 hours. After outgassing, the sample was weighed again to determine the actual sample weight. The sample tube was then placed in the analysis station, cooled in liquid nitrogen and a known amount of nitrogen gas was introduced into the cooled tube. After equilibration, the pressure was measured and the sequence repeated with successive pulses of N_2.

3.5.1 (c) X-ray Powder Diffraction (XRD) analysis

X-ray powder diffraction (XRD), being a non-destructive technique, is one of the most frequently applied techniques in catalyst characterization. X-ray with wavelengths in the Å range, is sufficiently energetic to penetrate solid and are well suited to probe their internal structure. XRD is therefore used to identify bulk crystalline phases and to estimate particle sizes.

An X-ray source consists of a target, which is bombarded with high-energy electrons. The emitted X-rays arise from two processes. Electron slowed down by the target emits a continuous background spectrum of Bremsstrahlung or braking radiation. Superimposed on this are characteristic narrow lines. The CuK_{α} line arises when primary electron creates a core hole in the K shell, which is filled by an electron from the L shell (K_{β}: the K-hole is filled from the M-shell electron, etc) under emission of an x-ray quantum [Mohd. Rahim 1993].

Different features of powder diffraction pattern can be exploited in the characterization of material. XRD data are mostly used as a “fingerprint” in the identification of materials (Table 3.9).

Table 3.9: Information contained in the powder diffractogram

Feature	Information
Peak position (2θ value)	Unit Cell Dimension
Non-indexable Line	Presence of Crystalline impurities
Background	Presence of amorphous material
Width of Peak	Crystalline Size
Peak Intensities	Crystal Structure

The diffraction line for a powder sample occurs because of a small fraction of particles oriented in such a way that by chance a certain crystal plane (hkl) is at the right angle with the incident beams for constructive interferences. Diffraction lines from perfect crystals are very narrow, whereas, crystalline size below 100 nm causes broadening due to incomplete destructive interference in scattering directions where the x-ray is out of phase. d_{hkl} for a relatively big crystal can be obtained by using Bragg’s law and assuming first order diffraction:

$$\lambda = 2d_{hkl} \sin\theta;\ \text{with } \lambda = 0.1542 \text{ (for Cu } K_{\alpha}\text{) radiation}$$

If the crystalline is very small (<50nm), then Bragg condition is no longer satisfied, and the residual scattered intensity will be detected at angles away from the Bragg angle. As a consequence, the reflection broadens (as mentioned above). The broadening is related to the average crystallite size by Scherrer equation:

$$D = k\lambda / \beta \,\text{Cos}\,\theta$$

With k constant 0.9, $\lambda = 0.1542$ (for Cu Kα) radiation, and β = true line width

$$\beta = (B^2 - b^2)^{1/2}$$

With B = measured line width, and b = instrumental broadening of diffractometer.

Experimental Procedure:

To identify the crystal lattice dimensions, structure and composition of material, XRD was performed using a Bruker X-ray Diffraction model D-8 equipped with EVA Diffract software for data acquisition and analysis. Data were acquired using a CuK_{α} monochromatized radiation source operated at 40 kV and 40 mA at ambient temperature. The samples were finely grounded and placed in the sample holder, with the powder lightly pressed into place using a microscopic slide. The surface of the sample was flattened and smoothens. The sample holder was then placed in the diffactometer stage for analysis. A continuous 2θ scan mode from 5^0- 80^0 was used for high degree scanning at step time of 15 s and step size of 0.050^0 2 theta. A divergence slit was inserted to ensure that the x-rays focused only on the sample, and not the edges of specimen holder. The diffractograms obtained were matched against the Joint Committee on Powder Diffraction Standards (JCPDS) PDF 1 database version 2.6 to confirm the precursor and catalyst phase.

3.5.1 (d) X-Ray Fluorescence (XRF)

Wavelength-disperse x-ray fluorescence (XRF) is a non-destructive analytical technique used to identify and determine the concentrations of elements present in solid, powdered and liquid samples. XRF is capable of measuring all elements from beryllium to uranium at trace levels often below one part per million. The sample is irradiated by intense x-rays, which cause the emission of fluorescent x- rays using either an energy-dispersive or wavelength-dispersive detector of emitted rays. The elements in the sample are detected by characteristic wavelengths of emitted x-rays and concentration is determined by the intensity of the x- rays [Rousseaou 2001].

In XRF, the atom absorbs the x-ray by transferring all of its energy to an innermost electron. During this process, the primary x-ray, which has sufficient energy, ejected the inner orbital electrons and creat vacancies. These vacancies present an unstable condition for the atom. As the atom returns to its stable condition, electron from the outer shells are transferred to the inner orbital and in this process give off a characteristic x-ray whose energy is the difference between the two binding energies corresponding shells (Figure 3.11). Because each element has a unique set of energy levels, each element produces x-rays at a unique set of energies, allowing one to non-destructively measure the elemental composition of a sample. The process of emissions of characteristic x-rays is called “X-ray Fluorescence” or XRF.

For a particular energy (wavelength) of fluorescent light emitted by an element, the number of photons per unit time (generally referred to as peak intensity or count rate) is related to the amount of that analyte in the sample. The counting rates for all detectable elements within a sample are usually calculated by counting, for a set time, the number of photons that are detected for the various analytes "characteristic" x-ray energy lines. Therefore, by determining the energy of the x-ray peaks in a sample's spectrum, and by calculating the count rate of the various elemental peaks, it is possible to qualitatively establish the elemental composition of the sample and to quantitatively measure the concentration of these elements.

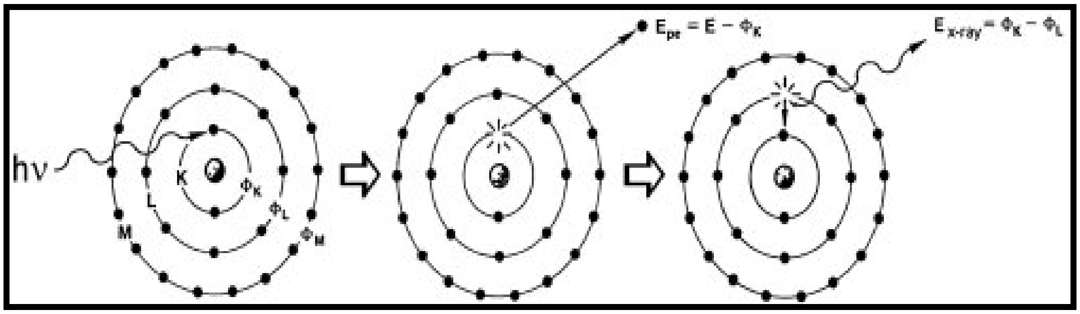

Figure 3.11: The excitation energy from inner atom is transferred to one of the outer electrons causing it to be ejected from the atom.

Experimental Procedure:

The XRF analysis was performed using a Bruker X-ray Fluorescence model S4 Explorer (made in Germany) equipped with Spectra plus software for data acquisition and analysis. Data were acquired using x-ray generator using source operating at 1 kW at ambient temperature. The analysis was performed using semi-quantitative method. Samples were finely grinded using mortar and placed in the sample cup (40 mm diameter) installed with 6 μm mylar film at the bottom. The x-ray was generated from x-ray tube and passed through the beryllium oxide window slit before striking the sample. Then, the sample reflected the x-ray photon and the photon passed through the collimator before hitting the synthetic multilayer crystal. The crystal consisted of lithium fluoride and pentoerythrite elements. This crystal was used to diffract polychromatic x-ray beam coming from the sample into a monochromatic light-beam before sending it to detector. Then, the detector converted the energy of the x-ray photon into a measurable energy form.

3.5.1 (e) Diffuse Reflectance of UV-Visible

Ultraviolet and visible spectroscopy is a suitable technique for studying electronic transitions. The absorption of UV or visible radiation corresponds to the excitation of outer electrons. There are three types of electronic transitions;

- (i) Transitions involving π, σ and n electrons.

All possible transitions are shown in Figure 3.12.

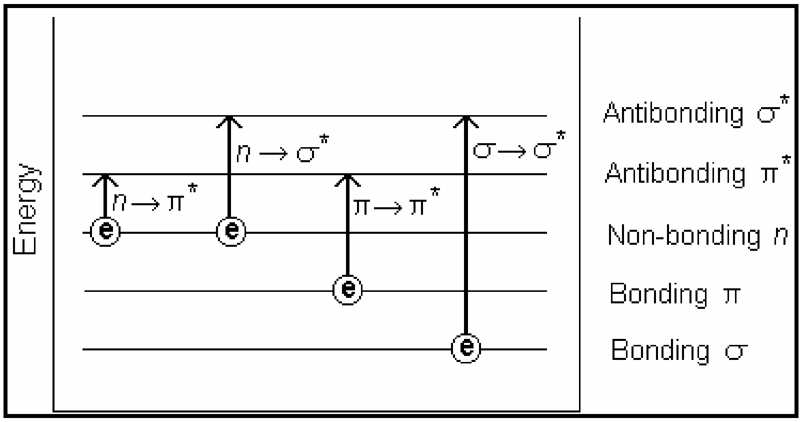

Figure 3.12: Possible electronic transitions of π, σ and n electrons.

Most absorption spectroscopy of organic compounds is based on n-π* or π-π* electronic transitions. This is because the absorption peaks for these transitions fall in an experimentally convenient region of the spectrum (200-700 nm). These transitions need an unsaturated group in the molecule to provide the π electrons. On the other hand, σ-σ* transitions require a large energy with absorption maxima that are not seen in typical UV-vis spectra. n-π* transitions usually need less energy than σ-σ*. The number of organic functional groups with n-σ* peaks (150-250 nm) in the UV region is small.

- (ii) Transitions involving charge-transfer of electrons

Many inorganic species show charge-transfer. For a complex to demonstrate charge-transfer behaviour one of its components must have electron donating properties and another component must be able to accept electrons. Electronic transition in this case is a transfer of an electron from the donor to an orbital associated with the acceptor. Three types of charge-transfer are known: 1) Ligand to metal charge transfer (LMCT). 2) Metal to ligand charge transfer (MLCT). 3) Metal to metal charge transfer (MMCT). The first two types can be detected in the range 200-400 nm, the last one in the range 400-800 nm.

- (iii) Transitions involving d and f electrons

The transition metal ions are characterized by a configuration $3d^n$ or $4d^n$ or $5d^n$. The d-d transitions give information on oxidation states and symmetry of the transition metal ions. These transitions found in the UV range and more often in the visible part of the spectrum, and are responsible for the colours of many transition complexes.

Experimental Procedure:

Diffuse reflectance of UV/Vis was performed with Perkin Elmer Lambda 35 spectrometer equipped with a diffuse reflectance sphere (spectralon integrating sphere). The spectra were recorded from 250 nm to 1000 nm with scan speed of 960 nm min^{-1}. The slit width is 1.00 nm. A commercial sample of copper citrate was used as reference.

3.5.1 (f) Fourier Transformed Infrared Spectroscopy (FTIR)

Infrared Spectroscopy is the study of the interaction of electromagnetic radiation with a chemical substance. The nature of the interaction depends upon the properties of the substance. When radiation passes through a sample (solid, liquid or gas), certain frequencies of the radiation are absorbed by the molecules of the substance leading to the molecular vibrations. The frequencies of absorbed radiation are unique for each molecule, which provide the characteristics of a substance. The electromagnetic spectrum covers an immense range of wavelengths. The infrared regions are classified as follows:

(i) Near Infrared 12500 to 4000 cm^{-1} (0.8 to 2.5 um)
(ii) Mid Infrared 4000 to 200 cm^{-1} (2.5 to 50 um)
(iii) Far Infrared 200 to 12.5 cm^{-1} (50 to 800 um)

The functional group region (4000-1500 cm^{-1}) – Peaks in this region are characteristic of specific kinds of bonds, and therefore can be used to identify whether a specific functional group is present. The fingerprints region (1500-400 cm^{-1}) – peaks in this region arise from complex deformations of the molecule. They may be characteristic of molecular symmetry or combination bands arising from multiple bonds deforming simultaneously.

Any absorption band can be characterized by two parameters: the wavelength at which maximum absorption occurs and the intensity of absorption at this wavelength. In an absorption spectrum, the y-axis measures the intensity of the band, which is proportional to the number of molecules observed. This principle consequently leads to quantitative analysis. Intensity of IR absorption is illustrated as below:

Transmittance $T = I/I_o$

Absorbance $A = \log(1/T) = \log(I_o/I) = ecL$

Where

I_o = Intensity of incident radiation

I = Intensity of transmitted radiation

e = molar extinction coefficient

c = concentration (mole/l)

L = sample pathlength (cm)

FT-IR spectroscopy is certainly one of the most important analytical techniques today. One of its great advantages of is that any sample in any state can be studied: gas, liquids, solution, powders, films and surfaces can be examined by a suitable choice of sampling technique.

The energy at which any peak in an absorption or transmission of FT-IR spectrum appears corresponds to the frequency of vibration of a part of the sample molecule. This provides information on the functional groups in the molecule. From the frequencies of the absorption, it is possible to determine whether various functional groups are present or absent. This forms the basis of analyses of the molecular structure of single and multi component materials. The movements of the atoms of a molecule during vibration can be classified as bond or angle deformations.

FT-IR spectroscopy was carried out to determine the molecular functional groups embedded in the catalyst. FT-IR is also an important method for structure characterization giving information on short range and long range bond order caused by lattice coupling and electrostatic and other effects. The characteristic group frequencies corresponding to the citric acid molecule were used to determine whether the catalyst kept its properties after heterogeneization and during all the steps of the catalytic procedures.

Experimental Procedure:

Fourier transform infrared transmission (FTIR) spectra were recorded with a Bruker spectrometer model IFS 66v/s, using the technique of KBr pellets and working with a resolution of 4 cm^{-1} in the Middle range. Before analysis, air evacuation was done under vacuum (5 mbar) for 15 minutes.

3.5.2 Thermal Analysis

3.5.2 (a) Thermo gravimetric Analysis (TGA)

The thermogavimetric analysis (TGA) is basically quantitative nature in that the mass-change can be accurately determined. TGA measures the mass of a sample (usually a few mg) as a function of temperature while the temperature changes according to a temperature program. The quantitative nature of TG can be further exploited to enable stoichiometric equation for the decomposition mechanism to be postulated. The mechanism may then be confirmed by analysis of the solid and gases of the decomposed product.

Results from thermogravimetric experiment can be presented in many ways. The most common versions are mass or percent as the abscissa and temperature or time as the ordinate. The point of inflection in the TG curve is associated with completions of steps in a series of reactions, or changes in the mechanism during a reaction. The relationship between the rate of weight change and temperature or time is expressed by derivative thermogravimetric curve [Dallimore 1996]. The DTG curve can be produced from the data processed from TG. The same equipment is used but instead of plotting mass against time, the results will produce the rate of mass change against time. Each stage in multiple stage decomposition can be plotted as fraction decomposed [Knozinger 1996].

Experimental Procedure:

To investigate the thermal stability of the catalyst, the measurement was done using Mettler Toledo TGA/SDTA 851^e unit, equipped with a microbalance and furnace capable of heating up to 1873 K. The Mettler Toledo balance technology on this unit allows the horizontal flow of gases that minimize chimney effect and more stable weight signal.

Nitrogen was necessary to flow continuously at 50 cm^3 $min^{-1,}$ to avoid harmful gases from flowing back towards the microbalance.

In a typical measurement, about 50 mg samples were measured in an open alumina crucible (70 µl), at an elevated temperature from ambient to 973 K at 5 K min^{-1}. Synthetic air was used as reactive gas at a constant flow rate of 50 cm^3 min^{-1}. The results were evaluated with the V7.01 STAR^e software packages. The DTG curves were calculated as derivatives of the TG curves.

3.5.2 (b) Different Calorimetric Analysis (DSC)

Differential Scanning Calorimetry (DSC) is a technique in which the differences in an energetic behavior between the substance and the reference materials are measured as a function of the temperature when the substance and the reference undergo a controlled temperature program. The amount of energy which has to be supplied to or withdrawn from the sample to maintain zero temperature differentials between the sample and the reference is the experimental displayed as the ordinate of the thermal analysis curve [Daniels 1973].

This method allows accurate evaluation of small differences between the actual sample temperature and the programmed sample temperature. It is an extremely valuable technique for quantitative measurement of heats of reaction and transition, specific heats etc. Furthermore, DSC measurement maybe made isothermally or at very low heating rates without loss of sensitivity.

Experimental Procedure:

The analysis was performed using a METTLER TOLEDO DSC821^e equipped with an intra-cooler. The system was automated with a sample robot. The DSC was calibrated (temperature and heat-flux) by melting Indium. The purge gas used was nitrogen at 50 ml min^{-1}. The results were evaluated with the V7.01 STAR^e software package.

Samples of about 9-10 mg were measured in hermetically sealed 40 μl aluminum standard crucibles in a self-generated atmosphere and an empty sealed aluminum crucible served as reference.

The self-generated atmosphere was released to the environment by piercing a 50 μm hole in the aluminum lid of a sealed crucible. The DSC temperature program was run dynamically from ambient to 823 K at a heating rate of 5 K min^{-1} under compressed air with a flow rate of 50 ml min^{-1}.

3.5.2 (c) Temperature Programmed Reduction (TPR)

Temperature-programmed reduction (TPR) is a class of technique in which chemical reaction is monitored while the temperature increased linearly with time. These techniques are applicable to real catalysts and have the advantage of being experimentally simple and inexpensive in comparison to many other spectroscopies. Interpretation in a qualitative base is rather straight forward.

The basic set up for TPR consists of a reactor and a thermal conductivity detector (TCD) to measure the hydrogen content in TPR of the gas mixture before and after reaction. More sophisticated TPR equipment consists of a mass spectrometer for the detection of reaction products. The area under a TPR curve represents the total hydrogen consumption and is commonly expressed in terms of moles of H_2 consumed per g of sample. TPR provides a quick characterization of metallic systems. This method gives information on the eventual degree of reduction of the phases present.

For bimetallic catalysts, TPR pattern often indicates if the two components are mixed or not.

Experimental Procedure:

TPR was carried out to determine the oxidation state and the chemical nature of metal species of the supported catalysts. Measurement was carried out in a Thermofinnigan TPDRO 1100 instrument. The samples were first calcined ex-situ in a furnace at 473-723 K for 2 hours. Then, approximately 100-300 mg of the catalyst was pre-treated in a tubular quart reactor, by heating the material from room temperature to 383 K at 10 K min^{-1} under 20 cm^3 min^{-1} N_2 for 20 minutes. This step is crucial in eliminating any possible contaminants present on the surface of catalyst. The material was cooled to room temperature again after pre-treatment. TPR measurement was carried out by flowing 20 cm^3 min^{-1} H_2 (5% H_2 in Nitrogen) from room temperature to 1173 K at a heating rate of 10 K min^{-1} and hold isotherm, under flow of gas for 20 minutes. The reduction was measured by monitoring the hydrogen consumption with the TCD detector. The water produced during the reduction was trapped in a 5 Å molecular sieve column. In order to quantify the degree of reduction, CuO standard was used for calibration of the peak areas.

CHAPTER FOUR
RESULTS AND DISCUSSION

4.1 Introduction

The diversity in compositions, structures, and treatments in heterogeneous catalyst pose a major challenge in structural characterization. Therefore the demonstration of the properties of synthesized materials and their behavior as catalysts should be accompanied by a suitable methodology for their characterization.

This chapter particularly discusses results on various catalyst characterization techniques that have been described in Chapter Three. The results and discussion are divided into two categories namely the structural analysis and the thermal analysis. The structural analysis studied the physical and chemical characteristics of samples such as elemental composition, crystalinity, surface area, porosity and other structural properties while the thermal analysis studied the samples behaviour towards the heat treatment under oxidation and reduction.

The catalysts prepared and characterized are listed and coded in Table 4.1. The catalysts selection criteria is based on the previous studied which executed by COMBICAT research group that claimed catalyst CuZn/SiO_2 with 3:1 ratio, temperature at 723 K and weight at 25% was one of the best catalyst using high throughput experimentation (HTE) testing result for hydrogenolysis reaction to produce fatty alcohol from fatty acid methyl esters. Thus, Cu-Ni catalyst system was chosen as it showed good performance in hydrogenation of fatty alcohols to fatty amines in many research works.

Table 4.1: List of catalysts prepared and characterized.

Catalyst Code	Composition	Calcination Temperature
M1	25wt% 3Cu/Zn/SiO_2	723 K
M2	25wt% 3Cu/Ni/SiO_2	723 K

Thermal analysis is used to identify the sequence of events during calcination step which involved the transformation of precursor into oxides, an active form of catalyst before further reduction prior to the reaction. A complete gasification of all volatile ligands without compromising the interaction of the active oxide with support should be achieved after calcination. It is also a step at which the bulk as well as surface structure of the supported oxide catalysts finally forms. The new structures that subsequently appear during the calcinations step are at first poorly organized, but then with increasing temperature become progressively organized and evolve towards a state close to the final product.

In the preparation of active and selective hydrogenation catalysts, it is important to achieve nano-scale copper oxide (supported or unsupported). Citrate precursor used in this experiment has also been widely used to synthesize oxide nanoparticles for its many advantages such as homogenous mixing of components on an atomic scale, good control of the stoichiometry and ease of synthesis of the complexes [Wang *et. al* 2003]. One of the most critical preparation steps in this scope is the calcination procedure. The lowest possible temperatures to achieve complete conversion of the precursor into oxides are required.

In the present research, thermal behavior of each precursor prepared by standard method and various modifications applied during preparations step were analysed in order to identify the effect of each preparation variable to the decomposition of precursor and the reduction behavior of the samples. Table 4.2 shows the purpose of thermal analysis in this study. This section will discuss about the event that might be developed during real calcination.

Table 4.2: Purposes of analysis using techniques of TGA-MS, DSC, and TPR

Thermal Analysis	Experimental conditions	Purposes
DSC	Temp = 298 K to 823 K Rate = 2 K/min Gas = Compressed Air	To know the enthalphy of reaction happened during precursor decomposition.
TGA-MS	Temp = 298 K to 973 K Rate = 2 K/min Gas = Compressed Air	To observe the weight loss as function of mass loss, temperature, and gas evolve during real calcinations.
TPR	Temp = 298 K to 1000 K Rate = 2 K/min Gas = 5% Hydrogrn in Nitrogen	To analysed the reduction behaviour of samples.

4.2 Structural Analysis

4.2.1 X-ray Fluorescence (XRF)

XRF analysis is used to measure the bulk composition of the element and metal oxide in all samples. The sample preparation method used is loose powder and the systematic error of overall composition of theoretical and experimental is estimated to be about 5 % or less. Even though other preparation methods available are more accurate such as pressed pellet and fuse bead but the quantity of samples are inadequate for the former and incompatible for the next measurement. In quantitative XRF analysis, the systematic error is present when a certain bias exists in the results, as could happen if a badly determined calibration line is used. This bias is a measure of the difference between the given and the calculated concentration value. Systematic error not only depends upon errors that arise from the conversion of intensities into concentrations (calibration), but also from those produced by the sample preparation, the instrument and the analytical method used for the correction of matrix effects [Rousseaou 2001].

Tables 4.3 and 4.4 show the theoretical and experimental composition measurements using XRF analysis. Those data are presented in weight percent of elements and metal oxides. The deviation between expected and experimental compositions is within acceptable limit given the errors in determination and in the weighing of the educts. The usefulness of the elemental analysis is demonstrated with sample M2 revealing a bit higher metal loading than suspected. The ratio of metal oxides of copper to nickel is no longer 3:1 but 3.2:1 (Table 4.4). The most likely cause of this deviation is an error in sample preparation. The uncertainty introduced by this error source may limit considerably the accuracy and precision of the analytical results if we are not attentive to it [Rousseaou 2001]. The oxygen abundance is hypothetical and has not been determined experimentally. It is assumed that all cationic species are present in their highest oxidation states from which the expected oxygen content is estimated.

Table 4.3: Calculated percentage weight of metal in samples M1 and M2

Sample	Weight % of Cu		Weight % of Zn		Weight % of Ni		Weight % of Si		Weight % of O		Total Weight % of Metal	
	Cal.	Exp.	Cal.	Exp.	Cal.	Exp.	Cal.	Exp.	Cal.	Exp.	Cal.	Exp.
M1	15.50	15.70	5.40	5.00			35.10	34.60	39.90	44.60	20.90	20.70
M2	16.10	16.50			4.90	5.00	35.10	32.20	39.90	43.00	21.00	21.50

Table 4.4: Calculated percentage weight of metal oxide in samples M1 and M2

Sample	Weight % of CuO		Weight % of ZnO		Weight % of NiO		Weight % of SiO_2		Total Weight % of Metal Oxides	
	Cal.	Exp.	Cal.	Exp.	Cal.	Exp.	Cal.	Exp.	Cal.	Exp.
M1	18.60	19.60	6.40	6.20			75.00	74.10	25.00	25.80
M2	19.00	18.70			6.00	5.80	75.00	68.90	25.00	25.00

4.2.2 X-ray Powder Diffraction (XRD)

The structural properties and phase integrity of the support in the solid precursors and in the calcined samples M1 and M2 are evaluated using X-ray powder diffraction. Tables 4.5 and 4.6 show the main diffraction peaks related to CuO and ZnO.

Table 4.5: Main diffraction peaks related to CuO

JCPDS	Plane	Diffraction angle (2θ)	Intensity
45-0937	[110]	32.497	8
	[111]	35.496	100
	[111]	38.731	91
	[202]	48.727	20
	[202]	58.377	9
	[113]	61.535	15
	[311]	66.250	11
	[220]	68.091	11

Table 4.6: Main diffraction peaks related to ZnO

JCPDS	Plane	Diffraction angle (2θ)	Intensity
36-1451	[100]	31.770	57
	[002]	34.422	44
	[101]	36.253	100
	[110]	56.603	32

The diffraction patterns of precursor and calcined samples of M1 and M2 are depicted in Figures 4.1 to 4.2 plotted simultaneously with pristine silica, the catalyst support used in the preparation. The pristine silica support exhibited a big hump at 15-30° which is typical characteristic of highly amorphous silica. This prevailing feature of silica giving rise to the broad feature is the first maximum of the Si-O pair correlation function. It remains unchanged in the diffractogram of precursors and calcined samples. The fact that no changes can be observed for this signal between precursor and calcined catalysts show that the average tetrahedral coordination in the support remained unchanged and that no crystallization process has occurred. Such a process may have been induced by the incorporation of cations from the active component mixtures as the temperature treatment alone would not have induced crystallization.

Generally, both precursor samples do not show discernible diffraction pattern of crystalline phases. This X-ray amorphous characteristic shows an early indication of the presence of nano-structured supported particles which can be observed in SEM images discussed later in this chapter. XRD investigation from earlier studies revealed that the successful catalyst should exhibit an X-ray amorphous structure [Maamor 2005]. Table 4.7 shows the analysis of samples M1 and M2 and their corresponding peak reflections together with the relevant JCPDS citation. The diffraction peaks are influenced by the degree of crystalinity, particle size and also the amount of active element corresponding to CuO in agreement with other characterization results from UV-Vis and SEM-EDX measurements.

Table 4.7: Structural characterization by XRD technique of precursor and calcined samples of M1, M2 and silica Aerosil 300.

Sample		Main Peak	JCPDS	Observation
Precursor	M1	22.0°	39-1425	Cristobalite, SiO_2 (syn). Amorphous material; shows reflection of silica.
	M2	22.0°	39-1425	Cristobalite, SiO_2 (syn). Amorphous material; shows reflection of silica.
Calcined	M1	22.0°	39-1425	Cristobalite, SiO_2 (syn). Amorphous material; shows reflection of silica.
		35.5°, 38.9°	45-0937	CuO tenorite (syn). Crystalline material in mixture with amorphous silica. Characteristic pattern assigned to tenorite (syn), monoclinic lattice.
	M2	22.0°	39-1425	Cristobalite, SiO_2 (syn). Amorphous material; shows reflection of silica.
		35.5°, 38.9°	45-0937	CuO tenorite (syn). Crystalline material in mixture with amorphous silica. Characteristic pattern assigned to tenorite (syn), monoclinic lattice.
Support	Silica Aerosil 300	22.0°	39-1425	Cristobalite, SiO_2 (syn). Amorphous material; shows reflection of silica.

The identification of poorly crystalline phase in both calcined samples as depicted in Figure 4.1- 4.2 are shown by the presence of twin peaks at 2-theta 35.5° and 38.9° which are typical characteristic pattern assigned to tenorite CuO with monoclinic structure (JCPDS 45-0937). The finding suggests that the large copper oxide particles are situated at the external surface of the support material. The most probable explanation for this unwanted crystallisation is that after incipient wetness impregnation a large amount of the copper ions has been entrained out of the mesopores with the solvent flow during the drying treatment. As a result, the large copper citrate crystallites have precipitated at the external surface during drying, thus giving rise to the formation of the copper oxide crystallites of this catalyst during the calcination process. However, a significant quantity of copper ions has been retained inside the mesopores after drying, giving rise to the formation of small copper oxide particles inside the mesoporous support structure. Therefore, due to the limited interaction between copper ions and the support pore walls during the catalyst preparation process a catalyst with a broad particle size distribution is obtained, consequently exhibiting a relatively low dispersion of copper (oxide) [Rammohan 2004].

There is no diffraction line for ZnO and NiO phase in the diffractogram of samples M1 and M2 respectively. These results can be related to lower zinc and nickel loading (6.25%). This finding also suggests that the abundant zinc and nickel species are present as non-crystalline binary oxide, or is incorporated into the silica by acting as textural modifier forming a “zincsilicate” or “nickelsilicate” structure respectively [Poels and Brands. 2000]. This may help in producing a better dispersion of the nanostructured copper as the active component in the catalysts [Kim *et. al.* 2003]. The diffraction peaks are influenced by the degree of crystallinity, particle size and also the amount of active element corresponding to CuO in agreement with other characterization results from BET, UV-Vis and SEM-EDX measurements.

Moreover, that the active working component in the material should be very small nanostructured copper particle as indicated by their largely X-ray amorphous characteristic. The addition of only small amount of zinc and nickel acted as textural promoter modifying the support of the system to produce a better dispersion of the copper particle. As expected no indication for a ternary mixed oxide of a Cu-Zn or Cu-Ni were found by XRD indicating that after reduction the localisation of Cu and Zn or Ni will be different from each other. It is believed that applying spray dried technique for slurry solidification causes the formation of homogenous size of Cu particles being well dispersed on support and this brings to the formation of homogeneous CuO particles compared to the standard drying method [Nasrudin 2008]. High temperature during calcination provides sufficient energy and weakens the anchoring of copper solution precursor onto the support and thus causing the particles to sinter and form large particles. However, samples (after calcination) can be considered as X-ray amorphous as the material could be nanoscopic basic structural units which would not give rise to significant Bragg diffraction.

In summary, the XRD investigation reveals the samples are composed of an x-ray amorphous structure. The second metals (zinc and nickel) show no sign of an individual phase formation but is assumed to be dissolved in the nanostuctured primary particles of the support silica helping to disperse the copper material throughout the support and prevent the sintering phenomenon of the active component

[Kim *et. al.* 2003]. As a conclusion, the occurrence of slight development of poorly crystalline CuO-like material diffraction in M1 and M2 after calcinations are taken as indication of the presence of many CuO nanoagglomeration dispersed on the coarse support of silica. This corresponds to the high metal loading (25 wt%) and high calcination temperature (723 K) used in the preparation.

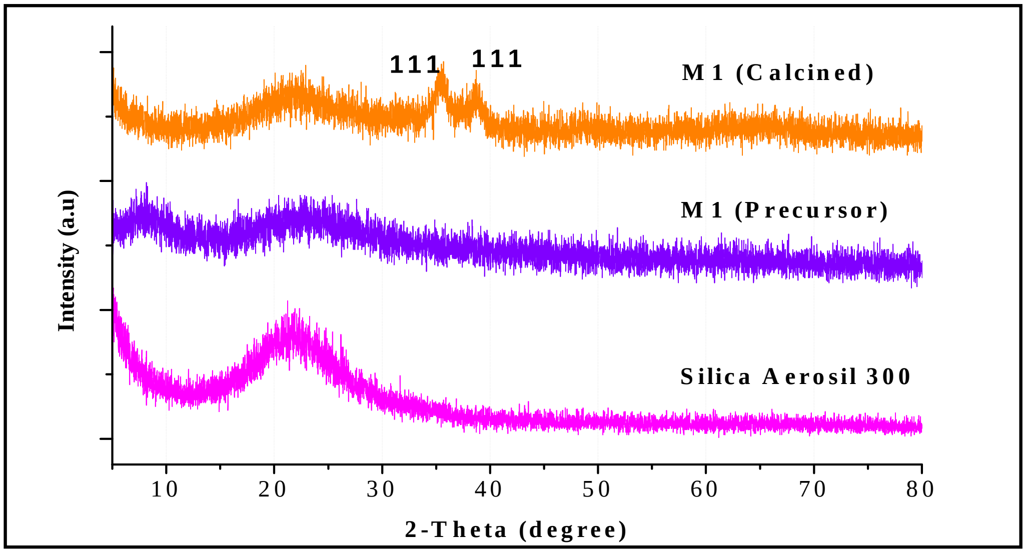

Figure 4.1: X-ray diffraction patterns of M1 in comparison with silica Aerosil 300

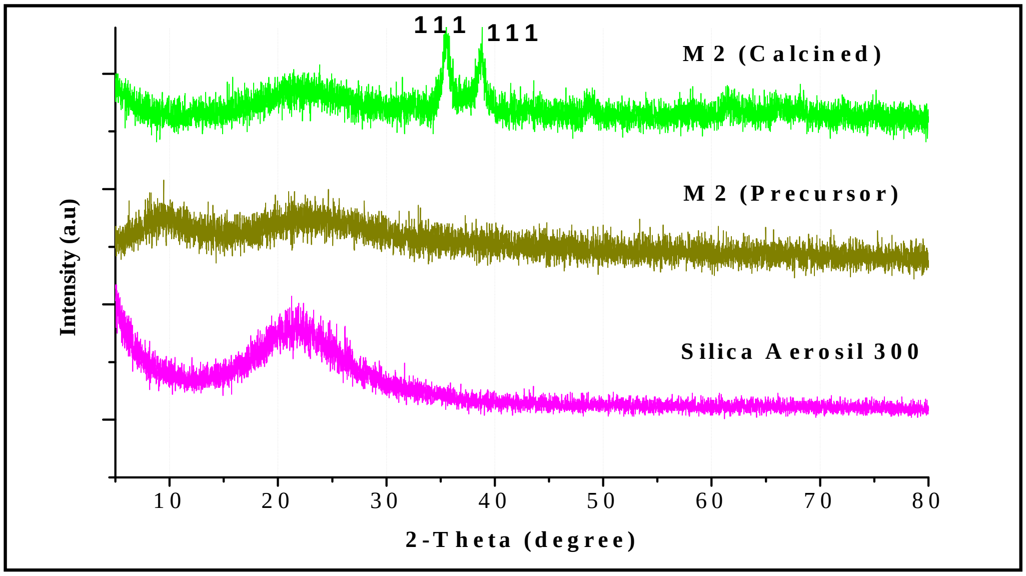

Figure 4.2: X-ray diffraction patterns of M2 in comparison with silica Aerosil 300

4.2.3 Nitrogen Physisorption Measurement

Nitrogen physisorption technique is used to define the textural properties of precursors and catalysts. Attention is made to follow the variation in surface area and porosity of samples as a consequence of differences of second metal used. The rate of the product formation is a function of the available surface area of the active phase and so it follows that the greater the amount of active surface area (ASA) accessible to the reactant, the higher is the reaction throughput. In supported systems it is often customary to assume that a fixed relaxation exists between the total surface areas (TSA) and the ASA. It is thus of primary concern to ensure that TSA is not lost during catalyst preparation. A desirable morphology is monolayer coverage of the active phase on the support that will affect the initial morphology in a minimal way. Thus, the mode of catalyst preparation and its subsequent activation influence greatly the resulted surface area of the catalyst prepared. Therefore, it is useful to measure the surface area for each sample to evaluate and to develop the methodology used in the modification.

The experimental isotherms were analysed in terms of Brunauer, Emmett and Teller (BET) surface area and for the pore volume and its size distribution using the Barrett, Joyner and Halenda (BJH) method. It is imperative to know the pore structure in a given catalyst as some of the internal microporous surface area is completely or partially inaccessible to large reactant molecules and thus may restrict the rate of conversion to products by impeding the diffusion of reactants and product through the porous medium. All samples were analyzed in their precursor and calcined states. The results from the samples are summarized in Table 4.8 and the isotherms are depicted in Figures 4.3-4.7.

Table 4.8: Characteristics of the porous structure of the samples before and after calcinations.

Sample	**Precursor**		**Calcined**		**Average pore diameter**	**Particle size**	**Colour**	
	BET, SA (m^2g^{-1})	**BJH, $V_p{}^a$ (cm^3g^{-1})**	**BET, SA (m^2g^{-1})**	**BJH, $V_p{}^a$ (cm^3g^{-1})**	**(nm)**	**(nm)**	**Dry**	**Calcined**
Silica Aerosil 300	N.A	N.A	299.14	1.26	N.A	N.A	White	White
M1	22.83	0.40	103.43	0.77	30	10.35	Light blue	Dark Brown
M2	26.36	0.34	191.84	1.15	34	4.69	Light blue	Black

The pristine commercial silica support used is generally assumed to be non-porous nano-particles. The material is a typical non-porous platelet piles with rough outer perimeters as the inter-particle volume is so large. Nitrogen physisorption results support that it is a non-porous type. Eventhough the isotherm (Figure 4.3) shows a small loop at region III and with relatively small pores size distribution mainly in the range of 10 – 20 Å, these can be considered as artifacts and are thus ignored. It is demonstrated that the characteristic of pristine silica support used is most likely the type III isotherm of non-porous system based on IUPAC nomenclature. For silica support there are two distinct regions seen in Figure 4.3. At relative pressure (P/P_0) of up to 0.85, a moderate amount of nitrogen becomes physisorbed (region I, II and III).

At relative pressure of 0.98 the nitrogen uptake by the sample increases further which could be assigned to inter-particle filling of voidages as expected for fluffy nano-particles (region IV) [Chen *et al.*, 2004].

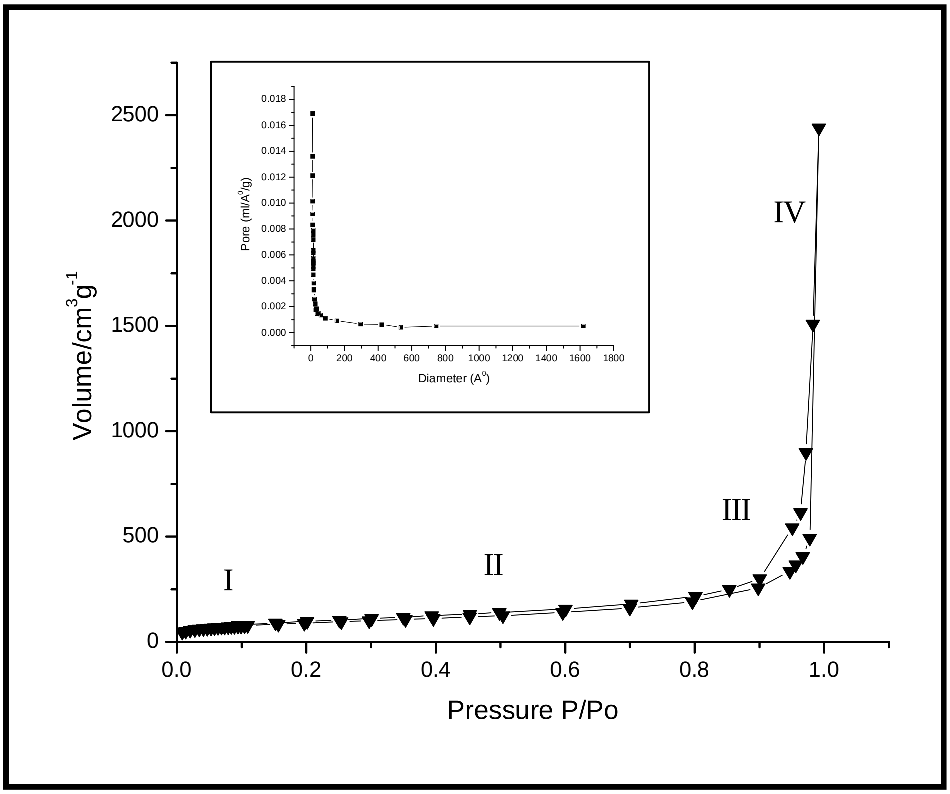

Figure 4.3: Nitrogen adsorption-desorption isotherm of silica support. Also (inset) the pore distribution of silica

It is the purpose of the investigation to detect any textural changes of the parent support silica with both samples. These may originate from the chemical transformation of the basic structural units (incorporation of metal ions into the oxide matrix). In addition, the agglomeration of the basic structural units (BSU) may change through precipitation of active metal oxide particles and or through modification of the support oxide surfaces occurring from their contact with the impregnated liquid and also the thermal treatment during drying and calcination.

Generally, it is observed that the general shape of silica isotherm was quite preserved for both the precursor and calcined materials. The isotherm patterns for both samples, M1 and M2, show similar hysteresis loop in region III as in bare support (Figures 4.4 and 4.5). This indicates the filling and emptying of the pores by capillary condensation. However, the hysterisis loop was further extended until saturation/inter-particle condensation point when the desorption occurred suggesting changes in the pore structures have taken place from inkbottle shape to cylindrical or tubular pore type with a narrow distribution of uniform pores based on the characteristic of the hysterisis loops [Thomas *et al.*, 1997]. Presumably after precursor loading, large amounts of copper ions were driven out of the pores with the solvent flow during drying treatment [Chen *et. al.,* 2004]. The complexes seemed to have formed a continuous layer of material encapsulating much of the support aggregates with the loss of surface area. All specific surface areas measured for both samples are still lower than 299.14 m^2g^{-1}, suggesting that the specific surface area loss had occurred after slurry drying and calcination processes. It is mainly because of the effect from the addition of metal precursor on the support that would originate a chemical transformation of their basic structural units.

This apparent correlation is a strong indication that the support cannot be considered as inert against the deposition-drying calcination process. Traditionally it is assumed that the pore system created by the irregular stacking of the silica BSU forms an inert system of channels for the transport of fluids and during drying/calcination of gaseous species that is either modified by the deposition of nanoparticles or narrowed by deposition of a continuous film of a oxide layer. The present data indicating substantial losses in the volume of this macroscopic pore/channel system strongly suggest that after drying a strong modification of the architecture of the pore system had occurred as the surface of the silica BSU was modified by the deposition solution.

Most of the voidage between the particles of the silica are lost after the deposition process and this voidage is indicated as the location of the deposition of the salts. Furthermore the size distributions of the interparticle voidage are reduced as can be seen from Figures 4.6 and 4.7. It can be concluded that some of the silica is dissolved into its primary basic structural units and re-assembled themselves into different secondary structures. In this process there is a good opportunity to mix the Zn-Ni into the support structure whereas the Cu tends to self-agglomerate. This is due to the different surface charges of Cu and Zn-Ni at the pH when drying begun: Zn-Ni reacted with the OH groups of silica whereas Cu self-condensed into hydrous oxides.

The reduction in surface area and pore volume happen when the Cu particles precipitate at or next to the external and internal surfaces and the precursor complex seems to have formed a thin film that contains metal ions after drying. Thus it may originate the formation of small copper oxide during calcination [Rosenthal M.R., 1973]. A decrease in the specific surface area of silica is observed after impregnation either with ZnO or NiO, this decrease is more pronounced in the case of ZnO catalyst. This event indicates that probably precipitation has occurred during metal loading as metal citrate precursor covered the pores and the surface area of silica support. Presumably after precursor loading, large amounts of metal ions were driven out of the pores with the solvent flow during drying [Rosenthal 1973]. In addition, a significant increase in the pore volume (V_p^a) after calcinations is observed for both catalysts (Figures 4.6 and 4.7). This increase (V_p^a) may be interpreted as arising from the penetration of zinc oxides and nickel oxide particles in the silica pores, thereby causing some expansion to slightly wider pore size [Witte et. al., 2008].

An important aspect of the catalyst is the pore structure. The advantageous of pore structure of the catalyst of the present invention is characterised by wide pores in combination with a good porosity. The average pore diameter of the catalyst is at least 10 nm, preferably between 10 and 60 nm. This average pore diameter is calculated from the pore volume by the formula **PV*4000/SA**, in which PV is the pore volume as defined underneath, and SA is the single point BET surface area. For example for silica containing materials, this is quite contrary to the usual pore size of 4 nm. At higher amounts of structural promoter, these typical values are found again. In this respect it is to be noted that the macropore size does not play a role in this, which is also confirmed by the use of nitrogen physisorption for defining the average pore diameter. This method only determines pore diameters up to about 60 nm. On the basis of structural analysis of the catalyst it has been determined that the best definition of the shape of the pores is a cylindrical shape. Accordingly the model for determining the average pore diameter was based on this shape [Reesink et. al, 2003]. The particle size (crystalline size) d_{BET} was figured out according to the following equation $\mathbf{6*10^3\ /SA*\rho}$, where d_{BET} is the crystalline size (nm), ρ is the density of nanosized powder (g/cm^3), and SA is the BET specific surface area (m^2/g).

In summary, the adsorption isotherms retain type IV hysteresis, characteristic for mesoporous materials. M1 as well as M2 show a typical isotherm for materials with ordered mesoporous channels. Nevertheless, the hysteresis of M2 is shifted to higher relative pressure compared to the M1, indicating that larger pores are obtained. Also the pore volume is higher than the pore volume of M1. The hysteresis loop appears at high relative pressures and at this point, the isotherms show a large increase in the amount of adsorbed nitrogen. On the other hand, these materials have smaller specific surface areas than silica. M2, in comparison to M1, has a broader pore size distribution, a higher specific surface area and total pore volume and smaller pore dimensions. A loss in pore volume and surface area is obtained for both materials after deposition of the bimetals (Cu-Zn and Cu-Ni). This is due to:

1) The bimetallic (Cu-Zn / Cu-Ni) particles deposited in the mesopores of the silica materials will block the micropores. This results in a significant decrease in microporous-specific surface area and pore volume.
2) The bimetallic (Cu-Zn / Cu-Ni) nanoparticles occupy a part of the mesopores resulting in a decreased pore volume.
3) Keeping in mind the higher molecular weight of bimetals (Cu-Zn / Cu-Ni) in comparison to silica, one can conclude that the specific surface area and the total pore volume (both expressed per gram) will be seriously decreased [Witte et. al, 2008].

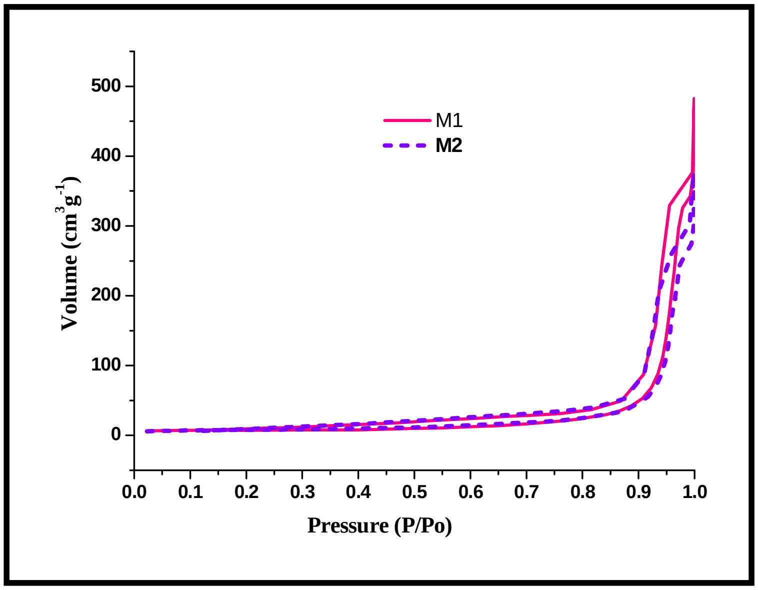

Figure 4.4: Nitrogen adsorption-desorption isotherms for precursor samples M1 and M2.

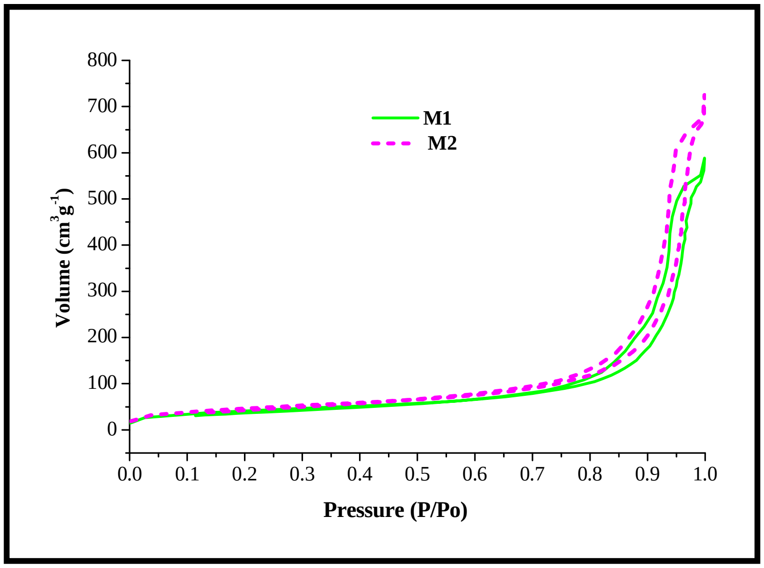

Figure 4.5: Nitrogen adsorption-desorption isotherms for calcined samples M1 and M2.

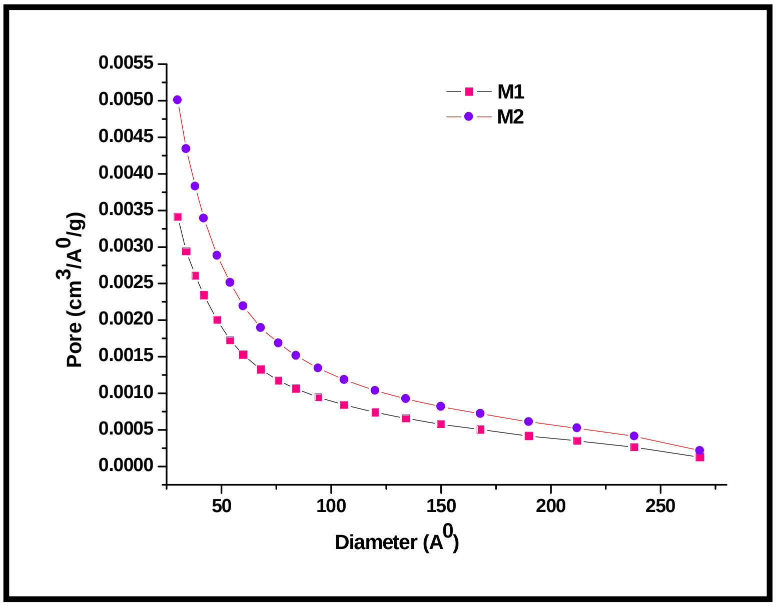

Figure 4.6: Pore size distribution for precursor samples of M1 and M2

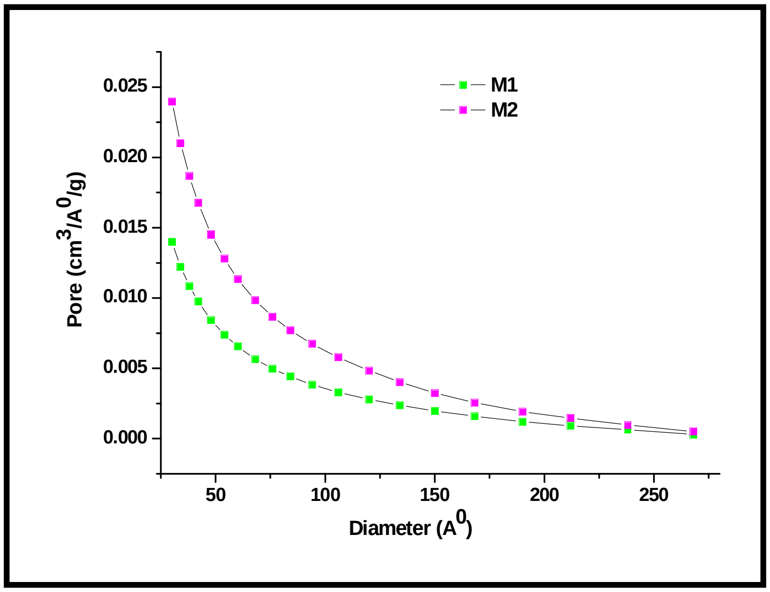

Figure 4.7: Pore size distribution for calcined samples of M1 and M2

4.2.4 Scanning Electron Microscope and X-ray Dispersive Analysis (SEM-EDX)

It is known that the morphology of the copper oxide particles is the most relevant factor for preparing a successful catalyst where the aggregation helps expose the activated surface. Therefore, the SEM technique is used to study the texture and morphology of the samples, M1 and M2. Environmental SEM with field emission gun is used to obtain medium-high resolved images of uncoated samples. In general low and medium magnifications were used to recognise the disposition of typical objects to be inspected with the highest useful magnification for this kind of very poorly conducting material [Wang *et al.* 2003].

EDX allows further identifying of the surface chemical nature of mesoscopic objects. With electron microscopy alone it is also difficult to find the typical structure of a complex material. Together with the data presented so far, it is possible to augment analysis of the picture derived so far by SEM-EDX data without falling into the problem of selecting a typical situation. This technique is also useful to study the micro morphology in addition to the more integral examination by XRD and BET whereby, these data show how vastly different the local composition can be from average sample content and it also underlines the multiphasic nature of the samples. This was done by analyzing four spots on each material and the results are summarized in Table 4.9 and individual results for each sample are reported in Figures 4.13 and 4.14.

Table 4.9: Averages of EDX measurements on calcined samples, M1 and M2

Sample ID	Element	Metal/Support			
		Atomic %		Weight %	
		Calculated	Experimental (Average value)	Calculated	Experimental (Average value)
M1	**Cu**	3.00	3.78	15.50	15.04
	Zn	1.00	1.17	5.40	5.67
M2	**Cu**	3.00	3.31	16.10	16.31
	Ni	1.00	1.06	4.90	4.56

The systematic error of EDX method can be estimated to be 3%. A larger source of errors arises from the varying electronic structure of the sample giving rise to vastly different volumes of analysis at different locations in the same sample (interaction profile of the electron beam with the different locations structure). The compositional variation in the samples is so large that an average of four sampling points may not be sufficient for eliminating the fluctuations. Taking all these considerations into account it can be stated that in all samples the agreement between theoretical and experimental composition is good to fair. Large deviation indicates large textural fluctuations. For this reasons it was not found adequate to statistically analyze the data and quote the standard deviations as a measure of accuracy.

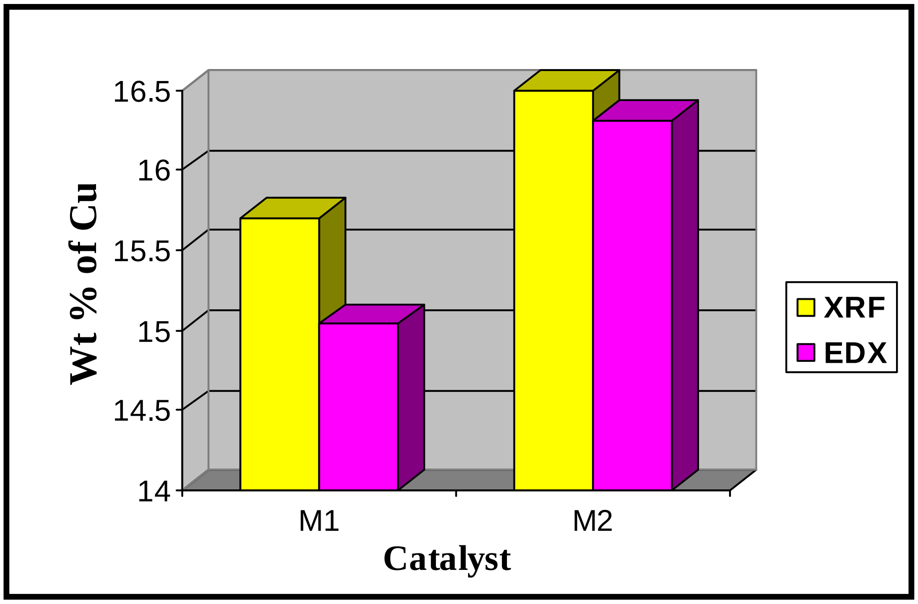

Figure 4.8: Comparison of wt% of Cu analyzed using EDX and XRF

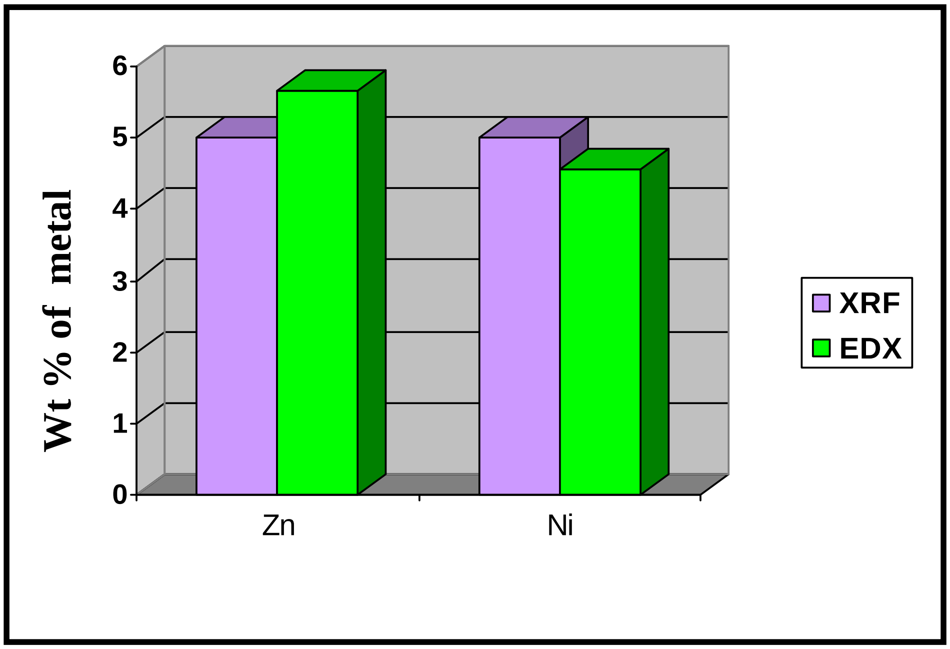

Figure 4.9: Comparison of wt% of Zn and Ni analyzed using EDX and XRF

Initially, the elemental weight percent has also been analyzed by XRF which in principle measures the average percentage of element in bulk whereas the EDX is a sub-surface elemental analysis whereby the electron beam penetrates to approximately 1-4 μm deepness from sample's surface depending on sample density. The results from both analyses are useful as complementary to each other and specifically for investigation of sample's homogeneity from surface to bulk. Figures 4.8 and 4.9 show 2 sets of comparison bar graphs of metal wt% of Cu in both samples and metal wt% of Zn and Ni in respective calcined catalysts analyzed using EDX and XRF. Generally for weight percent of Cu in both samples, there were systematic deviations between both analyses at approximately 2.8 % with XRF given higher values of percentage than EDX. In the case of Zn, the deviations of weight percent is higher in EDX while for Ni it is higher in XRF. Therefore, upon considering some errors mentioned earlier in both analyses, one can conclude that generally all metals are homogeneously scattered within samples as seen in good agreement between both analysis techniques with more systematic in case of CuNi compared to CuZn.

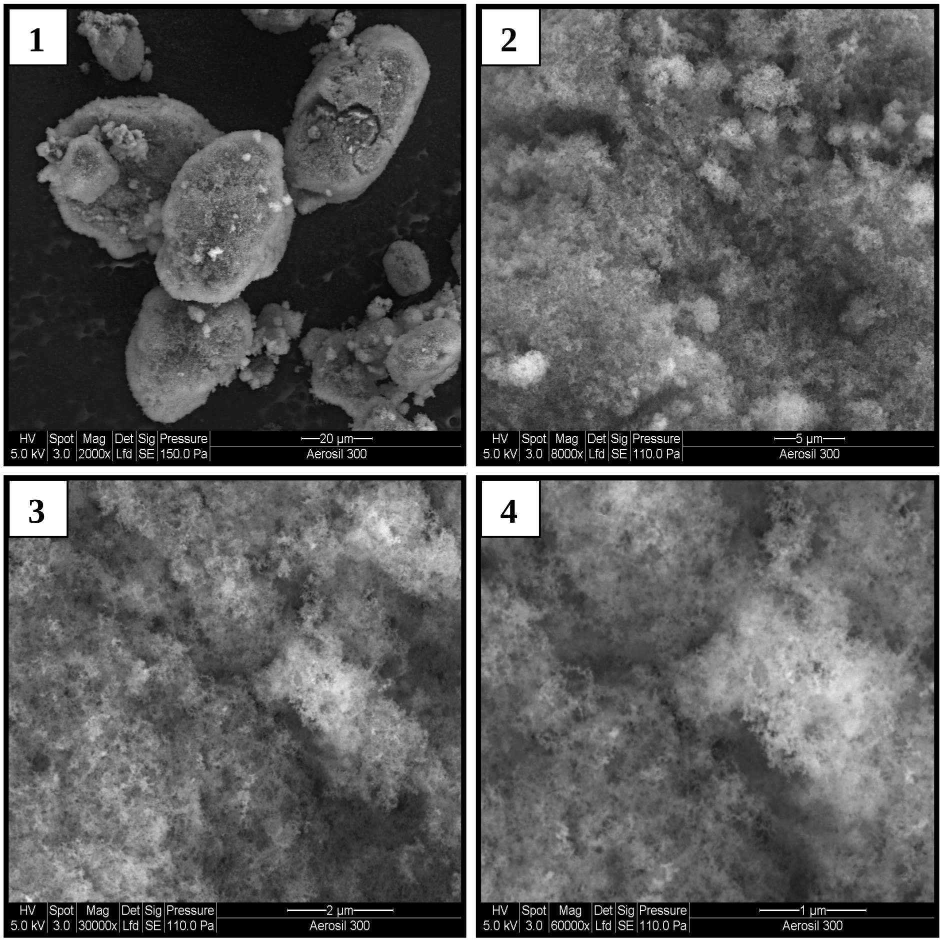

Figure 4.10*:* SEM image of bare silica support (Aerosil 300)

The micrographs of silica support are shown in Figure 4.10. Generally, the silica support exhibits as poorly structured materials. Furthermore, the morphology shows that it appears as non-spherical agglomerates of 100 nm and less forming a secondary structure of chains of rough particles. Mostly they enclose a huge empty volume (inter particle between very small nanoparticles) as seen in BET near P/P_0 approximately 0.85-0.95. Only sometimes the orientation of the basic structural unit (BSU) is such that the basal plane of the stacks is situated parallel to the electron beam giving rise to the contrast of a densely agglomerated material. This silica material is perfectly suited for supporting as it offers unrestricted access to all its surface of the BSU.

The characteristic SEM images along with the individual analysis results of EDX measurement for the M1 and M2 supported on silica catalysts are compiled in Figures 4.11 to 4.18. The summarised results of EDX analysis are given in Table 4.9. This helps in further explanations on characteristic of both catalysts (M1 and M2). EDX allows further identification of the chemical nature of samples. The integral chemical composition were measured based on average number of local EDX analyses. This was done by analyzing four spots in each material. In general, taking all the considerations into account it is found that in EDX analysis, all samples have shown an agreement between theoretical and experimental compositions to be good to fair. Due to small size of the BSU and hence of the chemically different structures with respect to an electron probe within a non-conducting and charging sample it was not possible to detect chemical compositions locally such as to assign chemical natures to textural features. This would have to be done in a Transmission Electron Microscope coupled with EDX study (TEM-EDX) but this is not studied in this dissertation.

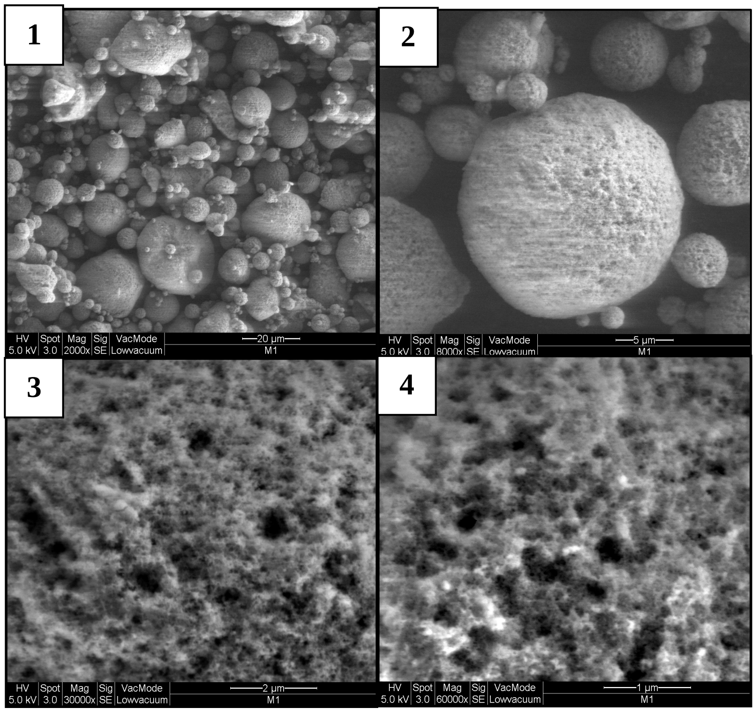

Figure 4.11: SEM images of precursor M1

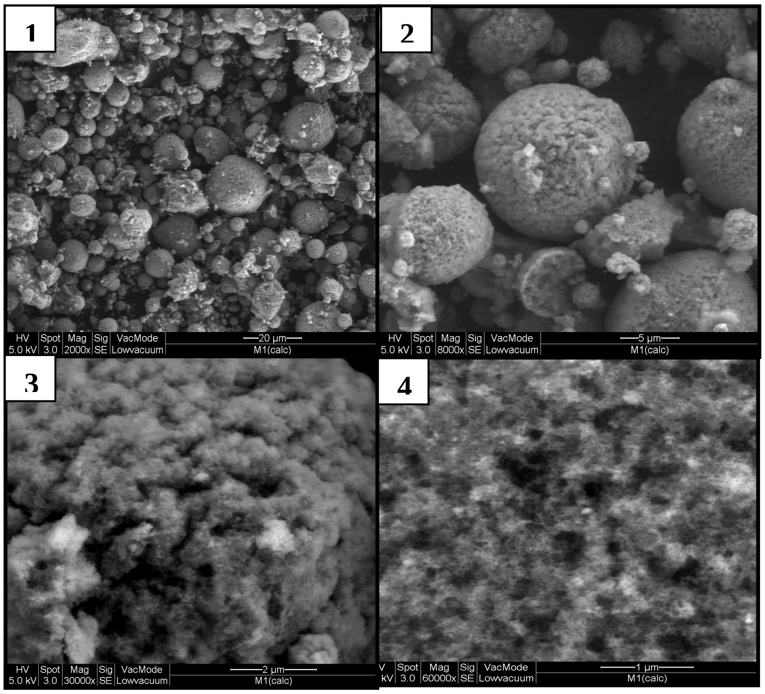

Figure 4.12: SEM images of calcined M1

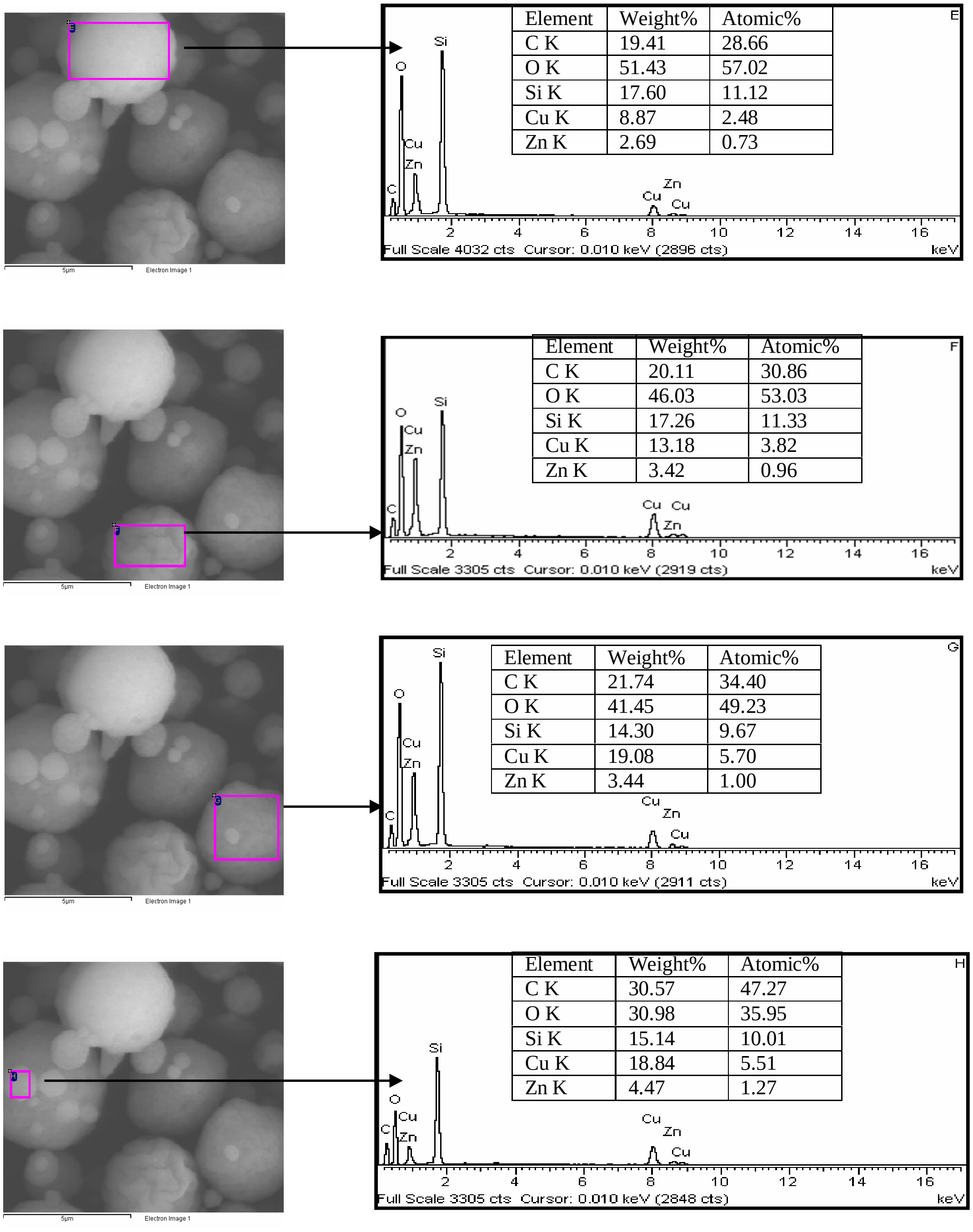

Element	Weight%	Atomic%
C K	19.41	28.66
O K	51.43	57.02
Si K	17.60	11.12
Cu K	8.87	2.48
Zn K	2.69	0.73

Element	Weight%	Atomic%
C K	20.11	30.86
O K	46.03	53.03
Si K	17.26	11.33
Cu K	13.18	3.82
Zn K	3.42	0.96

Element	Weight%	Atomic%
C K	21.74	34.40
O K	41.45	49.23
Si K	14.30	9.67
Cu K	19.08	5.70
Zn K	3.44	1.00

Element	Weight%	Atomic%
C K	30.57	47.27
O K	30.98	35.95
Si K	15.14	10.01
Cu K	18.84	5.51
Zn K	4.47	1.27

Figure 4.13: EDX images of precursor M1

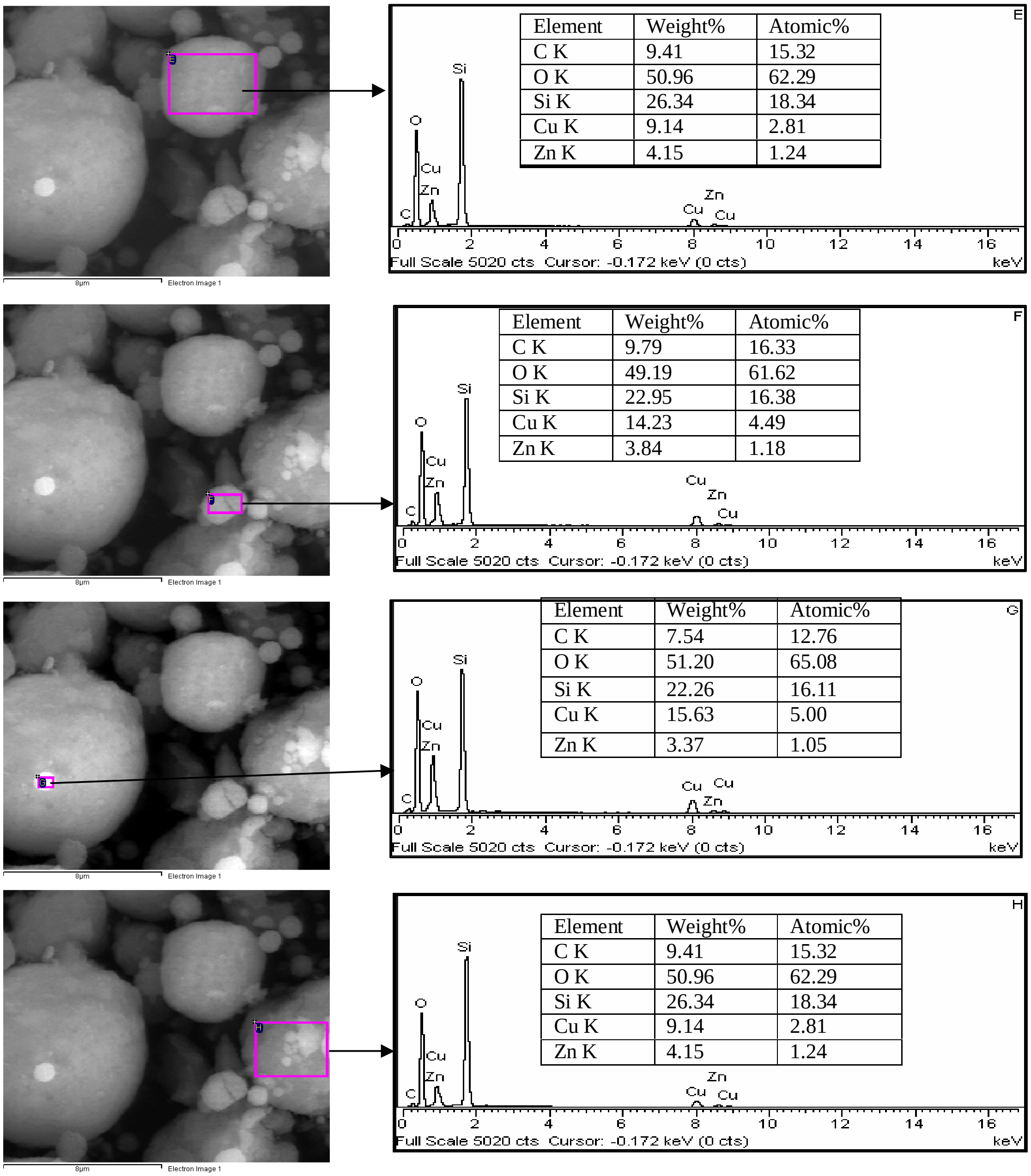

Element	Weight%	Atomic%
C K	9.41	15.32
O K	50.96	62.29
Si K	26.34	18.34
Cu K	9.14	2.81
Zn K	4.15	1.24

Element	Weight%	Atomic%
C K	9.79	16.33
O K	49.19	61.62
Si K	22.95	16.38
Cu K	14.23	4.49
Zn K	3.84	1.18

Element	Weight%	Atomic%
C K	7.54	12.76
O K	51.20	65.08
Si K	22.26	16.11
Cu K	15.63	5.00
Zn K	3.37	1.05

Element	Weight%	Atomic%
C K	9.41	15.32
O K	50.96	62.29
Si K	26.34	18.34
Cu K	9.14	2.81
Zn K	4.15	1.24

Figure 4.14: EDX images of M1 after calcined

The difference of SEM images between precursor and calcined samples for both samples can be seen in Figure 4.11-4.14 for M1 and Figure 4.15-4.18 for M2. For both samples, after calcinations the size of particle becomes smaller. The morphology clearly shows the formation of spherically ball shaped particles with uneven surface that contains several type of dents caused by the drying process. The dispersed copper on modified support are also observed. Figures 4.12 and 4.16 show that the chemical nature of the agglomeration has also changed (no more Si-OH groups as all are used up for binding with the active phase and or were lost (structural promotion concept). During spray drying, there was an instantaneous evaporation which is similar to an explosion. As a result, the structure is disrupted and there were no covalent bondings. Therefore, the spray drying may be an unsuitable method as it allows agglomeration of the more active materials on their outer surface. As beautiful as these samples may look they are no good as the large spherical lumps concentrate much of the active material that maybe missing in the monolayer coverage and destroy the fluffiness. As mentioned earlier, it is very important to preserve the fluffy nature of support characteristic in order to arrive at depositing a thin layer of active material on most of the surface where it excludes some outer surface where aggregation took place. This is a major success of the complexing actions. Overall, the EDX measurement found that the chemical composition of the samples is locally varied and not homogenous because the element distribution with respect to atomic percent is not persistent for each plate as shown in Figures 4.13, 4.14, 4.17 and 4.18. Some big clusters show high atomic percent of copper and low atomic percent of zinc or nickel.

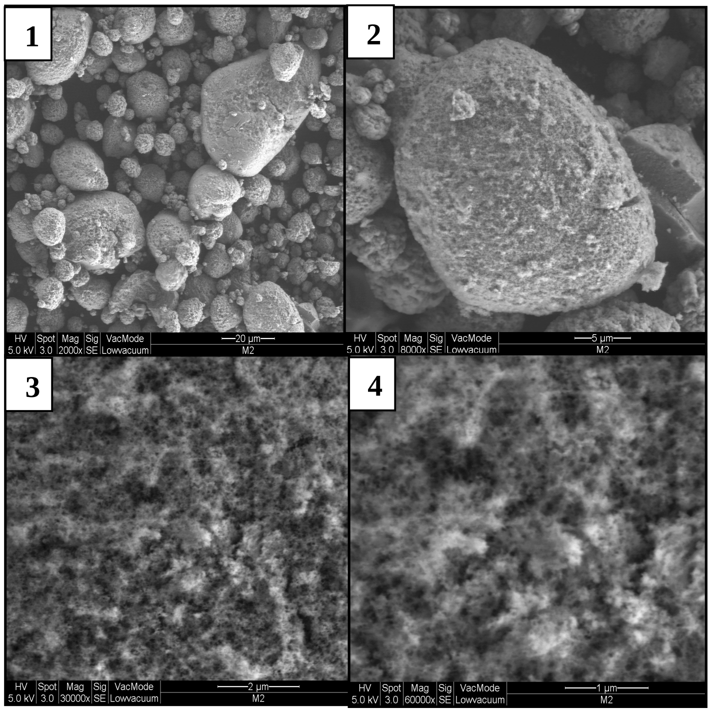

Figure 4.15: SEM images of precursor M2

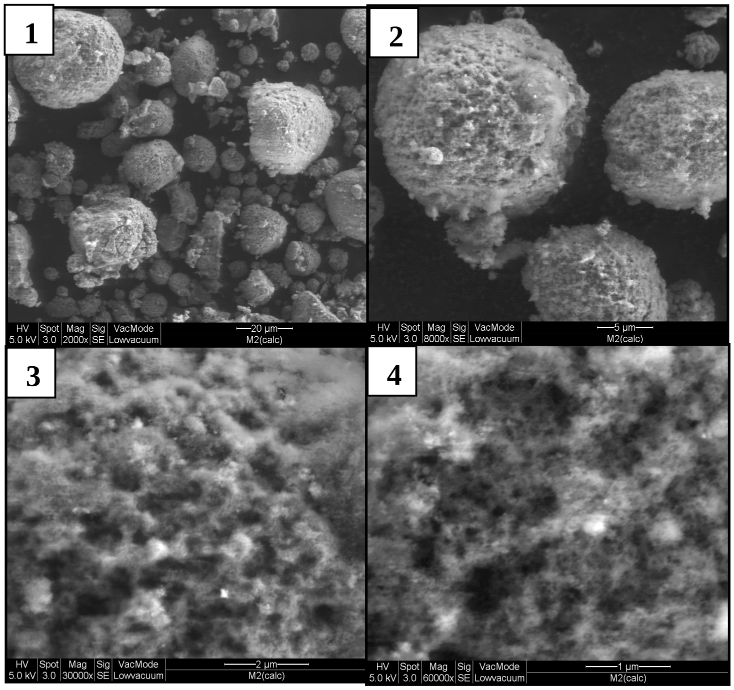

Figure 4.16: SEM images of calcined M2

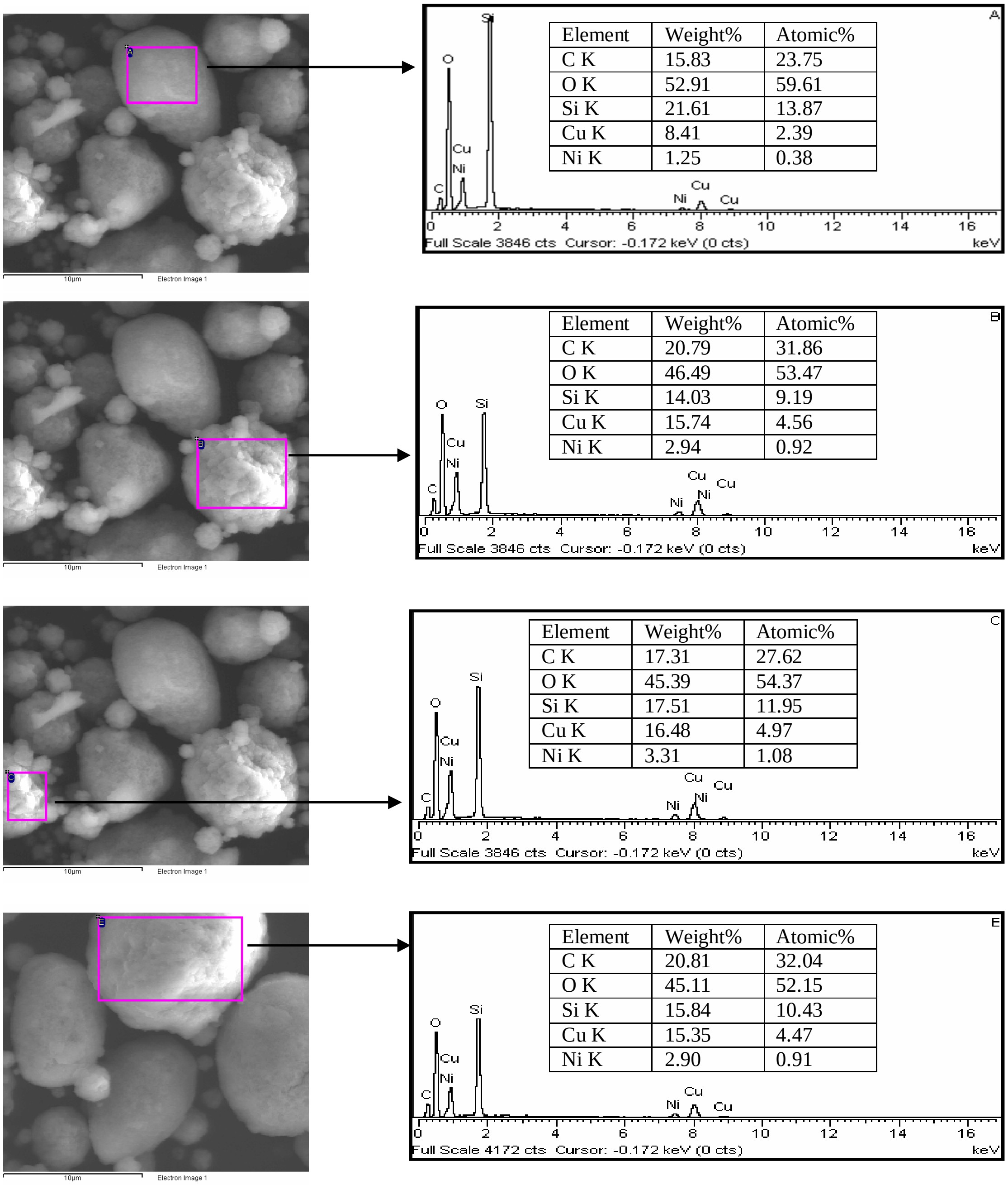

Element	Weight%	Atomic%
C K	15.83	23.75
O K	52.91	59.61
Si K	21.61	13.87
Cu K	8.41	2.39
Ni K	1.25	0.38

Element	Weight%	Atomic%
C K	20.79	31.86
O K	46.49	53.47
Si K	14.03	9.19
Cu K	15.74	4.56
Ni K	2.94	0.92

Element	Weight%	Atomic%
C K	17.31	27.62
O K	45.39	54.37
Si K	17.51	11.95
Cu K	16.48	4.97
Ni K	3.31	1.08

Element	Weight%	Atomic%
C K	20.81	32.04
O K	45.11	52.15
Si K	15.84	10.43
Cu K	15.35	4.47
Ni K	2.90	0.91

Figure 4.17: EDX images of precursor M2

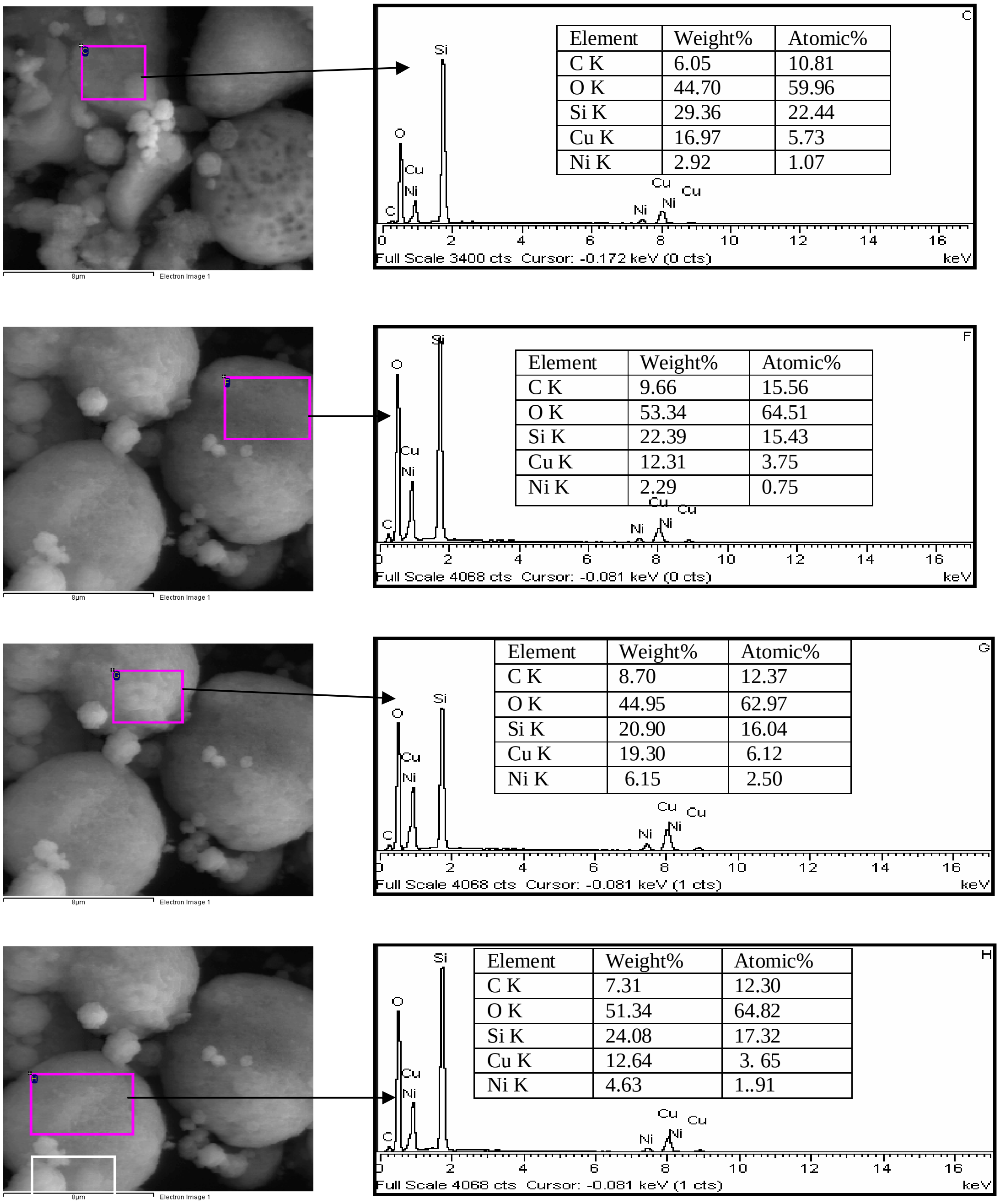

Element	Weight%	Atomic%
C K	6.05	10.81
O K	44.70	59.96
Si K	29.36	22.44
Cu K	16.97	5.73
Ni K	2.92	1.07

Element	Weight%	Atomic%
C K	9.66	15.56
O K	53.34	64.51
Si K	22.39	15.43
Cu K	12.31	3.75
Ni K	2.29	0.75

Element	Weight%	Atomic%
C K	8.70	12.37
O K	44.95	62.97
Si K	20.90	16.04
Cu K	19.30	6.12
Ni K	6.15	2.50

Element	Weight%	Atomic%
C K	7.31	12.30
O K	51.34	64.82
Si K	24.08	17.32
Cu K	12.64	3. 65
Ni K	4.63	1..91

Figure 4.18: EDX images of M2 after calcined

The comparison of the morphological analysis of the catalytically more successful citrate family has given the clear trend that the preservation of the substrate morphology goes in parallel with the catalytic performance. The stronger the deviation of texture and morphologies are with respect to the silica supports, the less attractive is the catalytic function. It can be deduced that a successful catalyst synthesis must be carried out such as to prevent any modification of the support oxide chemistry. The modification in morphology and texture is detrimental due to losses of favourable transport properties (less surface area, blocking of mesopore transport paths) and it indicates that the active metal may not be fully available for catalysts as it is buried in the support oxide. Morphological inspection seems to be a good indicator for the expected performance: only unspectacular samples are good candidates and the presence of the impregnated material should manifest itself in any way at the level of resolution accessible with these materials.

In summary, all samples exhibited very small particles of aggregates between silica and active phases at their surfaces. Most of these aggregates are no crystals as no signs of such particles were detected in the XRD. But they are useful to indicate that in particular, after calcinations some of the active material has dissolved in the silica and changed the basic structural units (BSU). This was assigned as action of zinc oxide forming a solid solution of zinc silicate was not detectable as a phase in XRD. Here, TEM would be needed for further clarification. In addition it was found that the fluffy structure of the support must be preserved to enable a maximum distribution of the active phase as a layer and not as agglomerates of nanoparticles. These tend to form when the fluffy interparticle interaction is destroyed in the preparation process by either excessive deposition of active phase or by spray drying that breaks the secondary structure of the BSU aggregates (irregular stacks of platelet BSU forming rough nanoparticles that interact via OH groups to the secondary structure). Calcination changes the surface chemistry of the BSU and that is seen as a final indication for the structure-promoting effect of the zinc component. It cannot be said at this level of analysis that the interaction of the invisible particles of CuO is modified by this change in surface chemistry but it actually shows that the zinc incorporation in silica has affected the surface chemistry of the BSU.

4.2.5 UV-Visible Spectroscopy

Uv-Vis spectroscopy of diffuse reflectance (DR) was used to investigate the state of the cations in all precursors and calcined samples prepared by standard and modified preparation methods. In addition, this technique is used to provide information on the valence state and the average coordination number of transition metal cations.

Spectroscopy in the ultraviolet (UV) and visible (Vis) region of the electromagnetic spectrum is also often called electronic spectroscopy because electron are transferred from low-energy to high-energy atomic or molecular orbital when the material is irradiated with light [Weckhuysen 2004]. This technique also helps to explain the coloured-matter of elements as it is related to the electron transfer process in transition metal ion, an inorganic and organic molecule. Sample code and apparent colour description are listed in Table 4.10.

Table 4.10: The apparent colour of M1 and M2 samples.

Sample ID	Color	
	Precursor	Calcined
M1	Light Blue	Black
M2	Light Blue	Dark brown

The light blue colour observed in both precursor samples (Table 4.10) exhibited the typical characteristic of the presence of cupric ion Cu^{2+} in a dilute form allowing formation of undisturbed octahedral Cu-O ligand structures. Cu cations are dispersed onto the silica matrix in a dilute form rather than forming a (crystalline) Cu-silicate or copper oxide phase. After calcination, the colour of sample M1 changed to black while sample M2 changed to dark brown in colour. The black and dark brown coloured powders show the formation of CuO in the samples.

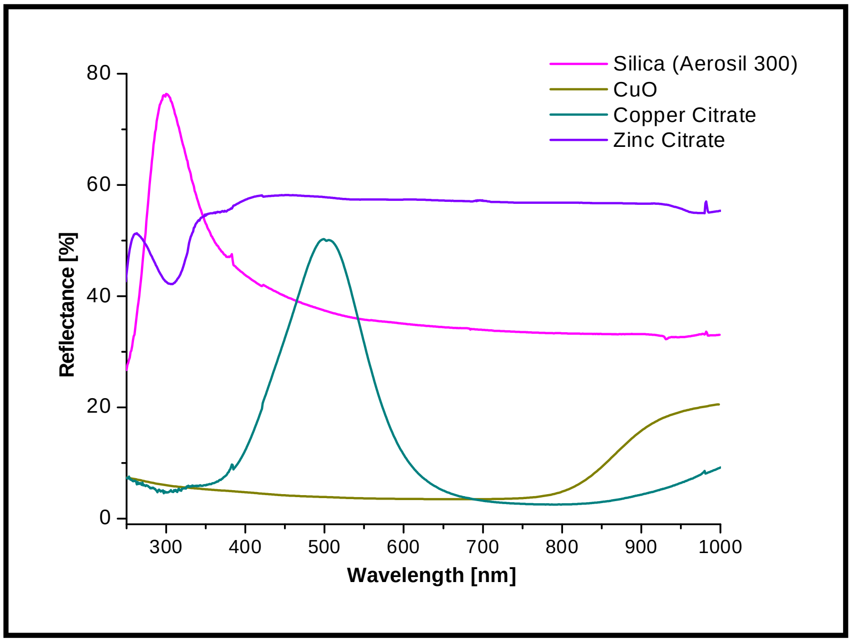

Figure 4.19: DR UV/Vis spectra of references

Bare silica support (Aerosil 300), copper oxide commercial chemical from Aldrich (99.0%), copper citrate commercial chemical salt from Pfaltz and Baeur (98.9%), zinc citrate commercial chemical salt from Aldrich (99.0%) were measured and represented in Figure 4.19 as guidance in the interpretation work of samples. Copper has the electronic structure [A]$3d^{10}4s^1$. It shows a broad band centred at 950 nm in the region of 850-1000 nm. A d^9 metal in an octahedral complex has the electronic configuration $t_{2g}^6e_g^3$; according to the Jahn-Teller thereom, such a complex should be distorted. The ground state of an octahedrally coordinated Cu(II) ion is ^2E_g $(t_{2g}^6e_g^3)$. The only excited state should then be $^2T_{2g}(t_{2g}^5e_g^4)$ with the energy difference being 10

Dq. The ^2D free ion term is split into ^2E_g and $^2T_{2g}$ by a field of O_h symmetry and further split on distortion to D_{4h} symmetry (Figure 4.20). The reflectance spectra of octahedral coordinated Cu(II) ions confirm the structural data [W.M Wesley *et al.*, 1966].

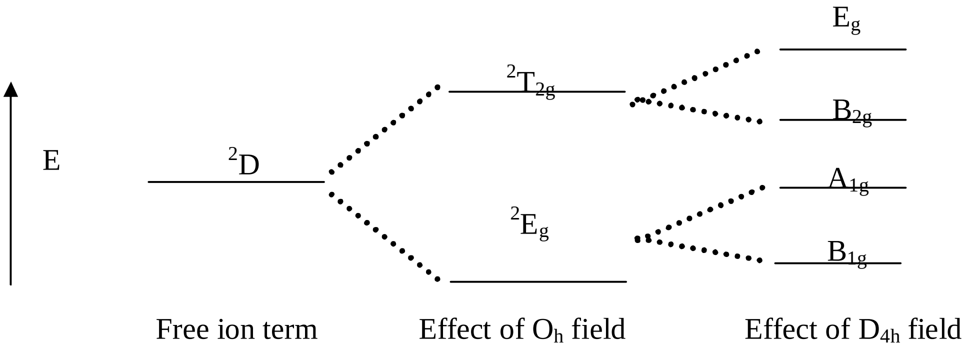

Figure 4.20: Splitting of octahedral ligand field terms on Jahn-Teller distortion for d^9 configuration.

Zinc has the electronic structure [A]$3d^{10}4s^2$. It shows a broad band in the region of 290-300 nm. The electronic ground state of Zn^{2+} ion is ^6S. In the weak field limit, assuming octahedral configuration, the ground state will be $t_{2g}^3e_g^2$, possessing five unpaired spins. In the strong field limit it will be t_{2g}^5 with only one unpaired spin. In a high spin octahedrally coordinated Zn^{2+} complex the lowest configuration $t_{2g}^3e_g^2$ gives rise to the ground state $^6A_{1g}$. One expects thus a sharp band for the LMCT of zinc positioned at 300 nm. As Zn(II) exhibits a filled d-shell, no d-d- transitions in fully oxidised compounds should be detected. This is consistent with the featureless spectra in Figure 4.20.

The spectral range can be divided into two parts; 1000 nm – 320 nm for visible range and below 320 nm for UV range. Care must be taken to observe the representation of the spectra in reflectivity units in which maxima indicate minimum absorption and minima stand for strong absorptions. Copper oxide spectra show an intense broad band centered at 950 nm in the region 850-1000 nm, (Figure 4.19) which is attributed to isolated octahedral coordinated cupric ion Cu^{2+}. Commercial zinc citrate shows broad band spectra in the region of 290-390 nm. Assuming the octahedral coordinated Zn^{2+} complex presence, one expects thus a sharp band for the LMCT of zinc positioned at 300 nm. As Zn(II) exhibits a filled d-shell, no d-d transitions in fully oxidized compound should be detected. For the silica support, one should be detects LMCT transitions in the UV range below 250 nm. In the Vis-NIR range the oxide exhibits featureless spectra with a limited reflectivity due to the optical qualities of the powder samples. Table 4.11 shows the UV-Vis band position and their assignment from the literature [Leofanti G. (2000)].

Table 4.11: UV-Vis band position and their assignments in accordance to literature [Leofanti G. (2000)]

Band position Wavelength [nm]	**Assignment**
690, 751, 773, 837	d-d transition of Cu(11) in octahedral environment
293, 303, 311	LMCT of isolated Cu(11)ions
300-340	LMCT of clustered Cu(11) ions
300	LMCT of Zinc

The reference data allow the following conclusion for the interpretation to be drawn. It is only copper species that will substantially contribute to the spectrum. The band position of the LMCT transition is highly sensitive to the nature of coordination and to the size of an oxide cluster. The d-d- transitions will be masked by the poor reflectivity of support oxides. For a Zn compound it may be expected to see a feature for the LMCT transition as this is sharp when the Zn is in a fully oxidized form. Any change in position from that of the parent compounds will indicate the incorporation of Zn into a ternary oxide. An exception will be the formation of Cu(II) oxide that is characterized by its band edge absorption of the collective electronic structure beginning at 920 nm and terminating at 800 nm.

Unfortunately, it is not possible to observe energy in the valence band at wavenumber less than 250 nm due the quality and sensitivity of the lab-scale UV detector used. Hence, only the onset or beginning of the LMCT region between 300-250 nm, can be used to verify the electronic states of the metal ions in the valence band. In the visible region, it is generally rather difficult to observe distinct d-d transition as the signals of metal ions tend to be weak. It is commonly seen as a broad peak. Only at low temperatures and diluted systems one can see distinct isolated peak. When the metal ions are coupled or have poor symmetry, there will be many split lines hence the d-d transition signals are broadened into a continuum. For wavenumber higher than 900, approaching NIR, the samples gets more transparent.

The close similarity in position and shape for both precursors of M1 and M2 shown in Figure 4.21 indicates that they contain the same type of supported copper species. All precursor samples exhibit a broad asymmetric band at 400-700 nm which is assigned to d-d transition of copper(II) cation and indicates the presence of copper(II) ion located in octahedral environment. In contrast with the precursor samples, the spectra of M1 and M2 calcined samples are dissimilar from one another (Figure 4.22). It was unfortunate that the poor reflectivity of the calcined samples excluded meaningful peak identification. This shows that calcined materials are hardly studied well in their undiluted state. The spectra of both calcined samples show that precursors have been completely eliminated at calcination temperature of 723 K, as there is no significant bands similar to the precursor appearing in the spectrum at the temperature concerned. The spectra of M1 and M2 samples show clear indication that CuO is formed in the sample after calcination as the spectra look similar to the reference CuO in Figure 4.19. It is suggested that UV-Vis can thus serve as fast and convenient method to establish the extent of condensation of the Cu species in future optimization efforts to try to eliminate the structural water at the mildest possible conditions. At the calcination temperature of 723 K, both samples show the bands of precursor eventually vanished. All bands are broad and diffuse (Figure 4.20) indicating a significant structural disorder of all compounds involved which is well in line with the XRD results.

In summary, UV-Vis is a suitable method to study x-ray amorphous samples for the local coordination of both precursors and calcined systems. The poor reflectivity in calcined samples allows one to presume that the dispersion of CuO over the surface of silica has been successful. However, the calcined materials cannot be studied very well in their undiluted state and this featureless data exclude the notion of supported copper oxide particles on an optically transparent support which would be the expected structural model. In those cases where a decent spectrum was obtained it can be concluded from the occurrence of detectable band edge absorption for the copper species that the CuO must be present in such large particles that a collective electronic system with little disruption as common in nano-clusters could be established.

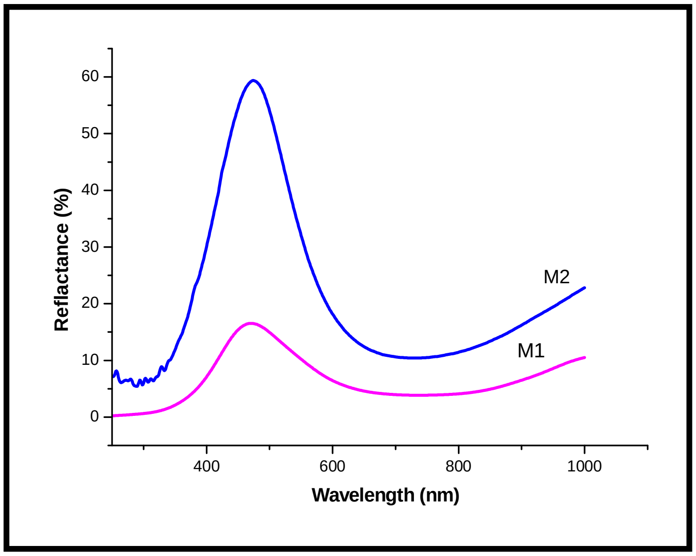

Figure 4.21: DR UV/ Vis spectra of precursor samples M1 and M2

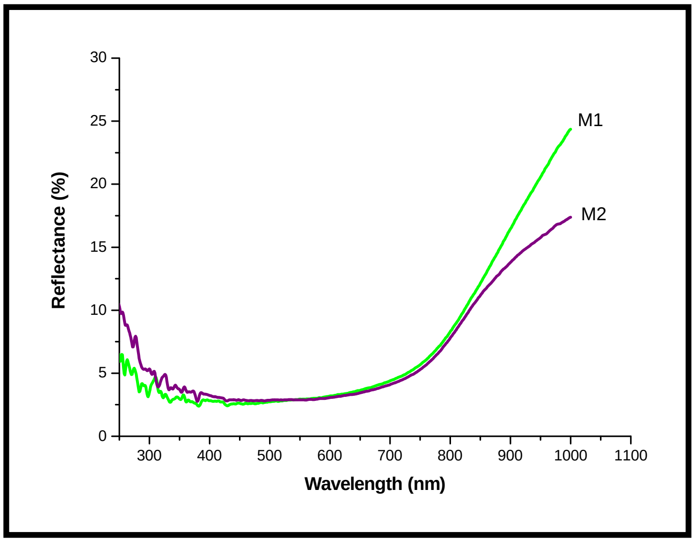

Figure 4.22: DR UV/ Vis spectra of calcined samples M1 and M2

4.2.6 Fourier Transforms – Infrared Spectroscopy (FT-IR)

The study of the vibration spectra by FTIR was carried out on both precursors and calcined samples M1 and M2. The FTIR spectroscopy was used to observe the chemical and structural changes that take place in each samples during the decomposition of the ligands in the heat treatment (before and after calcination). The frequency bands will be the fingerprint bands for each sample. The presence of ligands in precursor is in agreement with the UV-Vis spectroscopy suggesting some ligands in the sample have been removed after the calcination procedure at certain temperature. FTIR adsorption band position assignments of precursors and calcined samples M1 and M2 are shown in Table 4.12.

In general, the FTIR spectra of both precursors and calcined samples (Figure 4.23 – 4.24) show clear absorption bands of silica support at the region of ~1107 cm^{-1} and ~474 cm^{-1} which are assigned to different modes of Si-O-Si or O-Si-O vibrations [Boccuzzi *et. al.* 1992]. Bands at approximately 1107 cm^{-1} correspond to the stretching vibrations of Si-O bonds; a small shoulder at approximately 802 cm^{-1} is due to the presence of non-bonded oxygen Si-O-.The bands at ~474 cm^{-1} are attributed to bending vibrations of Si-O- and –O-Si-O- bonds. Both samples also show two additional broad band at 3444 cm^{-1} and 1624 cm^{-1} which can be assigned to the stretching vibrations of OH species and bending vibrations of OH from molecular H_2O respectively.

The vibrations of CuO that were reported to appear at 575, 500, and 460 cm^{-1} [Wang *et al.* 2003], [Bocuzzi 1999] were not observed, in the calcined samples partly due to overlap with support vibrations. The main reason for the absence of these vibrations is the poor ordering of the metal oxide being present in a loading around 2 hypothetical monolayer. Such interface modes will be very broad and remain largely undetected by vibrational spectroscopy. In the precursor materials no oxide but rather a poorly defined oxy-hydrate should be present as active material in this state consists likely of residual ligands and oxo-ligands. The broad bands which can be observed at 3430 cm^{-1} and 1630 cm^{-1} were assigned to the stretching vibrations of OH species and molecular H_2O respectively [Leofanti et al., 2000]. These groups and molecules cover the whole oxide surface being terminated with a substantial number of hydroxyl groups as can be concluded by the wetting of water molecules. The strong peak of water molecules also points to capillary filling of micropores in the oxide secondary structure.

The spectra of both precursor samples M1 and M2 (Figure 4.23), demonstrate broad stretching C-H vibration peak of the citrate ligand at 3151 cm^{-1} which is used as precursor in the sample preparation .There is also indication of C-O stretching which has two strongly coupled C-O bonds with bond strengths intermediate between C=O and C-O in both precursors. This band is not observed in the spectra of both calcined samples. The carboxylate ion gives rise to two bands; a strong asymmetrical OCO stretching band near 1600-1700 cm^{-1} and a weak symmetrical OCO stretching band near 1300-1400 cm^{-1} in the precursor spectra [Cosimo *et al.*, 1992]. However, the first band is not observed probably because the peak has been overlapped with the broad peak of H-O-H bending motion of free water. The weak symmetrical band is clearly observed at 1390 cm^{-1}. The similarity of the spectra of both precursors tells that they contain the same functional groups in both dried samples which in line with the UV-Vis spectroscopy characterisation.

The FTIR spectra of calcined M1 and M2 (Figure 4.24) do not show significant differences from one another. Elimination of carboxylate ion characteristic bands near 1600-1700 cm^{-1} and weak symmetrical OCO stretching band near 1300-1400 cm^{-1} are observed in M2 samples. This is expected as the entire citrate precursor and most of the residue of the organic ligand should have been well evaporated during calcination process carried out in air. However sample M1 shows reduced and narrow carboxylate ion characteristic bands near 1600-1700 cm^{-1}. It is probably that some granule particles has trapped carboxylate ion from being removed during calcination process. As mentioned earlier, the vibration band of CuO that was reported to appear at 575, 500, and 460 cm^{-1} cannot be observed due to the presence of broad band at ~ 500 cm^{-1} from the silica support. Elimination of citrate precursor were observed in both sample which showed no bands at 1300-1400 cm^{-1} and 1600-1700 cm^{-1} that represent the bands for citrate precursors. The elimination is accompanied by weight loss in samples as can be seen in TGA result discussed later.

In summary, from the FTIR results it shows that, the decrease in the intensity of carbonyl group from citrate precursor inferred that the decomposition of these ligands took place in a thermally induced redox process where the citrate acted as a reductant whilst that of nitrates as an oxidant. The vibrations from the support dominate both spectra with little modifications irrespective of the proposed incorporation of the Zn/Ni component into the silicate matrix. This is due to the measuring technique allowing molecular water to fill the pore system of the catalyst. Any more detailed analysis would require studying the samples in absolute exclusion of water and under dynamical removal of the hydroxyl groups. Under such conditions it can be expected that the effect of structural modifiers detectable by FTIR is no longer dominated by the water and hydroxyl structures. Under such conditions, it may also be possible to detect some combination vibrational signals from the copper component being present as nanoparticles.

Table 4.12: FTIR absorption band position assignments of dried precursors and calcined samples M1 and M2.

Wavenumber [cm^{-1}]	Observation and Peak Assignment	
	Precursor sample	Calcined Sample
3452	**M1**:Vibration of O-H **M2**: Vibration of O-H	**M1**:Vibration of O-H **M2**: Vibration of O-H
3151	**M1**:Vibration of C-H **M2**:Vibration of C-H	**M1**:Disappeared after calcinations **M2**:Disappeared after calcinations
1626	**M1**: H-O-H bending motion of free water and strong asymmetrical OCO stretching **M2**: H-O-H bending motion of free water and strong asymmetrical OCO stretching	**M1**:Reduced band observed after calcinations **M2**:Disappeared after calcinations
1396	**M1**:Weak symmetrical OCO stretching band **M2**:Weak symmetrical OCO stretching band	**M1**:Disappeared after calcinations **M2**:Disappeared after calcinations
1109,815	**M1**:-Si-O stretching vibration of silica **M2**:-Si-O stretching vibration of silica	**M1**:-Si-O stretching vibration of silica **M2**:Reduced band observed after calcination

486	**M2**:-O-Si-O vibration of silica	**M2**: Reduced band observed after calcinations

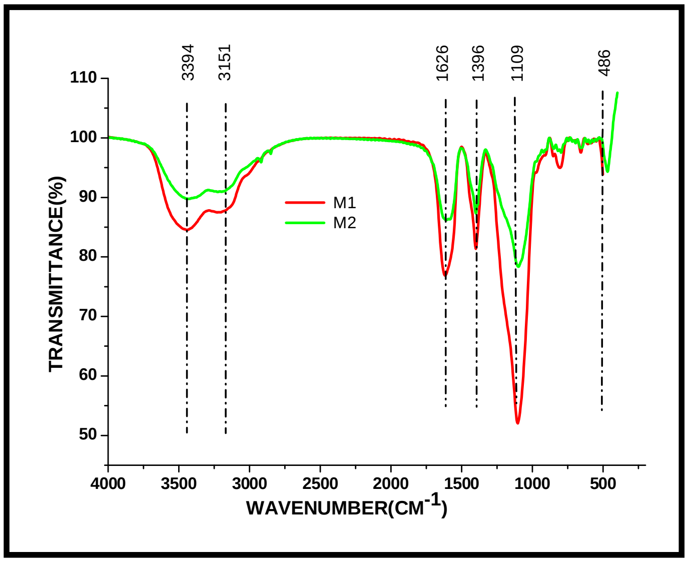

Figure 4.23: FT-IR spectra of precursor samples M1 and M2

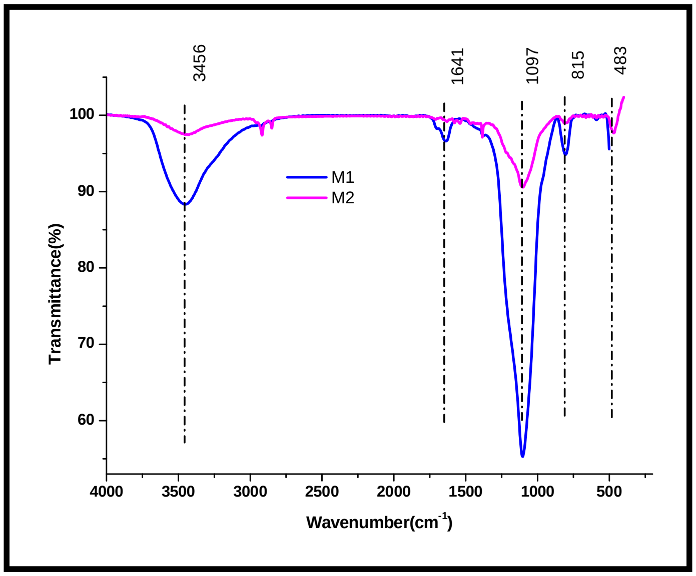

Figure 4.24: FT-IR spectra of calcined samples M1 and M2

4.3 Thermal Analysis

4.3.1 Thermal Gravimetric Analysis – Mass spectroscopy (TGA- MS)

TGA coupled with the mass spectroscopy allows the identification of the numbers of reaction and decomposition processes involving evaporation of small molecules from ligands and water removal from condensation or drying process. Mass spectroscopy was used in order to analyse the gaseous product evolved during the real calcination process. Analysis was carried out in air to allow direct comparison with real calcination condition. The analysis was done to both precursor samples. The observed weight losses at various temperatures in TGA measurement is tabulated in Table 4.13 whilst results of TGA–MS in Figures 4.25-4.30. The first derivative of the TGA (DTG) was plotted as well as to track changes in weight loss during analysis. The discussion of mass spectrometer data will only focused on the major peaks which indicate gaseous released by the high intensity of detected m/e value in the temperature range of weight loss observed in TGA analysis.

Table 4.13: Weight losses at various steps and temperatures as obtained from the thermal analysis data.

Precursor	**TGA**				
	1st weight loss		**2nd weight loss**		**Residue (%)**
	T_R (K)	**Wt loss (%)**	**T_R (K)**	**Wt loss (%)**	**Residue (%)**
M1	304-413	5.21	413-561	24.18	70.60
M2	304-396	6.83	396-560	28.25	64.91

The citrate route has been widely used to synthesize oxide nanoparticles for its many advantages such as homogenous mixing of the components in atomic scale, good control of the stoichiometry, low cost of reagents. When citrate precursor was heated in the inner atmosphere, the precursor decomposed as water, carbon dioxide, a few carbon monoxides and metal oxide [Lian J.S., *et. al.* (2004)]. The decomposition of metal citrate-precursor is complex and is also known as auto-combustion technique. It has been understood that citrate anions in the precursor undergo thermally induced redox reaction, in which citrate acts as a reductant. Citric acid has three carboxylic and hydroxyl groups for coordinating to metal ions, and therefore prevents the precipitation or phase separation and provides and intimated blending among the constituent ions. The pH 7 for both citrate solution was chosen to prevent any possibility of phase separation during the gel formation. Ammonia solution is used as a reagent to adjust the pH so that, all metal solutions are stable at pH 7 [Kwon *et. al.*, 2002].

Generally, the thermal decomposition of the citrate precursor at the temperature below 600 K proceeds via two well-defined steps (Table 4.13). The two major steps, namely dehydration and decomposition of citrate precursor are followed by formation of metal oxide. The following approximation reaction is postulated to give an idea of citrate precursor decomposition and formation of metal oxide during heat treatment:

1. $M(C_6H_6O_7)_8.\ (n+6)\ H_2O \rightarrow M(C_6H_6O_7)_8.\ 6\ H_2O + nH_2O$
2. $M(C_6H_6O_7)_8.\ 6\ H_2O \rightarrow M(C_6H_6O_7)_8. + 6\ H_2O$
3. $M(C_6H_6O_7)_8 \rightarrow M(C_5H_6O_6)_8 + 8CO$
4. $M(C_5H_6O_6)_8 \rightarrow M(CO_2)_3 + 8(CH_3COCH_3) + 13CO_2$

5. $2M(CO_2)_3 + O_2 \rightarrow 2MO + 6CO_2$

Where M representing binary catalyst system, comprises of supported Cu-Zn

Both precursors samples indicated, the removal of water that is loosely coordinated obtained as early as the sample was heated from room temperature to 413 K. This is clearly observed in first weight loss obtained in TGA curves in Figure 4.25 and Figure 4.27. The observation is supported by the MS result whereby the initial weight loss in TGA analysis was followed by a broad peak of mass number (m/e) of 18 corresponding to water release from both precursor samples (Figure 4.26 and Figure 4.28). Based on the amount of weight loss during the first stage decomposition, lower content of solvated water is found in precursor M1 compared to precursor M2. Limited amount of water will further help to reduce the mobilization effect of the precursor during higher heat treatment and minimize the sintering phenomena which later may promote the formation of large particles. However, atmospheric humidity is one of the factors that will also contribute to the amount of access water in samples. Therefore high water content might also be caused by the high humidity in the lab where the samples were exposed during loading to the instrument [Chen *et. al.*, 2004].

The second stage of decomposition process occurs at the temperature range of 400 K to 570 K. This is the main reaction of the rapid oxidation of the organic ligands that are associated with the decomposition process of citrate precursor metal complexes which were used in sample preparation. At this stage, the metal citrate precursor complex decomposed as, ammonia, water, nitrous oxide and carbon dioxide in the presence of air during calcination as indicated by evolution of m/e 17, 18, 30 and 44 in mass spectrometer (Figure 4.29 – 4.30). According to the literature, this mixture has undergone auto-ignition process under limited oxygen condition [Purohit R.D., 2002]. The semi-decomposed precursor obtained around 410 K is essentially a dehydrated and amorphous mixed citrate. The decomposition has contributed to a sharp weight loss. The percentage weight loss for precursor M1 is 14% less than precursor M2 implying that perhaps the highly dispersed Cu^{2+} species in precursor M1 provide more sites for the ligand to be bounded and therefore more energy is needed to break the bond. The ammonia content in the samples comes from ammonium hydroxide that is used as a solvent to dissolve and to dilute the copper, zinc and nickel citrate salts. The reaction of ammonia with oxygen in air brings about the formation of nitrous oxide as detected by MS.

The oxidation of the organic compound occurs in a rapid and vigorous reaction due to the intramolecular oxidative power of the citrate. The organic chelating compound burns heavily and is accompanied by such heat, which causes a high local temperature [Cosimo 1992]. The weight loss can also be the elimination of citric acid, which weakly interacts with silica and/or metal cation. This is due to citric acid, having one hydroxyl and three carboxyl groups, can form complexes with a metal cation and with a wide variety of structures [Salamiah 2005]. So far, not many literatures have reported on the exact decomposition mechanism of metal citrate precursor probably because metal citrate precursor is too reactive during thermal decomposition and it is hard to control the process. The sharp and narrow peaks of DTG in both precursor decompositions show the abrupt weight loss indicating an explosion-like gas evolution.

In summary, the TGA-MS results have given a picture of the thermal reactivity of the samples allowing several points for further catalyst development. The mass spectroscopic analysis of gaseous products permits to a conclusion that four types of gaseous compounds are released during the two decomposition steps as identified on the DTG curves (Figures 4.29 – 4.30). It is also clearly seen that in both samples, the decomposition was completed at about 550 K to 600 K with no significant weight loss observed after this temperature and the corresponding MS does not show any evolution of gases released.

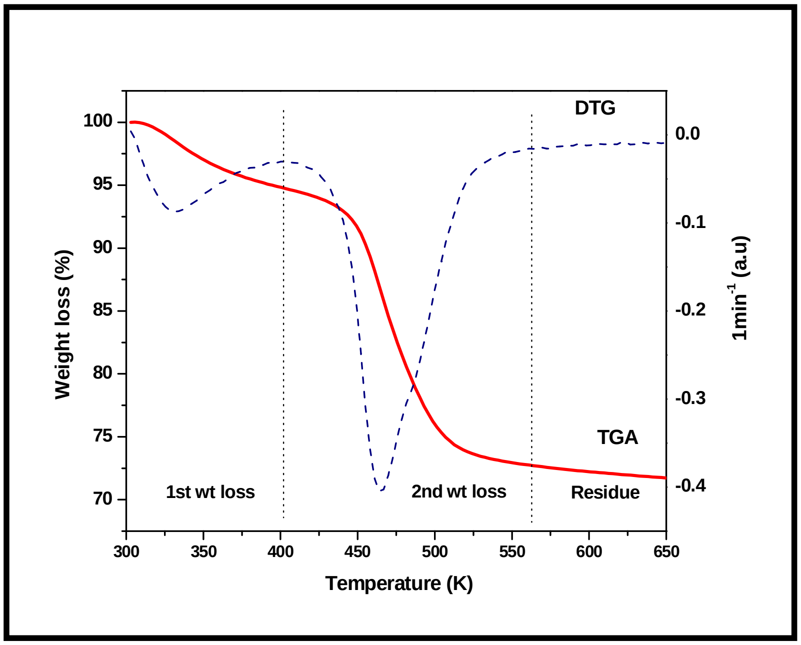

Figure 4.25: TGA thermogram for precursor M1

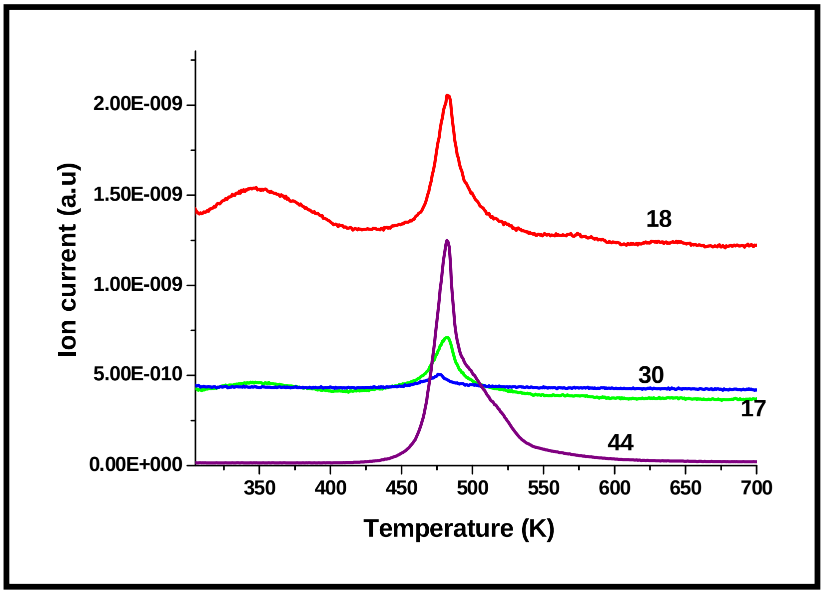

Figure 4.26: Mass spectroscopic analysis of gaseous products during TGA analysis for precursor M1

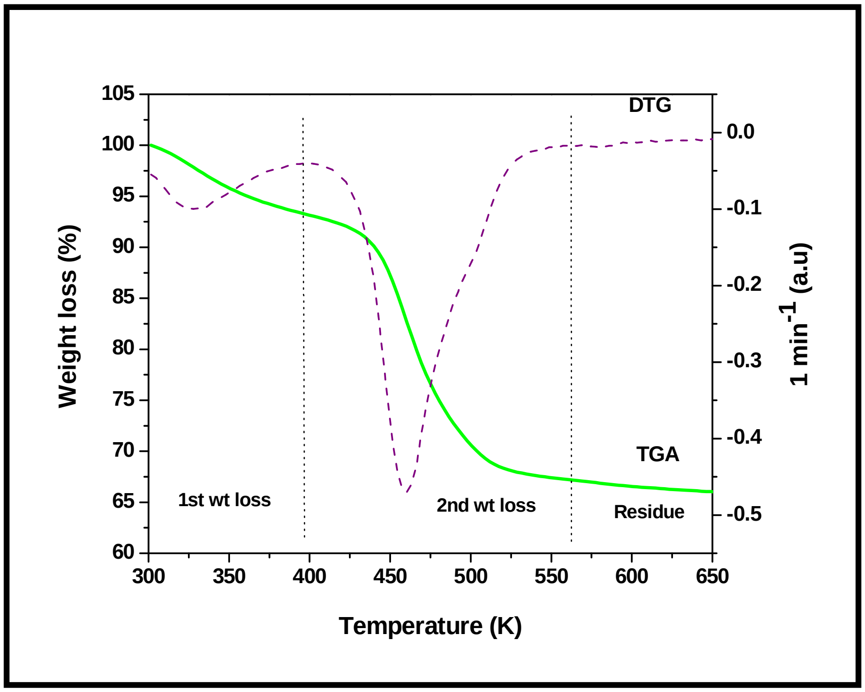

Figure 4.27: TGA thermogram for precursor M2

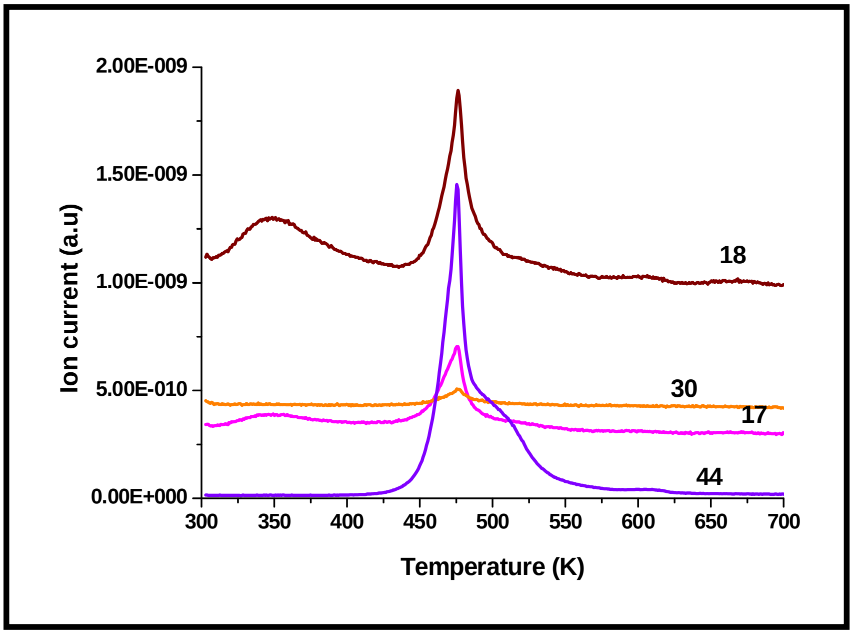

Figure 4.28: Mass spectroscopic analysis of gaseous products during TGA analysis for precursor M2

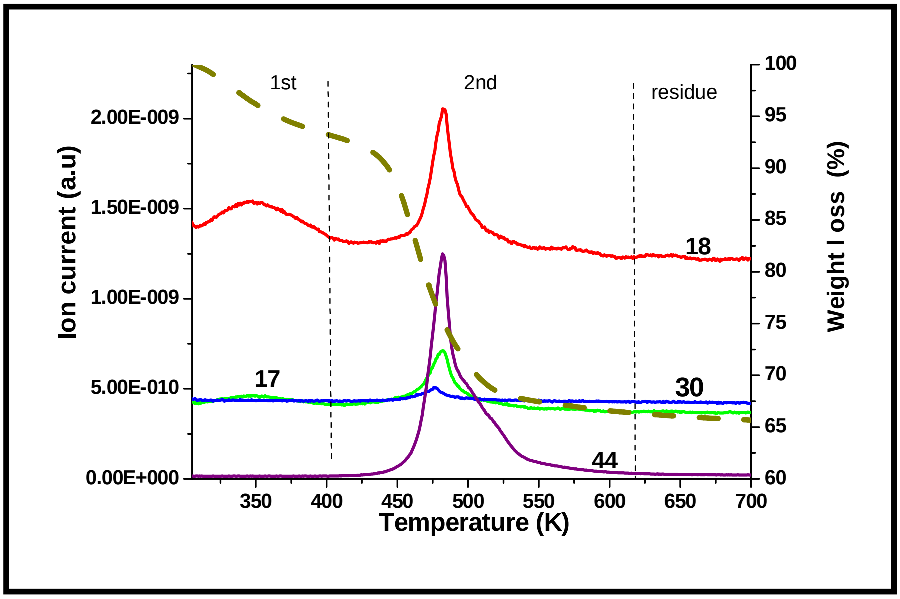

Figure 4.29: TGA thermogram coupled with MS spectrometer for Precursor M1

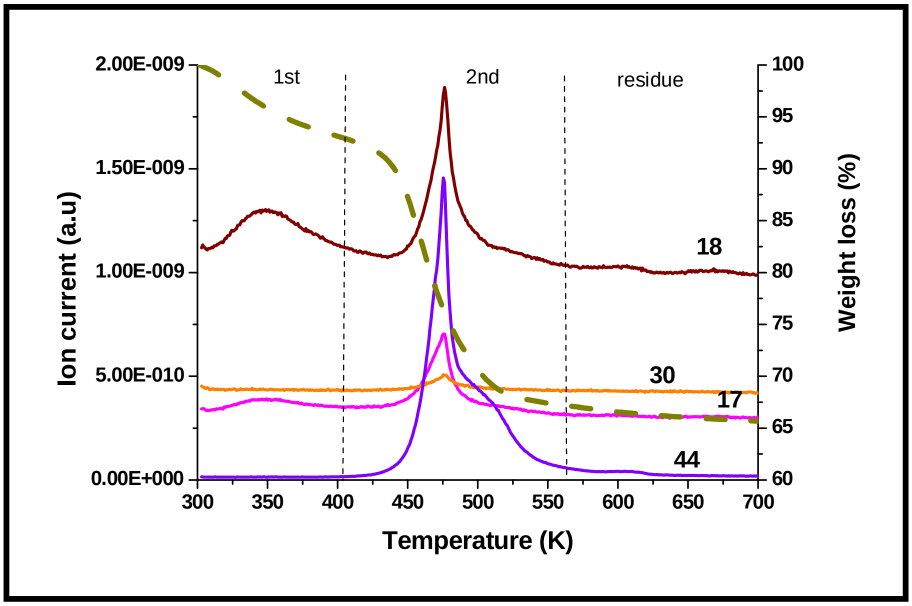

Figure 4.30: TGA thermogram coupled with MS spectrometer for Precursor M2

4.3.2 Differential Scanning Calorimetry (DSC) Analysis

The TGA-MS analysis is supported by the DSC analysis that gives the enthalpy value of endothermic and exothermic reactions during the temperature programmed analysis. During the analysis, precursors were heated from room temperature to 823 K at a heating rate of 2 K min^{-1} under compressed air with a flow rate of 50 ml min^{1}. The same temperature programmed was applied during sample calcination and TGA analysis. Based on the DSC measurement data, both the enthalpy of dehydration and ligand decomposition of both precursors M1 and M2 have been calculated and tabulated in Table 4.14.

Table 4.14: Summary of DSC results for samples precursors

Precursor ID	**DSC**			
	1st Transition		**2nd Transition**	
	T_{range} and T_{endo} (K)	**ΔH (J/g)**	**T_{range} and $T_{exo/endo}$ (K)**	**ΔH (J/g)**
M1	T_{range}= 304-421 T_{endo}= 360	-192.38	T_{range}= 421-593 T_{exo}= 492	1933.48
M2	T_{range}= 304-420 T_{endo} = 359	-324.37	T_{range}= 420-602 T_{exo}= 485	1881.76

Both precursors indicate endothermic peak at almost the same range in the lower temperature region starting at 303 K. This endothermic curve shows energy consumed in the reaction and is accompanied by the first weight loss in the corresponding TGA-MS. Energy was used in the removal of loosely coordinated water content in samples as temperature increased. The endothermic drying stage is terminated around 425 K. Sample M2 shows the higher value of ΔH (324.37 J/g) which indicates that this sample consumed higher energy during the endothermic reaction of water removal compared to the M1 precursor sample. At higher temperature, at which the decomposition of citrate precursors and formation of metal oxide occurred, the exothermic peaks observed in both samples are at slightly different temperature range. The exothermic of reaction started at 450 K and centered at about 490 K indicates the ligand removal from precursor and gaseous released in TGA-MS. The high thermal load of the sample during this process is most likely responsible for the incorporation of the copper into the modified silica support. The rapid kinetics and the short duration do not allow clustering of the copper ions and hence prevent the formation of CuO precipitates inside the silica matrix. Hence, the presence of the organic residues acts as a local fuel to generate the heat required for driving the metal ions into the oxide lattice. The exact nature of ligands is of less relevance than the rapid exothermal decomposition.

The DSC curves of both precursors samples in Figure 4.31 to Figure 4.32 exhibit two-dwell endothermic events next to each other which is interpreted as the removal of loosely coordinated water. This finding supports the postulate made in ligand decomposition in the TGA analysis that shows that the dehydration process is a multi-step reaction. Broad exothermic curve with small hump (shoulders) on the curves are observed in both precursors, indicating that more than one reactions have happened during citrate decomposition.

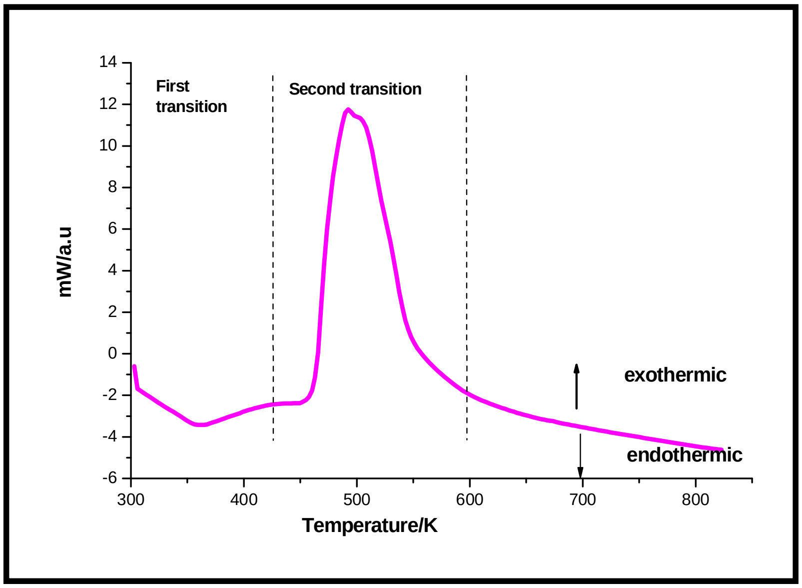

Figure 4.31: DSC analysis of precursor M1

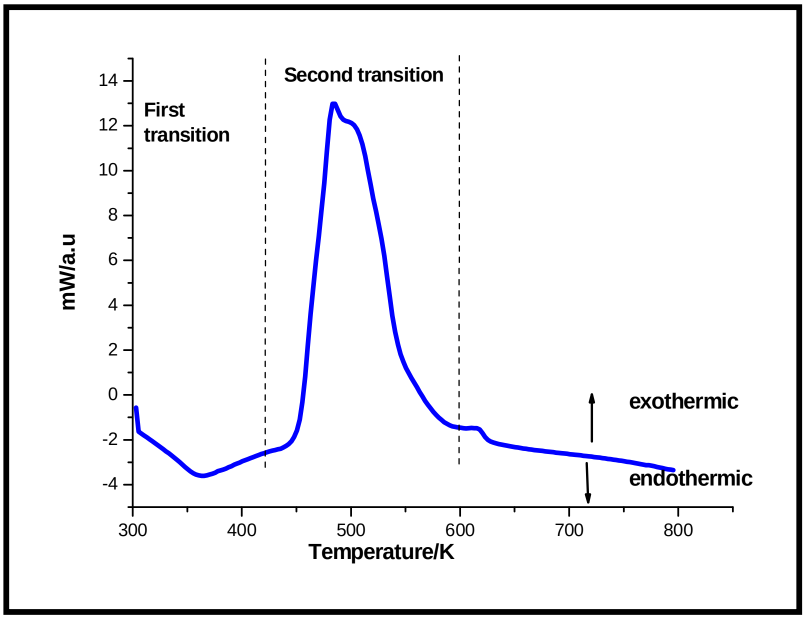

Figure 4.32: DSC analysis of precursor M2

4.3.3 Temperature Programmed Reduction (TPR)

The temperature-programmed reduction (TPR) is a thermal method that used in analysis of metal oxide reduction and it is very useful to predict the catalytic potential of the catalyst with the absence of the catalytic data. As a finely divided metallic copper has been identified to be the catalytically active component, it is appropriate to use TPR for investigating the kinetic of the generation of the active copper species. Typically, a sample is subjected to the predetermined linear heating rate and measuring the consumption of H_2 to monitor the reduction of the sample. Its quantification is also very valuable to give information about the capability of copper reduction into active species [Lee 2004].

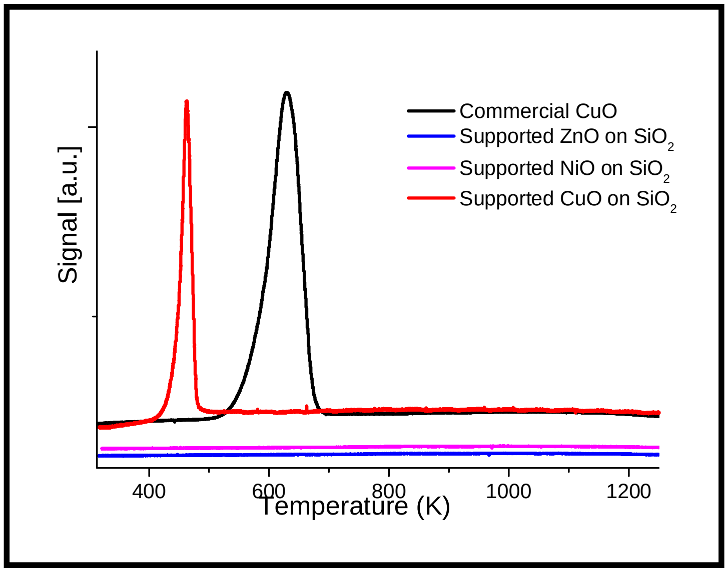

Figure 4.33: Hydrogen consumption during conventional temperature-programmed reduction (TPR) of the commercial CuO (black), supported ZnO on silica (blue). supported NiO on silica (purple) and supported CuO on silica (red).

Figure 4.33 reports the TPR profile of commercial CuO obtained from Aldrich (99% purity), CuO, ZnO and NiO supported on silica. The commercial CuO profile consists of one reduction peak whereby the onset temperature is apparent at 516 K. The peak reaches a maximum at 623 K and reduction of the CuO to Cu^0 is completed at about 621 K. No hydrogen consumptions were observed in ZnO and NiO supported on silica indicating that ZnO and NiO did not exhibit a reducible species. This is in good agreement with the other characterization results discussed earlier that also observed that the active component in bimetallic supported Cu-Zn and Cu-Ni material is apparently CuO. The zinc and nickel components which act as second metal in the catalysts only play role as textural promoter as predicted earlier in Chapter 4. A. Maa'mor in his thesis claimed that the addition of zinc on bimetallic Cu-Zn catalyst system will slightly increase the performance of the catalyst and nature of the CuO is hardly affected by the second metal (Zn) [Maamor 2005].

On the other hand the reduction of CuO shifted to lower temperature when the mono-metallic CuO deposited to the silica support compared to the bulk CuO. As indicates in the TPR profile the reduction temperature started at 419 K with maximum at 463 K. After 497 K, all active components have been reduced and no other reductions were observed at high temperature. As a matter of fact, it is well known that highly dispersed CuO is easier to reduced, which also means it can easily reduced at lower temperature compared to the bulk CuO.

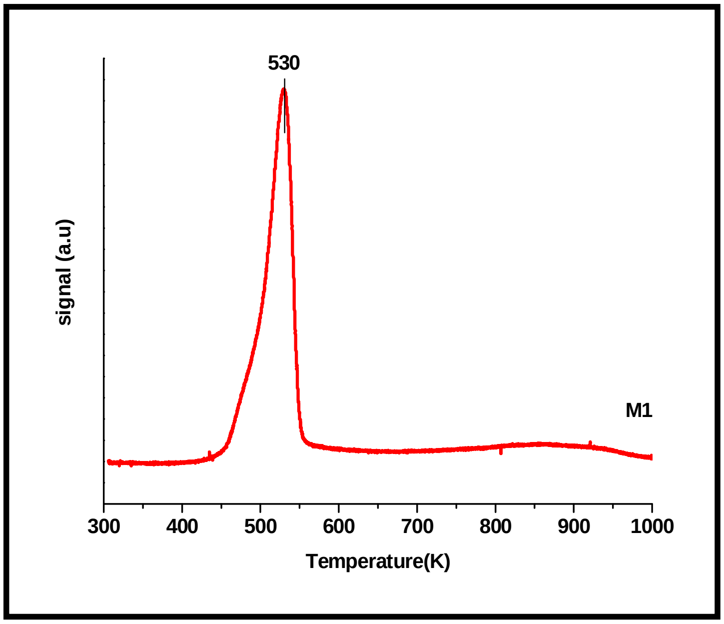

Figure 4.34: TPR profiles sample M1

The TPR profile of calcined M1 sample is shown in Figure 4.34. The profile corresponds to the reduction of CuO

$$CuO + H_2 \longrightarrow Cu^0 + H_2O$$

The TPR profile exhibits characteristic small shoulders left to the main reduction peak, which shows an indication of two overlapping peaks. The onset temperature is apparently at 423 K. At around 456 K, H_2 consumption increases rapidly reaching to maximum at 530 K and reduction is completed at about 580 K. There is no indication of ZnO reduction in the TPR profile. N. Ram Mohan claimed that the silica support has been modified at high reduction temperature by zinc at the location of copper oxide particles [Mohan N. R. (2005)]. However, only some of the modified zinc is incorporated with copper oxide particle while the rest of zinc component remains inactive sitting on copper and only acting as textural promoter to strengthen the role of active component on the support. Sample M1 is also found easier to be reduced compared to compared bulk copper oxide, which will only reduce at about 640 K. This indicates that it is also important to disperse the CuO particles on support material with homogenous distribution.

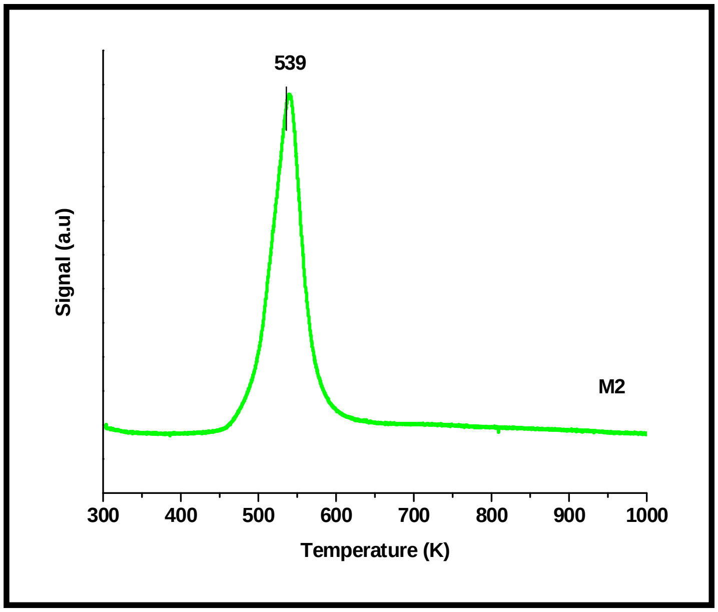

Figure 4.35: TPR profiles sample M2

The TPR profile of calcined M2 sample is shown in Figure 4.35. The profile corresponds to the reduction of CuO

$$CuO + H_2 \longrightarrow Cu^0 + H_2O$$

The TPR profile exhibits almost symmetrical characteristic and no indication of NiO reduction in the TPR profile. The onset temperature is apparently at 415 K. At around 478 K, H_2 consumption increases rapidly reaching to maximum at 539 K and reduction is completed at about 627 K. A slightly higher maximum reduction temperature is observed compared to M1 sample. This observations also support the characterization by XRD showing crystalline CuO (tenorite) phase.

Subsequently the higher thermal treatment increase the particle size by sintering the most reactive small copper particles, decreasing the peak width and making the profile more symmetrical. This is clearly observed in sample M2 that have symmetrical shape of TPR profile compared to M1. The estimation of the reduction of copper was carried out for both samples with results being reported in Table 4.15 Approximate calculation was made based on assumptions:

1. There are no loss of active metal copper from Cu-Zn and Cu-Ni during synthesis
2. All copper in Cu-Zn and Cu-Ni on silica transformed to metal oxide after calcinations in oxidative atmosphere in one step:

$$CuO + H_2 \longrightarrow Cu^0 + H_2O$$

The experimental value of total hydrogen consumption is represented in terms of area under peak calculated by computer software.

Table 4.15: Summary of Temperature Programmed Reduction of calcined samples M1 and M2

Sample ID	**T_{max} / K**	**Experimental H_2 Consumption / µmol g^{-1}**	**Calculated H_2 Consumption / µmol g^{-1}**	*** Max. reduction of copper (%)**
M1	530	3191.80	3100.00	97.1
M2	539	3544.10	3200.00	90.3

Sample M1 shows higher percentage reduction of CuO into metallic copper compared to sample M2. As mentioned earlier large amount of active surface area content in M1 sample has undergone complete reduction.

In summary, it should be noted that the TPR measurement cannot be explained only in terms of copper dispersion. When the results are compared with XRD and surface area measurement, it is clear that factors other than dispersion, e.g., CuO crytallinity and interaction between copper and oxide support, influence the reducibility of the catalytic material. Large crystallites tend to be reduced more slowly than small ones due to their relatively small surface area exposed to hydrogen. Finally, there is also clear evidence that there is no bimetallic system present and the active component is only Cu metal supported on modified oxide that has incorporated the second metal (Zn or Ni).

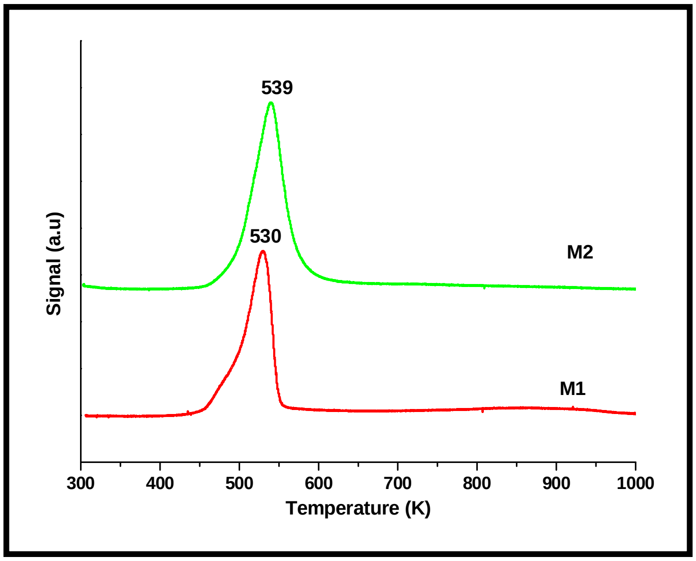

Figure 4.36: Summary of Temperature Programmed Reduction of calcined samples M1 and M2

CHAPTER 5

HYDROGENATION OF FATTY ALCOHOLS TO FATTY AMINES

5.1 Introduction

The reaction of ammonia with primary, long-chain alcohols is known. A large number of catalysts suitable for the said liquid-phase amination of fatty alcohols with ammonia have been disclosed, e.g. in U.S. Pat. No. 4,409,399, describing the state of the art of liquid-phase amination processes. By `liquid phase`, means an amination process wherein the alcohol is in the liquid phase, while the ammonia or the primary or secondary amines are in the liquid or gaseous phase under the reaction conditions defined hereinafter. However, it is difficult to selectively produce a specific amine, especially a primary amine, by reacting an alcohol with ammonia. Normally, secondary and tertiary amines are produced in large quantities whenever the reaction is carried out with the aim of achieving high conversionrates.

A wide variety of metal catalysts are used for the amination of alcohols, e.g. nickel, copper, chromium, cobalt, zinc and iron, or the oxides thereof, optionally in combination with alkali and alkaline earth metals as co-catalysts. Commercial hydrogenation of fatty alcohol to fatty amines is performed utilizing copper-based catalysts, typically at temperatures ranging from 423-523 K and at pressures 1-100 bar. The molar ratios of ammonia to alcohol can be in the range of 3:1 to 3.5:1. Developing low-pressure processes has long been a prime industrial target. Therefore, research effort nowadays focuses on creating active catalysts to allow processing elow 100 bar and on chromium-free copper catalysts to reduce environmental pollution.

5.2 Hydrogenation of Fatty Alcohol (Reaction Pathway)

The process to produce amines comprises of reacting of an aliphatic alcohol (lauryl alcohol) with an aminating agent selected from the group consisting of ammonia, in the liquid phase in the presence of a supported catalysts i) Cu-Zn/SiO_2 ii) Cu-Ni/SiO_2.

The main reaction in the hydrogenation of fatty alcohol to fatty amines is composed of three steps:

(1) dehydrogenation of dodecyl alcohol to dodecyl aldehyde (R′ CHO) over Cu;
(2) addition of NH_3 to the formed aldehyde;
(3) the hydrogenolysis of the NH_3–aldehyde adduct to form RNH_2 and water over Cu-Zn/SiO_2 or Cu-Ni/SiO_2

$$\mathrm{ROH} \leftrightarrows \mathrm{R'CHO} + \mathrm{2CuH} \quad \text{(dehydrogenation)} \tag{1}$$

$$\mathrm{R'CHO} + \mathrm{NH_3} \leftrightarrows \mathrm{R'CH(OH)NH_2} \quad \text{(addition of } \mathrm{NH_3} \text{ to the aldehyde)} \tag{2}$$

$$\mathrm{R'CH(OH)NH_2} + \underset{\substack{\text{or} \\ \text{Cu-Zn/SiO}_2}}{\text{Cu-Ni/ SiO}_2} \leftrightarrows \mathrm{R'NH_2} + \mathrm{H_2O} \quad \text{(hydrogenolysis of the adduct)} \tag{3}$$

The amination of alcohols involves a reaction between ammonia and alcohol in the presence of hydrogen gas. The catalytic amination process consists of hydrogenation and dehydrogenation reactions. The mechanism of these various reactions have been extensively discussed in the literature as illustrated in the seven reaction equations below consisting of a series of sequential steps (Figure 5.1): The first step in the amination process is a reversible dehydrogenation of the alcohol to give an intermediate carbonyl [eq. 1]. The aldehyde is then converted to an aminoalcohol [eq.

2] by reaction with ammonia or an amine present in the reaction mixture. The aminoalcohol then loses water to form the imine [eq. 3]. The imine is then hydrogenated to the amine [eq. 4]. Equations 5, 6, and 7 illustrate the possible products formed by the reaction of the intermediate imine with ammonia or amines present in the reaction mixture.

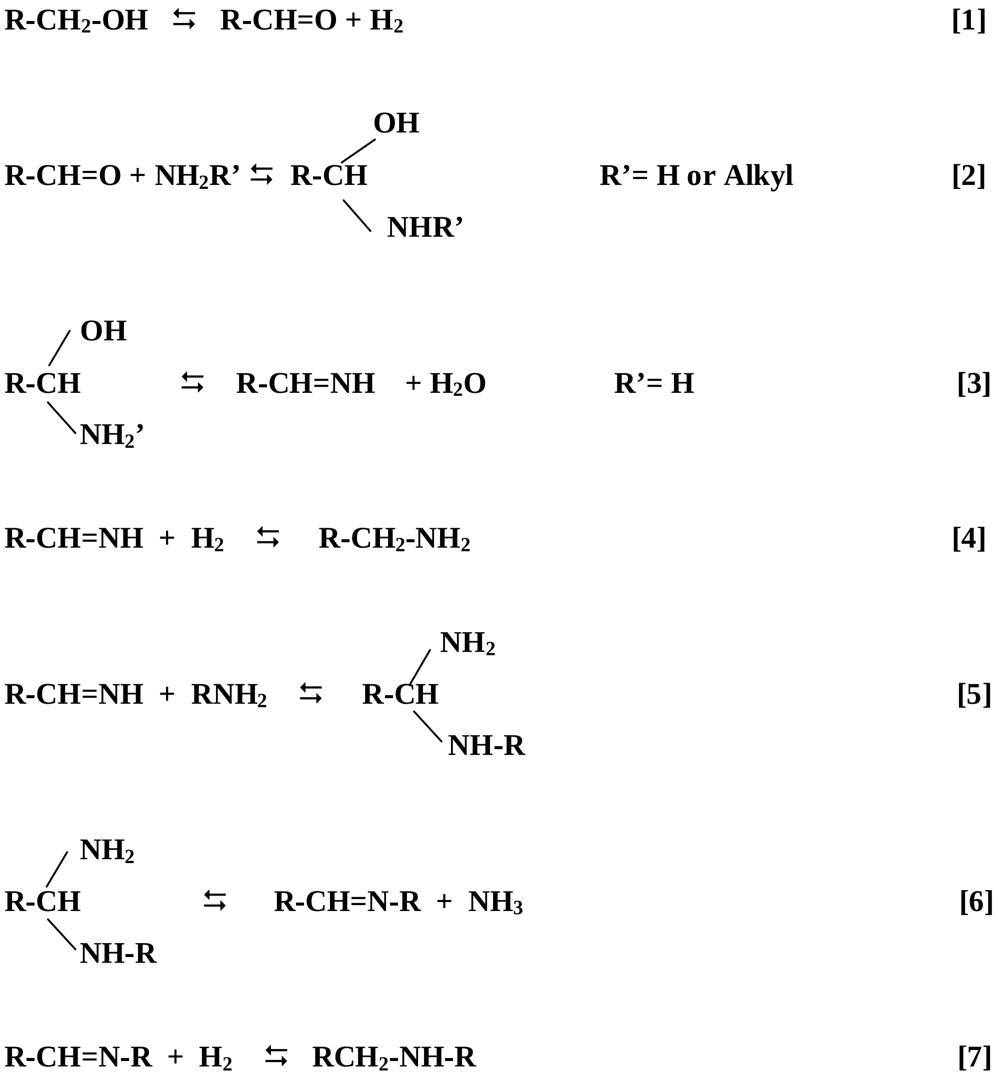

$$\mathbf{R\text{-}CH_2\text{-}OH \rightleftarrows R\text{-}CH{=}O + H_2} \qquad [1]$$

$$\mathbf{R\text{-}CH{=}O + NH_2R' \rightleftarrows R\text{-}\overset{OH}{\underset{NHR'}{CH}}} \qquad \mathbf{R' = H \text{ or Alkyl}} \qquad [2]$$

$$\mathbf{R\text{-}\overset{OH}{\underset{NH_2'}{CH}} \rightleftarrows R\text{-}CH{=}NH + H_2O} \qquad \mathbf{R' = H} \qquad [3]$$

$$\mathbf{R\text{-}CH{=}NH + H_2 \rightleftarrows R\text{-}CH_2\text{-}NH_2} \qquad [4]$$

$$\mathbf{R\text{-}CH{=}NH + RNH_2 \rightleftarrows R\text{-}\overset{NH_2}{\underset{NH\text{-}R}{CH}}} \qquad [5]$$

$$\mathbf{R\text{-}\overset{NH_2}{\underset{NH\text{-}R}{CH}} \rightleftarrows R\text{-}CH{=}N\text{-}R + NH_3} \qquad [6]$$

$$\mathbf{R\text{-}CH{=}N\text{-}R + H_2 \rightleftarrows RCH_2\text{-}NH\text{-}R} \qquad [7]$$

Figure 5.1: Schematic reaction process of hydrogenation of fatty alcohol to fatty amines [Nemphos et.al., 1997]

5.3 Catalyst Testing Procedure

The catalysts were tested in a high-pressure oleobed reactor platform (refer to Chapter 3), operating at 30 bars of hydrogen pressure and 443-523 K. The reactors are equipped with over head stirrers, temperature control, pressure control and a gas feed system to monitor the gas uptake.

The catalysts were pre-treated with hydrogen at 623 K in the pre-treatment unit. Approximately 200 mg of catalyst was weighed into the glass pre-treatment reactors (exact weight noted). The reactors were closed by attaching the bulb on the top of the pre-treatment with glass unit. The pre-treatment reactor was evacuated and purged with nitrogen several times to remove the air inside the reactor and catalyst bulb. The gas supply to the reactors was switched from nitrogen to hydrogen and the reactors were heated with a ramp of 5 ^{o}C min^{-1} to 623 K. The catalysts were kept under hydrogen flow at 623 K for 2 hours. After cooling the reactors were flushed with nitrogen and removed from the reactor rig. The catalysts were transferred to the bulbs by placing the reactors upside down and the bulbs were sealed with a torch. The catalyst ampoules were then stored until use in the hydrogenation reaction. For the hydrogenation reactions the catalysts ampoules were mounted in the PEEK holders that are inside the reactors. The reactors were filled with 15 mL of dodecanol and 45 mL of 25% ammonia solution. The reactors were sealed, flushed with nitrogen to remove any air and pressurized to 50 bars for a leak check. After the leak check the reactors were depressurized flushed with hydrogen and pressurized with hydrogen up to 30 bars. At 30 bars the reactors were heated to the reaction temperature, after which the reactors were left to stabilize at the reaction temperature. At stable reaction temperature the pressure was elevated to 80 % of the reaction pressure via the direct feed. The final 20 % of hydrogen were fed by the dosing system to prevent an overshoot in pressure. The stirrer was started after stabilization of the temperature and pressure. This action broke the catalyst bulb and released the catalyst into the reaction mixture, thereby starting the reaction (t=0). Figure 5.2 shows the historical trend of hydrogenation of Fatty Alcohol using Oleobed. During the reaction the pressure was kept constant by the gas dosing system. Gas consumption by reaction caused the pressure in the reactor to drop below the set point pressure, at which moment a valve between the reactor and the gas dosing vessel opened for a short time to replenish hydrogen. At all times the pressure in the gas dosing vessel were 10 bars higher than the reactor pressure to allow flow from the dosing vessel to the reactor. The amount of gas consumed by reaction can be calculated from the pressure profiles and temperature in the gas dosing vessel. When the pressure in the gas dosing vessel dropped below the reactor pressure + 2 bar, the gas dosing vessel was refilled automatically to the gas dosing set point pressure. At the end of the reaction, the gas dosing was stopped and fast mantle cooling was used to cool the reactor.

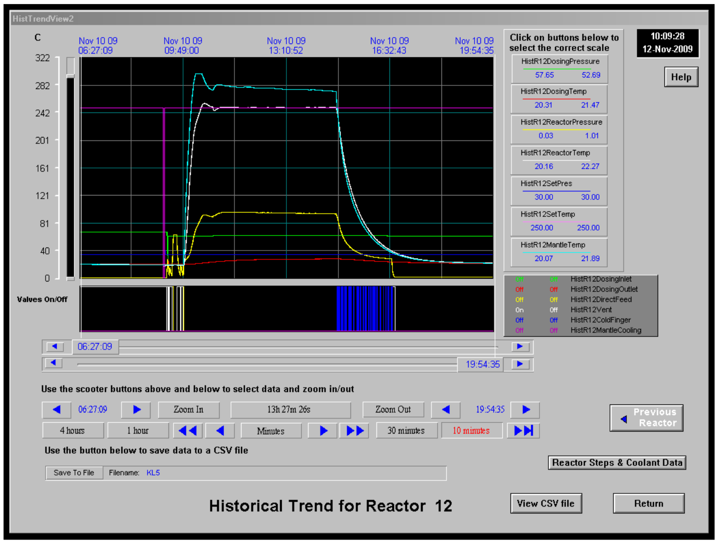

Use the scooter buttons above and below to select data and zoom in/out

Use the button below to save data to a CSV file

Historical Trend for Reactor 12

Figure 5.2: Historical trend of Hydrogenation of Fatty Alcohol using Oleobed

5.4 Analysis of Products

The samples were collected, filtered and analysed by Nuclear Magnatic Resonans Spectroscopy (NMR) and Fourier Transforms – Infrared Spectroscopy (FT-IR).

5.4.1 Nuclear Magnatic Resonans Spectroscopy (NMR)

NMR spectra were recorded in $CDCl_3$ at room temperature on a BRUKER 500 (11.7 T, 500.13 MHz for ^1H) using 5 mm BBO probe.^1H chemical shifts (ppm) were measured with and accuracy of 0.01 ppm and refered to $CDCl_3$ (^1H, 7.24 ppm). In order to obtain 1H NMR spectrum, the pulse sequence used a delay (D1) and acquisition time (AQ) of 1.0 s and 10.9 s, a spectral width of 3001.2 Hz, 16K data points, 90◦ pulse (14.15_s) and 16 scans. NMR is a powerful spectroscopic technique that gives information about both the structural and chemical properties of certain molecules. NMR is unique as it is one of the few non-destructive methods for analyzing structure and molecular dynamics. Proton NMR works by exploiting the behavior of ^1H atoms when they are placed in a very strong magnetic field. An approximate chemical shift ranges (ppm) for types of protons in amines and alcohols are tabulated in Table 5.1

Table 5.1: Approximate chemical shift ranges (ppm) for types of protons [John Voodeling 2001].

Protons	Chemical shifts (ppm)	Peak assignment
R-C**H**$_3$	0.7-1.3	Methyl groups are often recognizable as a tall singlet, doublet, or triple even when overlapping other CH absorptions.
R-C**H**$_2$-R	1.2-1.4	In long chains all of the methylene (CH_2) absorptions may be overlapped in an unresolvable group.
R-N-**H**	0.5-4.0	Hydrogens attached to a nitrogen have a variable chemical shift depending on the temperature, acidity, amount of hydrogen bonding, and solvent.
-C**H**-N	2.2-2.9	The α hydrogen slightly deshielded due to the electronegativity of the attached nitrogen.
C-O**H**	0.5-5.0	The chemical shift of the –OH hydrogen is variable, its position depending on concentration, solvent and temperature. The peak may be broadened and its base by the same set of factors.
C**H-O-H**	3.2-3.8	Protons on the α carbon are desheilded by the electronegative oxygen atom and are shifted downfield in the spectrum.
$CDCl_3$	7.77	Solvent

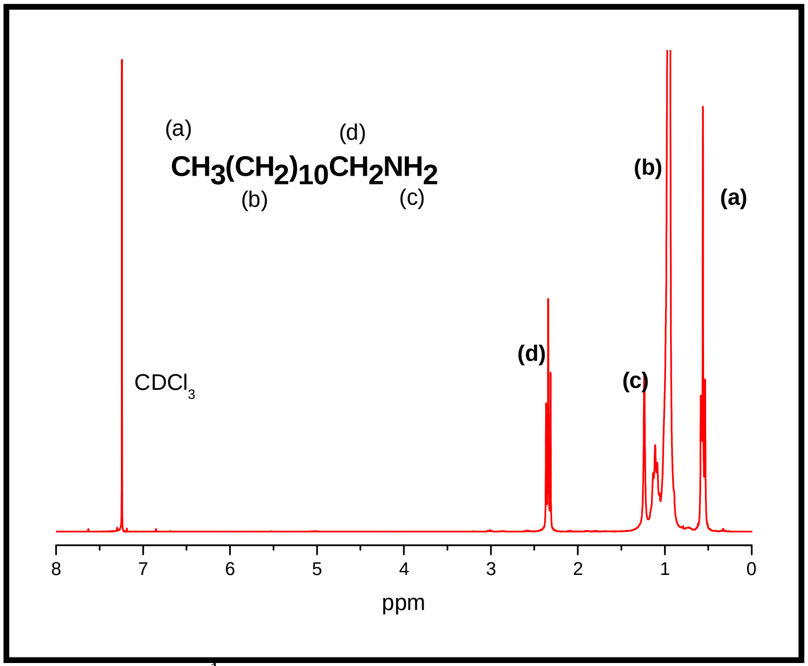

Figure 5.3: ^{1}H NMR spectrum of Dodecylamines (in $CDCl_3$)

Two characteristic types of hydrogens are found in amines: those attached to nitrogen (the hydrogens of the amino group) and those attached to the α carbon (the same carbon to which the amino group is attached). A spectrum of dodecylamines is shown in Figure 5.3. Hydrogens in methyl groups**(a)** are the most highly shielded type of proton and are found at chemical shift values lower 0.7-1.3 ppm, followed by methylene**(b)** in range 1.2-1.4 ppm. In long hydrocarbon chains, or in larger rings, all of the C**H** and C**H**$_2$ absorptions may overlap in an unresolvable group. Methyl group peaks are usually separated from other types of hdrogens, being found at lower chemical shifts (higher field). However, even when methyl hydrogens, are located within an unresolved cluster of peaks, the methyl peaks can often be recognized as tall singlets, doublets, or triplets clearly emerging from the absorptions of the other types of protons. The integral can be can also be used to estimate the total number of hydrogens (the ratio of CH_3 to CH_2-type carbons) since all of the CH_2 hydrogens are in one group and the CH_3 hydrogens are in the other. Location of the –N**H** absorption**(c)** is not reliable method for the identification of amines. These peaks are extremely variable, appearing over a wide range of 0.5-4.0 ppm, and the range is extended in aromatic amines. The position of resonance is affected by temperature, acidity, amount of hydrogen bonding, solvent or the presence of water in the solution. In addition to this variability in position, the –N**H** peaks are often very broad and weak without any distinct coupling to hydrogens on an adjacent carbon atom. This condition can be caused by chemical exchange of the –N**H** proton, or by a property of nitrogen atoms called quadrupole broadening. The hydrogen α to the amino group**(d)** are slightly deshielded by the presence of the electronegative nitrogen atom, and they appear in the range 2.2-2.9 ppm.

In Figures 5.4 and 5.5 show NMR spectra of fatty amines formed form the, hydrogenation of fatty alcohol using catalysts M1 and M2 respectively in temperature range of 443 K-523 K. Hydrogens in methyl groups are found at chemical shift of 0.7-1.3 ppm and methylene goups are found in range of 1.2-1.4 ppm. The hydrogens α to the amino group $–CH_2-NH_2$ appear in the range of 2.2-2.9 ppm. The location of the –N**H** absorption is weak, due to chemical exchange of the –N**H** proton. The presence of water in the solution can be seen in chemical shift 4.0-5.5 ppm and has affected to the –N**H** proton. The amino hydrogens will exchange with H_2O causing the peak to disappear from the spectrum (or to have its intensity reduced). In simple amines, intermolecular proton exchange is usually fast enough to decouple spin-spin interactions between protons or nitrogen and those on the α carbon atom. Under such conditions, the amino hydrogens usually appear as a sharp singlet (unsplit), and in turn the hydrogens on the α carbon are also not splitted by amino hydrogens. The rate of exchange can be made slower by making the solution strongly acidic (pH<1) and forcing the protonation equilibrium to favor the quaternary ammonium cation rather than the free amine [John Voodeling, 2001].

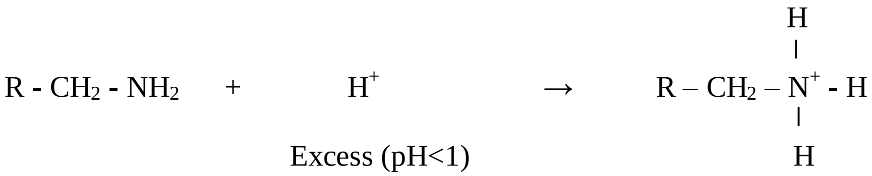

$$R - CH_2 - NH_2 \quad + \quad \underset{\text{Excess (pH<1)}}{H^+} \quad \rightarrow \quad R - CH_2 - \overset{\overset{H}{|}}{\underset{\underset{H}{|}}{N^+}} - H$$

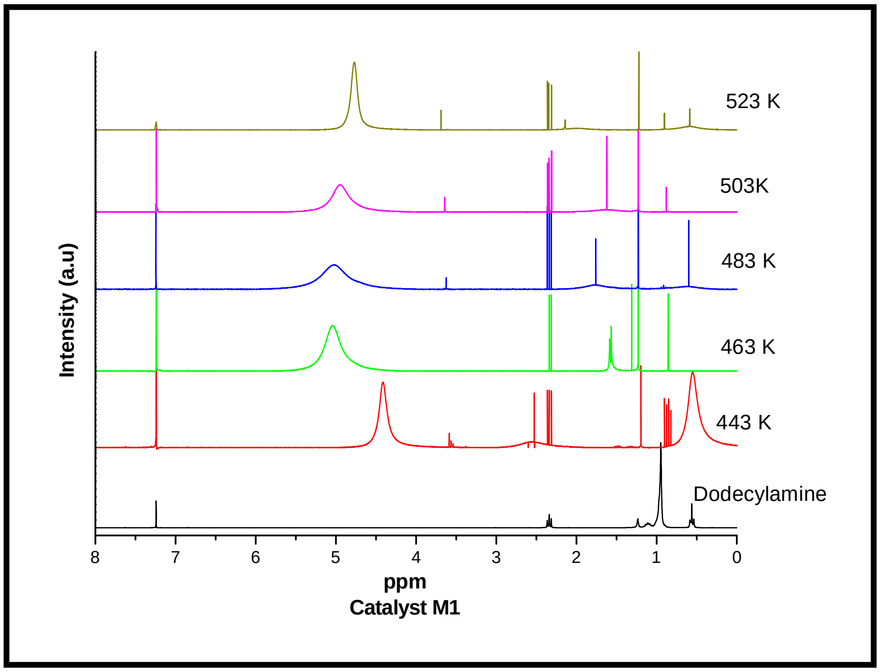

Figure 5.4: ^{1}H NMR spectrum of hydrogenation of fatty alcohol using catalyst M1

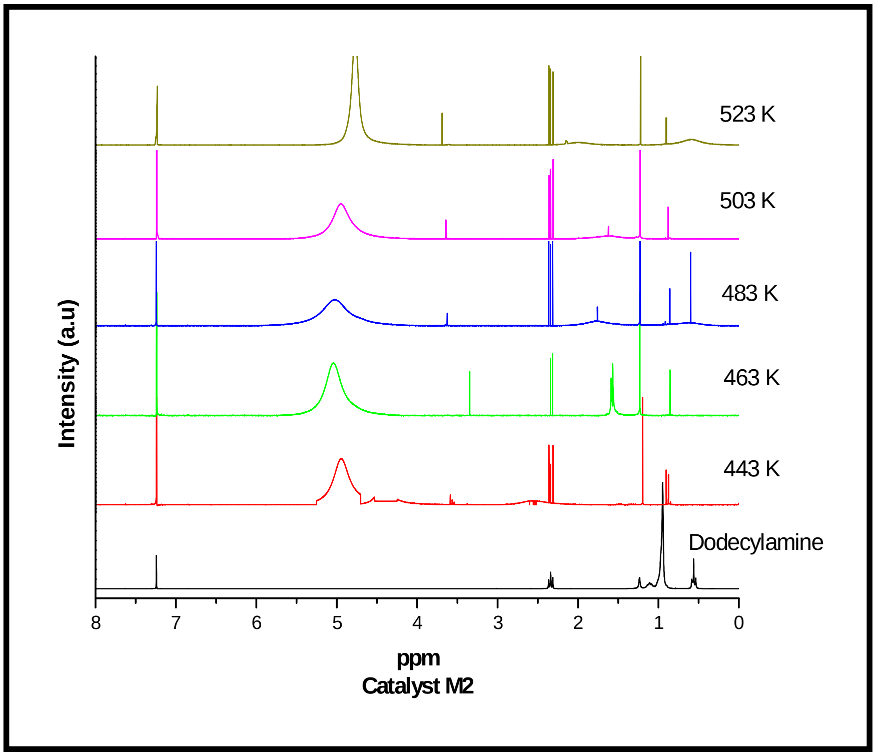

Figure 5.5: ^{1}H NMR spectrum of hydrogenation of fatty alcohol using catalyst M2

Not much information can be revealed from NMR on product yield and thus the catalyst activity and selectivity to obtained more, FTIR was carried out.

5.4.2 Fourier Transforms Infrared Transmission (FT-IR)

Fourier transform infrared transmission (FTIR) spectra were recorded with a Bruker spectrometer model IFS 66v/s, with a resolution of 4 cm^{-1} in the Middle range. Before analysis, air evacuation was done under vacuum (5 mbar) for 15 minutes. Table 5.2 shows FTIR absorption band assignment generally found in amines.

Table 5.2: FTIR absorption band assignment in amines [John Voodeling 2001].

Band	Observation
N-H	Strecth occurs in the range 3500-3300 cm^{-1}. Primary amines have two bands. Secondary amines have one band: a vanishingly weak one for aliphatic compounds and a stronger one for aromatic secondary amines. Tertiary amines have no N-H stretch.
N-H	Bend in primary amines results in a broad band in the range 1640-1560 cm^{-1}. Secondary amines absorb near 1500 cm^{-1}.
N-H	Out-of-plane bending absorption can sometimes be observed near 800 cm^{-1}.
C-N	Stretch occurs in the range 1350-1000 cm^{-1}.

Hydrogenation of fatty alcohols over M1 and M2 catalysts shows that primary amines are formed as evidenced from the FTIR absorption bands (Table 5.3).

Table 5.3: FTIR absorption band assignment of samples M1and M2 used in hydrogenation of fatty alcohol to fatty amines.

Wavenumber [cm^{-1}]	Observation and Peak Assignment	
	M1	M2
3315,3317	Stretching of N-H The free O-H The hydrogen bonded O-H band;	Stretching of N-H The free O-H The hydrogen bonded O-H band;
1627,1638	N-H bending	N-H bending
1448,1374	CH_3 bending	CH_3 bending
1110,1121	Stretching of C-N	Stretching of C-N
718,723	CH_2, the bending(rocking) motion associated with four or more CH_2 groups in an open chain	CH_2, the bending(rocking) motion associated with four or more CH_2 groups in an open chain

Figure 5.6 and 5.7 show a broad peak at a region 3500-3000 cm^{-1} indicating the presence of water in the solution with vibration of O-H overlapping the N-H region. This is correlates with NMR spectrum which also shows chemical shift of water. The N-H absorption usually has one or two sharp absorption bands of lower intensity in 3500-3000 cm^{-1}, whereas hydrogen-bonded O-H (3400-3300 cm^{-1}). Thus O-H bands, when it is in the N-H region it overlaps and will usually give a broad peak. Also primary amines give two absorption bands in this region, whereas alcohols as pure liquids give only one. The C-N stretching absorption occurs in the region from 1250 to 1000 cm^{-1} as a medium to strong band in the aliphatic amines (Figures 5.5 and 5.6).

Primary amines are also present as the N-H bending mode (scissoring) appears as a medium to strong intensity (broad) band in the range from 1640 to 1560 cm^{-1}. Methyl groups, CH_3 in the fatty amines have a characteristic bending absorption of 1448 cm^{-1} and 1374 cm^{-1} and the bending (rocking) motion associated with four or more CH_2 groups in an open chain appears near 718 cm^{-1} and 723 cm^{-1}.

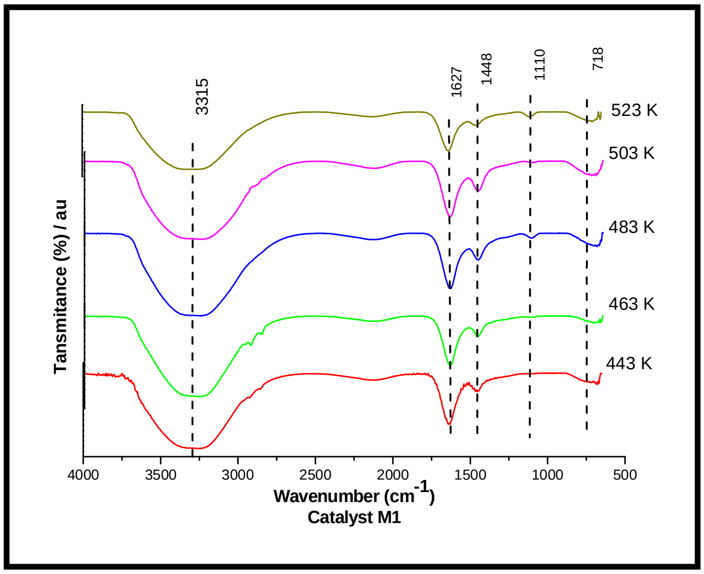

Figure 5.6: FTIR spectrum of hydrogenation of fatty alcohol using catalyst M1

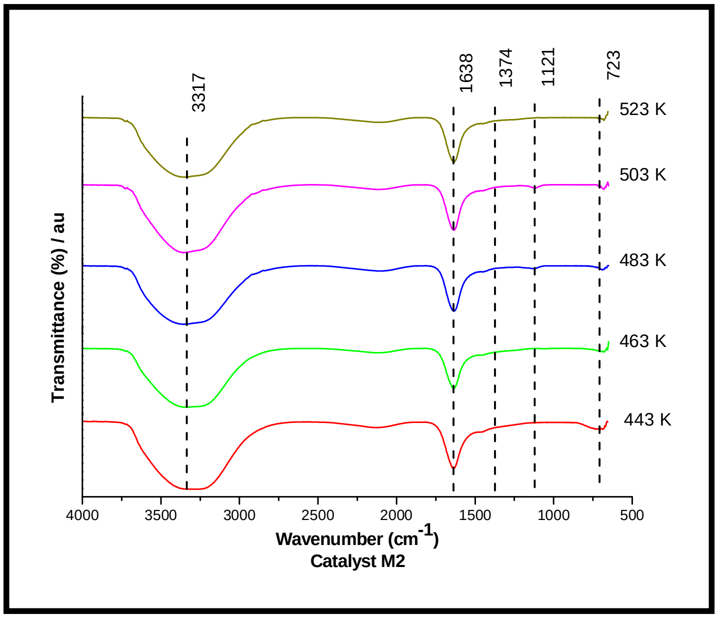

Figure 5.7: FTIR spectrum of hydrogenation of fatty alcohol using catalyst M2

5.5 Results and Discussion

The higher activity for a catalyst can be achieved by making use of supported binary system catalysts. Currently catalyst development exclusive for methanol synthesis, which may also be applicable for hydrogenation catalysts included adding a second metal component, ie. ZnO as a means of stabilizers – one of its function is to separate the copper crystallites physically, and hinder sintering process. Temperature, pressure, stirring speed and reaction time influence greatly the catalytic performance. The instant invention relates to a process for producing fatty amines which comprises reacting dodecanol with ammonia in the liquid phase at variables temperature and under pressure in the presence of a bimetal catalysts. Therefore, the experimental conditions used in the present study were selected as below.

Table 5.4: Experimental conditions applied for the hydrogenation of Fatty Alcohol

Operating conditions	Parameters
Temperature (K)	443-523
Pressure (bar)	30
Stirring speed (rpm)	500
Reaction time (hours)	4

Table 5.5: Factors Influencing Reaction Rate

Condition	Surface Hydrogen Concentration	Reaction Rate
Hydrogen dispersion (agitation) increase	+	+
Hydrogen pressure increase	+	+
Temperature increase (mass transport)	-	+
Catalyst active surface Increase	-	+

The hydrogenation of fatty alcohol to fatty amine is considered selective reactions. The selectivity to N-H is defined as follows:

$$S = \frac{Total\ N\text{-}H\ \ Produced}{Total\ Sum\ of\ \mathrm{Pr}oducts} * 100\%$$

The effect of temperature on the hydrogenation rate and fatty amine selectivity is shown in Figure 5.8 As is often the case, the reaction rate increases with temperature. This is because hydrogen is more soluble in oil at a higher temperature, and viscosity of oil reduces with temperature increase. Lower viscosity would lead to good mixing in the submerged phase and easy draining of entrained oil in the gas phase. These all facilitate the hydrogen transfer to the catalytic particles. Le Chatelier's principle states that if a dynamic equilibrium of a system is disturbed by a change in temperature, pressure or concentration, the position of equilibrium moves to minimize or counteract the effect of the disturbance. It seems beyond dispute that the increased rate on metal surface e.g. nickel – high active hydrogenation metal, which like other chemical reactions, occurs with rise in temperature. This variable far outweighs other variables such as solubility and transport of hydrogen in oil. Hence formation of hydrocarbon or overhydrogenation mentioned will easily occurs at higher temperature. Above 250^{0}C, water as well ammonia can poisons copper and nickel catalyst (Barrault et.al, 1993).

Bimetallic Cu-Zn(M1) and Cu-Ni(M2) catalysts on silica supports prepared by citrate routes were tested in liquid phase hydrogenation of fatty alcohol in the temperature range of 443 K to 523 K. The effect of reaction temperature in the hydrogenation of fatty alcohol to fatty amines is presented in Tables 5.6 and 5.7 and Figures 5.8 and 5.9. Both catalysts gave a good selectivity of N-H band at temperature 503 K with selectivity of 33.8% and 39.8% respectively (Figure 5.8 and Table 5.6). A similar profile is presented by intensity peak of N-H in NMR spectrum (Figure 5.9 and Table 5.7) for M1 and M2 catalysts which gave higher intensity at 503 K, of about 39.0% and 42.2% respectively. However, increasing the temperature at 523 K gives lower selectivity and intensity for both catalysts. This is shown in Table 5.6, as the selectivity of N-H band at 523 K for both catalysts decrease slightly. It can be concluded that operating the reaction at a moderate temperature would result in the generation of the primary product and the suppression of all pyrolysis products. Furthermore operating at a higher temperature may lead to lower selectivity due to transport limitations inside the porous catalysts (i.e. intra particle limitation). These findings indicate catalyst M2 gives better performance than catalyst M1 in hydrogenation of fatty alcohol to fatty amines. This conclusion relevant agree well with the characterization results (see chapter 4) which show M2 has better active sites. The presence of Ni in M2 seems to have more influence on the both chemical and physical properties of the catalyst creating better active sites of larger surface area compared to Zn (refer to Chapter 4). The reason for this could be due to the lower reducibility of Ni(II) compared to Zn(II). Lower reducibility of Ni(II) led to higher catalyst selectivity. A clear correlation is observed as higher the residual BET surface area obtained, the better is the catalytic performance. The data show that a successful supported catalyst is one that contains an optimal number of small particles dispersed on a large specific surface area.

From BET and SEM it is further known that the Cu does not form a film of clusters but aggregates (refer Chapter 4..2.3 and 4.2.4). Textural effects are relevant for catalysis in the context of the BET and SEM data analysis. This can be probed by looking at the correlations of the performance with textural modifications and/ with the residual BET surface area. As these data were only measured at the stage of calcination and before reductive activation, care must be taken in not over-interpreting the data. The data in Table 4.8 are, however of a clear signature. The greater the loss in initial surface area of the support (the greater the textural modification) the poorer is the catalytic performance. This seems to be a clear correlation in accordance to the statement that the higher the residual BET surface area found, the better is the catalytic performance. The data show that a successful supported catalyst is one that contains an optimal number of small metal particles dispersed on a large specific surface area. The initial design model of an impregnated Cu cluster catalyst is fully supported by the findings. Consequently, it seems important to go back to the preparation stages and re-examine all unit operations to adapt the synthesis protocol to the desired design model. This would be far more important than trying to optimise the performance by modifying the chemical composition of the systems studied so far.

Table 5.6: Selectivity of N-H band from hydrogenation of fatty alcohol in variable temperatures (443-523 K) by FTIR.

Catalyst	**Selectivity Of N-H band (%)**				
	443 K	**463 K**	**483 K**	**503 K**	**523 K**
M1	29.5	30.1	27.9	33.8	32.3
M2	33.2	34.5	35.3	39.8	36.9

Table 5.7: Intensity of N-H peak from hydrogenation of fatty alcohol in variable temperatures (443-523 K) by ^{1}H NMR.

Catalyst	**Intensity Of N-H peak (%)**				
	443 K	**463 K**	**483 K**	**503 K**	**523 K**
M1	38.3	38.7	38.4	39.0	37.3
M2	40.0	38.7	40.8	42.2	38.5

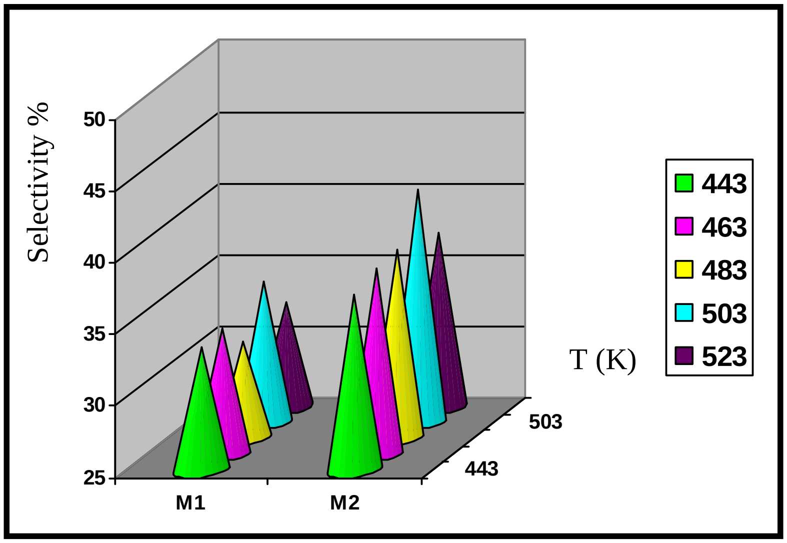

Figure 5.8: Selectivity of N-H band from hydrogenation of fatty alcohol by FTIR

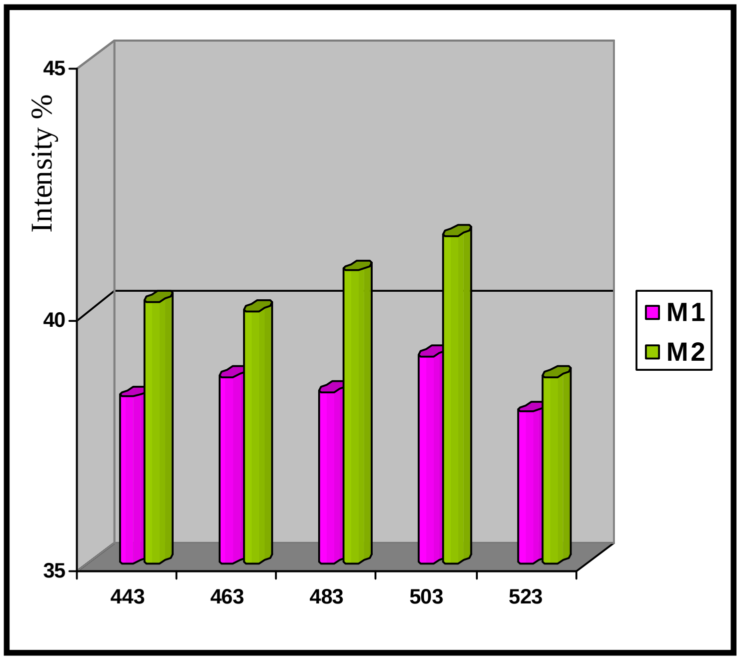

Figure 5.9: Intensity of N-H peak from hydrogenation of fatty alcohol by ^{1}H NMR.

CHAPTER 6

CONCLUSION AND RECOMMENDATION

6.1 Overall conclusion

This study focused mainly to investigate the effect of a second metal (zinc and nickel) in synthesis of silica supported copper based catalysts in order to achieve nanosize active metal particles that are highly dispersed on the support material and thus intrinsically give high activity and able to operate at relatively low pressures and moderate temperature particularly for hydrogenation of fatty alcohols to fatty amines. Comparison on the chemical and structural behaviors of the catalysts are studied by using data obtained from the FTIR, XRF, XRD, BET, SEM-EDX, and UV-Vis. Their thermal behavior was also studied by TGA, DSC and TPR results.

The elemental weight percent of M1 and M2 have been analyzed by XRF and EDX. The results from both analyses are useful and complementary to each other, in particular for investigation of the sample's homogeneity from surface to bulk. Generally for weight percent of Cu in both samples, there were systematic deviations between both analyses at approximately 2.8 % with XRF giving higher values of percentage than EDX. In the case of Zn, the deviation of weight percent is higher in EDX while for Ni it is higher in XRF. Therefore, upon considering some errors in both analyses, one can conclude that generally all metals are homogeneously scattered within the samples as good agreement between both analytical techniques are observed with more systematic deviation in case of M2 compared to M1.

From the BET results, M1 and M2 have retained type IV hysteresis, which is characteristic for mesoporous materials and also show a typical isotherm for materials with ordered mesoporous channels. Nevertheless, the hysteresis of M2 is shifted to higher relative pressure compared to the M1, indicating that larger pores are obtained. Also the pore volume is higher than the pore volume of M1. The hysteresis loop appears at high relative pressures and at this point, the isotherms show a large increase in the amount of adsorbed nitrogen. On the other hand, these materials have smaller specific surface areas than silica. M2, in comparison to M1, has a broader pore size distribution, a higher specific surface area and total pore volume and smaller pore dimensions.

The calcination temperature and the CuO content seem to play a role by influencing, on one hand the degree of dispersion and, on the other hand, the phenomena of sintering and surface area loss. High temperature during calcination which has provided sufficient energy and weakens the anchoring of copper solution precursor onto the support causes the particles to sinter and form large particles. TPR analysis indicated the reducibility of CuO was also increased with the crystalline size of CuO as shown in XRD analysis. The XRD results showed amorphous nature produced in both samples, meaning that the materials are nanoscopic basic structural units and the active working components in the material might also occur as nanostructured copper particles. The second metal (Zn and Ni) shows no sign of an individual phase formation and is assumed to be dissolved in the nanostuctured primary particles of the support silica thus helps to disperse the copper material throughout the support and prevents the sintering phenomenon of the active component. The occurrence of small and broad diffraction peak of CuO in XRD indicates the presence of many CuO nano-agglomeration dispersed on the coarse support of silica.

The SEM morphology results of M1 and M2 show that after calcinations the size of particle becomes smaller. The morphology clearly shows the formation of spherically ball shaped particles with uneven surface that contains several types of dents caused by the drying process. The highly dispersed copper on modified support is also observed. The chemical nature of the agglomeration has also changed (no more Si-OH groups as all are used up) by binding with the active phase and or were lost (structural promotion concept). The stronger the deviation of texture and morphologies are with respect to the silica supports, the less attractive is the catalytic function. Both samples exhibited very small particles of aggregates between silica and active phases at their surfaces. Most of these aggregates are no crystals as no signs of such particles were detected in the XRD. This morphology has supported well the conclusions in obtained the other characterizations.

The similarity of the FTIR spectra of both precursors suggests that same functional groups are present in both the dried samples which are in line with the UV-Vis spectroscopy characterization. Results from the thermal analyses supported by FT-IR show that calcination at 573 K was sufficient to remove all respective ligands. The sharp and broad exothermic peaks observed in DSC leading to the instantaneous and vigorous nature of the decomposition of the citrate precursor to form metal oxide have completed after this temperature.

6.2 Catalytic Performance

The catalyst screening process focused on verifying the effect of catalyst composition, i.e., silica supported Cu-Zn and Cu-Ni catalysts as well as reaction temperatures towards its activity, selectivity and stability. This methodology has greatly contributed in identifying the most active catalyst under at a prescribed reaction conditions (T= 443 -523 K; P= 30 bars; reaction time = 4 hours). From the catalyst screening of M1 and M2-based catalysts, Cu-Ni (M2) has been identified as the more active catalyst. Analysis on cumulative reaction mixtures collected after 4 hours using FTIR and NMR show predominantly the presence of primary amines. It is possible to differentiate and reconcile the amine structure (primary, secondary or tertiary) based on these two analytical techniques. The IR vibrations around 3000-3500 cm^{-1} wavenumbers are broad and overlapped with –OH of water. Other possible reaction products using NH_3, such as nitriles, amides were not detected. In addition, the catalysts used did not support etherification nor dehydration.

For the hydrogenation of fatty alcohol to fatty amines, testing time has been reduced in great length by using high throughput parallel reactor. The reaction results show that Cu-Ni (M1) exhibited high selectivity. This due to the catalyst containing small particles of highly dispersed metal on silica and that Ni^{2+} has lower reducibility compared to Cu.

6.3 Recommendations

The catalyst screening process focused on verifying the effect of catalyst composition, i.e., silica supported Cu-Zn and Cu-Ni catalysts as well as reaction temperatures towards its activity, selectivity and stability. This methodology has greatly contributed in identifying the most active catalyst under at a prescribed reaction conditions (T= 443 -523 K; P= 30 bars; reaction time = 4 hours). From the catalyst screening of M1 and M2-based catalysts, Cu-Ni (M2) has been identified as the more active catalyst. Analysis on cumulative reaction mixtures collected after 4 hours using FTIR and NMR show predominantly the presence of primary amines. It is possible to differentiate and reconcile the amine structure (primary, secondary or tertiary) based on these two analytical techniques. The IR vibrations around 3000-3500 cm^{-1} wavenumbers are broad and overlapped with –OH of water. Other possible reaction products using NH_3, such as nitriles, amides were not detected. In addition, the catalysts used did not support etherification nor dehydration.

This work has defined the role of 2nd metal and found that each metal (Zn or Ni) has significantly influenced the characteristic of the catalysts as shown clearly in the various characterization results. Therefore, the next phase of the research can be done by combining the optimized improved parameters such as 573 K calcination temperature with other modifications on the solidification method or presumably optimizing the metal loading to the support to maximize the content of catalytic active components of the catalyst.

On this basis, positive rules for designing new catalysts would be:

- Maintain the texture of the support as closely as possible and identify the integrity of the support by BET analysis revealing a minimum loss in surface area.
- Avoid the formation of XRD-detectable oxide particles.
- Abstain from hydrolyzing post synthesis treatments (ageing, washing) when citrates are used.
- Check for the availability of the Cu in TPR analysis before a catalytic test.
- The more sophisticated tools like spectroscopy and TEM or even surface analysis could be useful to be applied to promising catalysts with proven dispersion of the active Cu to better elucidate the complex nature of the nanostructured Cu.
- Determination of the end temperature with TG or DSC to minimize the calcination temperature and utilize the method of reduction of the calcination end temperature by introducing dwell times placed at the lower temperatures of individual thermal events.
- Testing the catalysts in order see the performance in target reaction and relate the characteristics of samples with the performance.
- Analysed the product using Gas Chromatography (GC) or High Performance Liquid Chromatography (HPLC)

A combination of BET analysis and of TPR for each sample would be a suitable high-throughput characterization to check for the usefulness of a catalyst prior to a catalytic test. In this way it would be possible to share the burden of classifying large number of samples by kinetic testing and a priori characterization with just simple means. The more sophisticated tools like SEM/TEM or even surface analysis such as XPS could then be applied to a few promising candidates with proven dispersion of the active Cu to better elucidate the complete nature of the nanostructured Cu.

Within the limited significance of the small data set of the samples it is possible to deduce a few hints on structure-activity correlations. This technique must be applied with great care as the structure was not detected directly and no check was possible if the texture of the catalyst was preserved during catalytic observation. Without any in-situ back up the following correlation have only diagnostic value.

In summary, it was well possible to shed light on the origin of the different behaviors of the catalyst materials. The different performances could be traced back to structural characteristics and rules were derived as how to avoid structural shortcomings of the initial set of systems. Cyclic application of these rules followed by characterization and refinement of the rules will quickly lead to better catalysts. Such a rational approach is scaleable, as the choices of parameters are rational and the boundary conditions in the parameter space of synthesis and activation are known. The present work has thus a generic character for other projects in the group and gives a clear example of the superior strategy of a combination of high throughput experimentation combined with in-depth characterization over purely combinatorial variations of the composition of catalyst formulations.